University of Texas Rio Grande Valley

ScholarWorks @ UTRGV

Theses and Dissertations

8-2021

Investigation of the Effect of Process Parameters by Taguchi Method on Structural and Electrical Properties of RF Magnetron Sputtered SiO2 & pSi on Si Substrate

Sajid Mahfuz Uchayash
The University of Texas Rio Grande Valley

Follow this and additional works at: https://scholarworks.utrgv.edu/etd

Part of the Electrical and Computer Engineering Commons

Recommended Citation

Uchayash, Sajid Mahfuz, "Investigation of the Effect of Process Parameters by Taguchi Method on Structural and Electrical Properties of RF Magnetron Sputtered SiO2 & pSi on Si Substrate" (2021). *Theses and Dissertations*. 986.
https://scholarworks.utrgv.edu/etd/986

This Thesis is brought to you for free and open access by ScholarWorks @ UTRGV. It has been accepted for inclusion in Theses and Dissertations by an authorized administrator of ScholarWorks @ UTRGV. For more information, please contact justin.white@utrgv.edu, william.flores01@utrgv.edu.

INVESTIGATION OF THE EFFECT OF PROCESS PARAMETERS BY TAGUCHI METHOD ON STRUCTURAL AND ELECTRICAL PROPERTIES OF RF MAGNETRON SPUTTERED SiO_2 & pSi ON Si SUBSTRATE

A Thesis

by

SAJID MAHFUZ UCHAYASH

Submitted to the Graduate College of
The University of Texas Rio Grande Valley
In partial fulfillment of the requirements for the degree of

MASTER OF SCIENCE IN ENGINEERING

August 2021

Major Subject: Electrical Engineering

INVESTIGATION OF THE EFFECT OF PROCESS PARAMETERS BY TAGUCHI METHOD

ON STRUCTURAL AND ELECTRICAL PROPERTIES OF RF MAGNETRON

SPUTTERED SiO_2 & pSi ON Si SUBSTRATE

A Thesis
by
SAJID MAHFUZ UCHYASAH

COMMITTEE MEMBERS

Dr. Hasina Huq
Chair of Committee

Dr. Paul Choi
Committee Member

Dr. Md. Jasim Uddin
Committee Member

August 2021

Copyright 2021 Sajid Mahfuz Uchayash
All Rights Reserved

ABSTRACT

Uchayash, Sajid Mahfuz, Investigation of The Effect of Process Parameters by Taguchi Method on Structural and Electrical Properties of RF Magnetron Sputtered SiO_2 & pSi on Si Substrate. Master of Science in Engineering (MSE), August, 2021, 96 pp., 57 Figures, 25 Tables, 61 References

In this work, Taguchi Signal-to-noise (S/N) analysis was applied to investigate the effect of varying three process parameters, namely- sputtering power, working pressure and Ar gas flow rate on the surface, morphological and electrical properties of the RF sputtered SiO_2 and Boron doped pSi over Si substrate. The contribution of a particular process parameter on these properties was also inspected by applying Analysis of Variance (ANOVA). SiO_2 and pSi thin films were fabricated over Si substrate using RF magnetron sputtering system. Three sets of inputs for the three mentioned process parameters were chosen for sputtering SiO_2 and pSi thin films. To deposit SiO_2, 150W, 200W and 250W power levels were chosen, for pSi deposition-power levels were 100W, 150W and 200W; 5mTorr, 10mTorr and 15mTorr were chosen for pressure and three Ar gas flow rate levels at 5, 10 and 15 sccm were selected. By performing Taguchi L^9 orthogonal array, nine combinations of sputtering parameters were prepared for depositing SiO_2/Si and pSi/Si thin films. The surface morphological and electrical properties (resistivity per unit area and capacitance per unit area) of the sputtered samples were therefore

inspected by analyzing the Taguchi design of experiment. Signal-to-noise (S/R) analysis presents how the properties were affected by the variation of each process parameter. ANOVA analysis showed that sputtering power and working pressure are the two dominant process parameters contributing more to surface morphological and electrical properties. A regression model for surface roughness of the SiO_2/Si and pSi/Si thin film samples was also derived. The electrical properties of the SiO_2/Si and pSi/Si thin films, however, didn't show linearity and that is why it was not possible to derive a regression model for the electrical properties of SiO_2/Si and pSi/Si sputtered thin films.

DEDICATION

To the soul now living afar,

Out of sight and maybe gone forever.

But never she will disappear,

As in my heart, I will hold her dear.

May this milestone of mine

bring smile and shine

The face of her-I am dying to see again.

-To my mother, Kazi Habiba.

Without her sacrifice, I wouldn’t be what I am now.

Thank you, mother!

ACKNOWLEDGMENT

With the blessing of almighty God, I have finished writing my thesis for M.Sc. degree in Electrical Enginnering. Thanks to all the people who have helped directly or indirecty in my pursuation of the M.Sc. degree. The first mention should be Dr. Hasina Huq, my supervisor, who had supported me for the past two years with her guidance and directions. Her trust on me had embued me with confidance and propeled me to the endevor I have undertaken to complete my thesis. She was quick to take any decisions that will help the reseaerch work I inteded to accomplish. Her patience to withstand my idiosyncratic working routine and technique is certainly a freedom for me which have I have availed to the full, not gonna lie! I am delighted that I got the opportunity to work in the Sputtering System Lab under her supervision. I am very thankful to some of my colleagues. Prossanto Biswas- who trained me to work on the sputtering system. Muhtasim Ul Karim Sadaf has taught me how to use XRD machine. Al Mazedur Rahman has helped me a lot with the statistical anlysis. Special mention to Meah Imtiaz Zulkarnain, whose tremenmdous assist, effort, constructive advice and counsel helped me to improve the quality and delivery of this research work. Dr. Ahmed Touhami and Dr. Victoria Pallida had provided the SEM and AFM images had lessened my work load. As the completion of this thesis book is in progress, thanks to all these people who made it possible. I am immense grateful and in debt to you. And thanks to the almighty again for everything he has betowed on me.

TABLE OF CONTENTS

Page

ABSTRACT ... iii

DEDICATION ... v

ACKNOWLEDGMENT ... vi

TABLE OF CONTENTS ... vii

LIST OF TABLES ... x

LIST OF FIGURES ... xii

CHAPTER I. INTRODUCTION ... 1

1.1 Brief Description RF Sputtering ... 4

1.2 SiO_2 Thin Film Literature Review ... 6

1.3 pSi Thin Film Literature Review ... 7

1.4 Objective of the Thesis ... 8

CHAPTER II. EXPERIMENTAL SETUP AND METHODOLOGY ... 10

2.1 Fabrication ... 10

2.1.1 Substrate Cleaning ... 10

2.1.2 Thin Film Coating by RF Magnetron Sputtering ... 12

2.2 Characterization ... 14

2.3 Analysis ... 15

2.3.1 Taguchi DOE and S/N ratio 15

2.3.2 Analysis of Variance (ANOVA) 19

2.3.3 Regression Analysis 21

CHAPTER III. CHARACTERIZTION OF SiO_2/Si THIN FILMS 23

3.1 Surface Roughness of SiO_2/Si Thin Films 23

3.2 XRD Analysis of SiO_2/Si Thin Films 26

3.3 Surface Morphology & Surface Topography of SiO_2/Si Thin Films 28

3.4 Electrical Properties of SiO_2/Si Thin Films 31

3.5 Adhesion 48

3.6 Conclusion 48

CHAPTER IV. CHARACTERIZTION OF pSi/Si THIN FILMS 49

4.1 Surface Roughness of pSi/Si Thin Films 49

4.2 XRD Analysis of pSi/Si Thin Films 52

4.2.1 Crystallinity 55

4.2.2 Grain Size 57

4.2.3 Micro-strain 59

4.2.4 Dislocation Density 60

4.3 Electrical Properties of pSi/Si Thin Films 61

4.4 Adhesion 75

4.5 Conclusion 76

CHAPTER V. FUTURE WORKS 77

5.1 Fabrication of Enhancement Mode n-MOSFET by Physical Vapor Deposition 77

REFERENCES 81

APPENDIX A 90

APPENDIX B 93

BIOGRAPHICAL SKETCH 96

LIST OF TABLES

Page

Table 2.1: Summary of sputtering process for the thin films 13

Table 2.2: Sputtering parameters for SiO_2/Si thin films 16

Table 2.3: Sputtering parameters for pSi/Si thin films 17

Table 2.4: 9 sets of parameter combinations from Taguchi L^9 orthogonal array for sputtering SiO_2/Si thin films 17

Table 2.5: 9 sets of parameter combinations from Taguchi L^9 orthogonal array for sputtering pSi/Si thin films 19

Table 3.1: Summary of surface roughness (R_a) of SiO_2/Si thin films 24

Table 3.2: Summary of ANOVA result for surface roughness (R_a) of SiO_2/Si thin films. 25

Table 3.3: Summary of the regression analysis of surface roughness of SiO_2/Si thin films 26

Table 3.4: Summary of surface and crystallographic information of SiO_2/Si thin films.............. 28

Table 3.5: Summary of electrical properties of SiO_2/Si thin film samples.................................. 33

Table 3.6: Summary of ANOVA result for resistance/area ($R_{nASiO_2/Si}$) at 50 kHz frequency for SiO_2/Si thin films... 45

Table 3.7: Summary of ANOVA result for resistance/area ($C_{nASiO_2/Si}$) at 50 kHz frequency for SiO_2/Si thin films... 45

Table 3.8: Summary of ANOVA result for resistance/area ($R_{nASiO_2/Si}$) at 10 kHz frequency for SiO_2/Si thin films... 46

Table 3.9: Summary of ANOVA result for resistance/area ($R_{nASiO_2/Si}$) at 10 kHz
frequency for SiO_2/Si thin films 46
Table 4.1: Summary of surface roughness (R_a) of pSi/Si thin films 50
Table 4.2: Summary of ANOVA result for surface roughness (R_a) of pSi/Si thin films 51
Table 4.3: Summary of the regression analysis of surface roughness of pSi/Si thin films 52
Table 4.4: Summary of the XRD analysis of pSi/Si thin films 54
Table 4.5: Summary of ANOVA result for crystallography (XRD peaks) of pSi/Si thin films... 56
Table 4.6: Summary of electrical properties of pSi/Si thin film samples. 70
Table 4.7: Summary of ANOVA result for resistance/area ($R_{nApSi/Si}$) at 25 kHz
frequency for pSi/Si thin films 73
Table 4.8: Summary of ANOVA result for resistance/area ($R_{nApSi/Si}$) at 50 kHz
frequency for pSi/Si thin films 73
Table 4.9: Summary of ANOVA result for capacitance/area ($C_{nApSi/Si}$) at 25 kHz
frequency for pSi/Si thin films 74
Table 4.10: Summary of ANOVA result for capacitance/area ($C_{nApSi/Si}$) at 50 kHz
frequency for pSi/Si thin films 74
Table 5.1: Process parameters used to deposit different layers of enchance mode n-MOSFET .. 79

LIST OF FIGURES

Page

Figure 1.1: A conventional thin film deposited on a substrate. 1

Figure 1.2: Global thin film market projection from 2018-2028... 2

Figure 1.3: Classification of thin film deposition techniques. 3

Figure 2.1: Cleaning steps of the Si substrate.. 11

Figure 2.2: Flowchart of the fabrication steps. 12

Figure 2.3: Flowchart of characterization of the fabricated thin films 14

Figure 2.4: SiO_2 and pSi target used for sputtering 15

Figure 2.5: 9 RF sputtered SiO_2/Si thin film samples.. 18

Figure 2.6: 9 RF sputtered SiO_2/Si thin film samples.. 18

Figure 2.7: Flowchart of performing statistical analysis 21

Figure 3.1: S/N response graph for surface roughness of SiO_2/Si thin films 25

Figure 3.2: XRD pattern of SiO2/Si thin film samples presented in stacked lines by Y offset.... 27

Figure 3.3: Surface and cross-sectional SEM micrograph of the SiO_2/Si thin film samples........ 29

Figure 3.4: AFM images of the SiO_2/Si thin film samples 30

Figure 3.5: Connection diagram SiO_2/Si thin film samples for impedance spectroscopy measurement.. 31

Figure 3.6: Bode plots and Real Z' vs Img Z'' scatter plot for SiO_2/Si thin film sample 1-3...... 34

Figure 3.7: Bode plots and Real Z' vs Img Z'' scatter plot for SiO_2/Si thin film sample 4-6...... 35

Figure 3.8: Bode plots and Real Z' vs Img Z'' scatter plot for SiO_2/Si thin film sample 7-9...... 36

Figure 3.9: Resistance/area ($R_{nASiO_2/Si}$) and capacitance/area ($C_{nASiO_2/Si}$) vs. frequency plots for SiO_2/Si Sample 1 37

Figure 3.10: Resistance/area ($R_{nASiO_2/Si}$) and capacitance/area ($C_{nASiO_2/Si}$) vs. frequency plots for SiO_2/Si Sample 2 37

Figure 3.11: Resistance/area ($R_{nASiO_2/Si}$) and capacitance/area ($C_{nASiO_2/Si}$) vs. frequency plots for SiO_2/Si Sample 3 38

Figure 3.12: Resistance/area ($R_{nASiO_2/Si}$) and capacitance/area ($C_{nASiO_2/Si}$) vs. frequency plots for SiO_2/Si Sample 4 38

Figure 3.13: Resistance/area ($R_{nASiO_2/Si}$) and capacitance/area ($C_{nASiO_2/Si}$) vs. frequency plots for SiO_2/Si Sample 5 39

Figure 3.14: Resistance/area ($R_{nASiO_2/Si}$) and capacitance/area ($C_{nASiO_2/Si}$) vs. frequency plots for SiO_2/Si Sample 6 39

Figure 3.15: Resistance/area ($R_{nASiO_2/Si}$) and capacitance/area ($C_{nASiO_2/Si}$) vs. frequency plots for SiO_2/Si Sample 7 40

Figure 3.16: Resistance/area ($R_{nASiO_2/Si}$) and capacitance/area ($C_{nASiO_2/Si}$) vs. frequency plots for SiO_2/Si Sample 8 40

Figure 3.17: Resistance/area ($R_{nASiO_2/Si}$) and capacitance/area ($C_{nASiO_2/Si}$) vs. frequency plots for SiO_2/Si Sample 9 41

Figure 3.18: S/N graph for the resistance/area ($R_{nASiO_2/Si}$) of SiO_2/Si thin films at 50kHz........ 43

Figure 3.19: S/N graph for the capacitance/area ($C_{nASiO_2/Si}$) of SiO_2/Si thin films at 50kHz..... 43

Figure 3.20: S/N graph for the resistance/area ($R_{nASiO_2/Si}$) of SiO_2/Si thin films at 10kHz........ 44

Figure 3.21: S/N graph for the capacitance/area ($C_{nASiO_2/Si}$) of SiO_2/Si thin films at 10kHz..... 44

Figure 4.1: S/N response graph for surface roughness of pSi/Si thin film. 51

Figure 4.2: XRD pattern of the Si [1 0 0] substrate. 53

Figure 4.3: XRD pattern of 9 pSi/Si thin film samples... 53

Figure 4.4: S/N response graph for Crystallinity of the pSi/Si thin films.................................. 55

Figure 4.5: Grain size of the pSi/Si thin films. 58

Figure 4.6: Mirco-strain of the pSi/Si thin films.. 59

Figure 4.7: Dislocation density of the pSi/Si thin films.. 60

Figure 4.8: Bode plots and Real Z' vs Img Z'' scatter plot for pSi/Si thin film sample 1-3 62

Figure 4.9: Bode plots and Real Z' vs Img Z'' scatter plot for pSi/Si thin film sample 4-6 63

Figure 4.10: Bode plots and Real Z' vs Img Z'' scatter plot for pSi/Si thin film sample 7-9 64

Figure 4.11: Resistance/area ($R_{nApSi/Si}$) and capacitance/area ($C_{nApSi/Si}$) vs. frequency plots for pSi/Si Sample 1 65

Figure 4.12: Resistance/area ($R_{nApSi/Si}$) and capacitance/area ($C_{nApSi/Si}$) vs. frequency plots for pSi/Si Sample 2 65

Figure 4.13: Resistance/area ($R_{nApSi/Si}$) and capacitance/area ($C_{nApSi/Si}$) vs. frequency plots for pSi/Si Sample 3 66

Figure 4.14: Resistance/area ($R_{nApSi/Si}$) and capacitance/area ($C_{nApSi/Si}$) vs. frequency plots for pSi/Si Sample 4 66

Figure 4.15: Resistance/area ($R_{nApSi/Si}$) and capacitance/area ($C_{nApSi/Si}$) vs. frequency plots for pSi/Si Sample 5 67

Figure 4.16: Resistance/area ($R_{nApSi/Si}$) and capacitance/area ($C_{nApSi/Si}$) vs. frequency plots for pSi/Si Sample 6 67

Figure 4.17: Resistance/area ($R_{nApSi/Si}$) and capacitance/area ($C_{nApSi/Si}$) vs. frequency plots for pSi/Si Sample 7 68

Figure 4.18: Resistance/area ($R_{nApSi/Si}$) and capacitance/area ($C_{nApSi/Si}$) vs. frequency plots for pSi/Si Sample 8 68

Figure 4.19: Resistance/area ($R_{nApSi/Si}$) and capacitance/area ($C_{nApSi/Si}$) vs. frequency plots for pSi/Si Sample 9 69

Figure 4.20: S/N graph for the resistance/area ($R_{nApSi/Si}$) of pSi/Si thin films at 25kHz 71

Figure 4.21: S/N graph for the resistance/area ($R_{nApSi/Si}$) of pSi/Si thin films at 50kHz 71

Figure 4.22: S/N graph for the capacitance/area ($C_{nApSi/Si}$) of pSi/Si thin films at 25kHz.... 72

Figure 4.23: S/N graph for the capacitance/area ($C_{nApSi/Si}$) of pSi/Si thin films at 50kHz.... 72

Figure 5.1: Methodology of MOSFET Fabrication by Physical Vapor Deposition 78

Figure 5.2: Steps of n-MOSFET Fabrication.... 79

Figure 5.3: I-V characteristics of enhancement mode nMOSFET fabricated by Physical Vapour Deposition (PVD) technique….80

CHAPTER I

INTRODUCTION

Silicon and its different types of variants have a significant contribution towards semiconductors, MEMS, NEMS and fabrication industry. Apart from intrinsic silicon, silicon doped with P-type and N-type dopants- which usage is broadly bound in semiconductor and photoelectric devices and SiO2 largely used as the insulation layer in those devices, other forms of silicon compounds like Si3N4 and SiC have been attracting interests in recent years as special layers in compound heterojunction devices. Intensive efforts have been taken over the last couple of decades to grow these materials over numerous substrates according to the application fields and improve the performance of the developed layers.

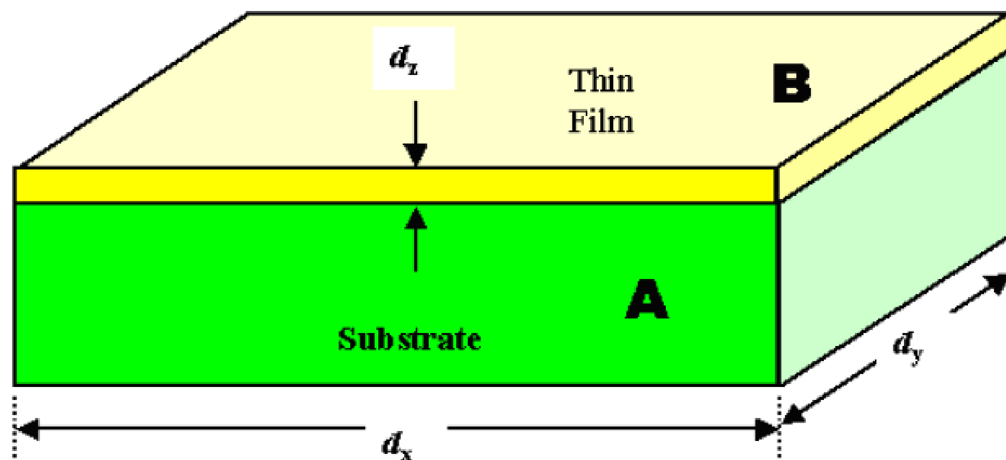

Figure 1.1: A conventional thin film deposited on a substrate. d_z denotes the thickness of the film while d_x and d_y denote the dimension of the substrate [1].

As the size of the semiconductor devices is shortening exponentially, the thin films industry, which is closely connected with the device industry is being forced to produce thinner and thinner films as a result. From the micrometer range a decades ago, requirements of superstrates which are no more than several nanometers have already appeared in the market. To quench this ever-growing demand of exponentially miniaturized thin-film layers, several growing techniques have been introduced to clinch the maximum performance, thanks to the elaborate research performed in this criterion.

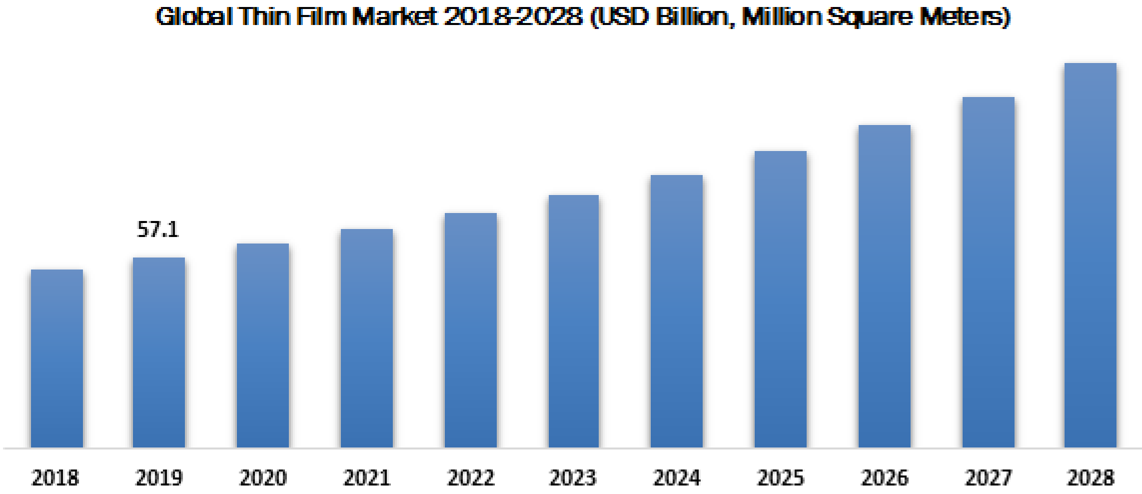

Figure 1.2: Global thin film market projection from 2018-2028 [4].

Current and emerging applications in various fields like MEMS, optoelectronic devices and semiconductor industry drives the market of thin solid films [2]. Expectation of increasing efficiency while reducing the size will propel the research, advancement and market growth in the upcoming years [3]. Encouragement in using green solar energy will also add a positive impact. Forecasts suggest the global revenue in the thin-film market is projected to reach about 202.6 billion by the year 2028 [4].

Although the miniaturization and efficiency dilemma is curving out better prospects for thin-film sectors, from researcher's perspective, it is also imposing conundrums. Controlling the nanometer level growth of the thin film is very challenging. The effect of lattice mismatch between substrate and superstrate is also very prominent at the nanoscale range and as a consequence, the residual stress in the thin-film becomes a crucial and influential and property. Conventionally, two types of residual stress are existent in thin films- compressive stress forcing thin films to expand and tensile stress, causing films to contract in the direction parallel to

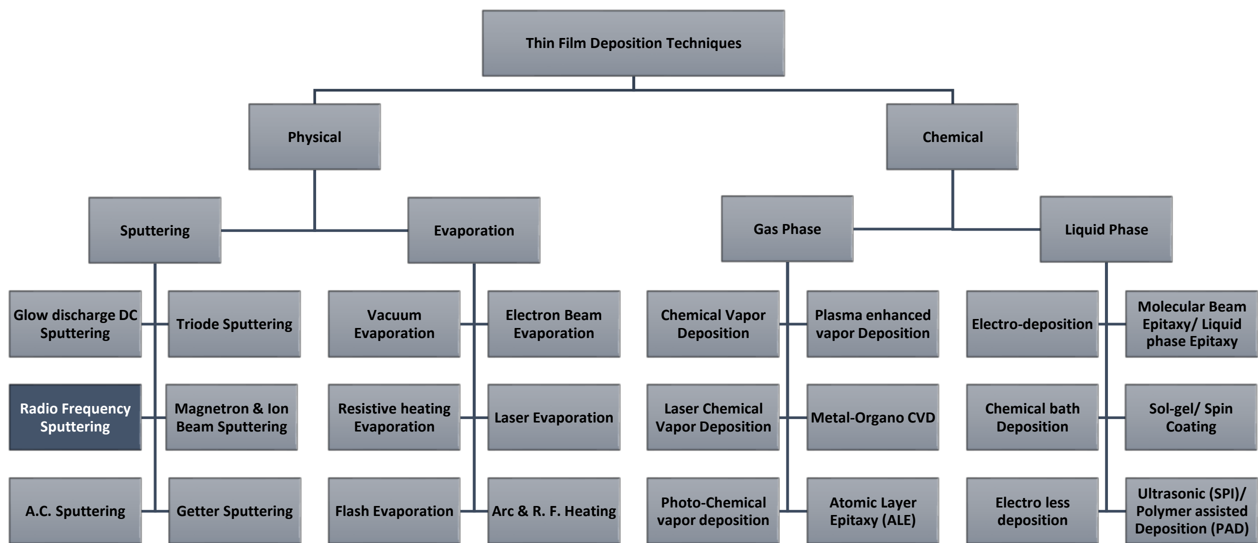

Figure 1.3: Classification of thin film deposition techniques [5].

substrate surface [6]. Excessive tensile stress may result in film cracking and over-compressive stress is the reason for delamination, peeling off or buckling [7, 8]. It has been found that the residual strain is inversely proportional to film thickness [9]. Thermal treatments is another source of residual stress, as the thermal expansion coefficient mismatch between substrate and superstrate [7-9]. This mechanical property, namely residual stress, can significantly impact

other properties important for specific applications like -adhesion, fracture toughness, thermo-mechanical behavior, conductivity, permittivity, reflectivity, etc. [7].

Since thin solid films subjected to high temperature may have some adverse effect on their mechanical property, commonly used high-temperature oxidation or thermally grown films may not be appropriate for every application. As mentioned before, many techniques have been introduced through the years to generate thin solid films. Each has merits over one another, taking the specificity of implementation of the film into account. Figure 1.3 shows a summary of fabrication techniques that are being practiced in industry and for research works.

Mainly, thin film deposition techniques can be categorized into two sections. Physical Vapor Deposition (PVD) and Chemical Vapor Deposition (CVD). In this research work, Radio Frequency (RF) Sputtering- one of the PVD technique is used to fabricate SiO_2 and pSi layer over Si substrate, so focus would be given only on this fabrication process. In the following section brief in introduction, history and technical advantages/disadvantages of RF sputtering is described.

1.1 Brief Description RF Sputtering

Magnetron sputtering is one of the Physical Vapor Deposition (PVD) techniques for fabricating thin solid films. Depending on the current provided, magnetron sputtering can be divided into two categories- Direct Current (DC) magnetron sputtering and Radio Frequency (RF) magnetron sputtering. DC magnetron sputtering is commonly used to deposit thin films from metals or conductive targets. RF sputtering can also be employed for metal thin film deposition. However, targets that are non-metal and low conductive are always sputtered using radio frequency signal, as DC signal has limitations when it comes to dielectric materials [10].

Radio Frequency signal is applied to the two electrodes in a vacuum environment in RF magnetron sputtering technique, thus altering the electric potential of the current, which helps to avoid charge rising up in dielectric materials [10]. High electric volts in vacuum create plasma and energized process gas hit the target; atoms of the target then drop on the substrate and create a thin superstrate [10, 11]. Detailed working principle of RF magnetron sputtering is explained in Chapter 2.

As the direction of polarity changes with time, RF magnetron sputtering has a lower deposition rate compared to DC sputtering, CVD process and thermal depositions [12]. Nevertheless, it has some advantages over the high-temperature oxidation process or chemical vapor deposition (CVD) technique [12, 13].

- Low cost of the process
- Less complexity
- Flexibility of sequential deposition
- Elimination of toxic gases
- Uniform deposition at larger areas
- High-purity films
- Protection of microelectronic circuits from higher temperature etc.

Because of the advantages RF sputtering offers, MEMS and micro-electronics industries most of the time prefer this process to coat non-metal and metal thin films. In this thesis, RF magnetron sputtering is applied to fabricate SiO_2 and pSi thin films on intrinsic Si substrate. The experimental setup is elaborately described in Chapter 3.

1.2 SiO_2 Thin Film Literature Review

Thin films of SiO_2 have a broad range of usage in microelectronics, MEMS and optoelectronic devices. For example- as diffusion masks and passivation coating, SiO_2 thin films are widely used in Si-based IC [14, 15]. In MEMS, apart from general use as structural or sacrificial layer [16-18], deposited SiO_2 thin films are the focus of interest to realize suspended microstructure like cantilever beams and micro-bridge [12]. In optoelectronic devices like solar cells, due to their adaptivity to harsh environments [19] and transparency [20], SiO_2 thins films, often in combination with other oxide thin films. are used as anti-reflection and absorption coating [19-23]. The use of SiO_2 films as gate insulation layer in CMOS technology is universal. Dynamic Random Access Memory (DRAM) and Resistance Switching Random Access Memory (ReRAM) use SiO_2 layer as capacitor dielectrics [24, 25]. In detector/sensor applications, or for solar energy devices SiO_2 layer works as intermetal insulator. Compound thin films of transition metal and metal oxides with SiO_2 increase the dielectric constant of the layer, which reduces leakage current and improves device properties [26].

SiO_2 thin film deposited by magnetron sputtering has been reported in several previous works [13, 27-30], many of which investigated the structural, electrical and insulation characteristics of the sputtered SiO_2 thin films as the function of the process parameters. The effect of RF power and working pressure on the deposition rate, O/Si ratio of the film, surface morphology and microstructure was explored in [12, 19]. Electrical properties like- breakdown field strength, resistivity and dielectric constant of the sputtered SiO_2 layer prepared by reactive pulse magnetron sputtering were reported in [24, 27]. Ho et al. studied the conductivity, reverse saturation-current and conversion efficiency of the GaAs solar cell coated with SiO_2 ARC (anti-

reflection coating) [24]. For high dielectric strength, layered Al_2O_3-SiO_2 thin film composites deposited by pulsed DC and RF magnetron sputtering were reported by Hanby et al. [28].

1.3 pSi Thin Film Literature Review

Comparing to SiO_2 thin film and Si thin film works on doped silicon thin film are lesser in number. Doped silicon is more used as substrates in most microelectronic and MEMS devices. Nevertheless, there are still many reports which characterized Si thin film doped with p-type material and explored its potential application. Silicon doped with p-type materials has extensive use in silicon-based solar cells and optoelectronic devices [31-35], for instance- as window layer p–i–n solar cells [31, 33] and an intermediate reflector in thin-film silicon tandem solar cells [35]. Other noteworthy applications of pSi thin films are- as anodes of lithium-ion batteries [36], thermoelectric generator (TEG) material [37] and piezo resistors [38].

Although silicon doped with p-type material is a better conductor than intrinsic Si and SiO_2, RF sputtering is also the general choice over DC sputtering to produce pSi thin films by physical vapor deposition (PVD) technique. Studies of DC and RF sputtered silicon and p-Si have been conducted for several decades. Boron and silicon were co-sputtered at low hydrogen flux and a relatively low temperature of 250° C to create thin films for detection of infrared radiation in [39]. For MEMS application, silicon thin film deposited by RF sputtering at low temperature ($<250^{o}$C) has been reported in [40]. In [41], electrical properties, namely- dark conductivity, carrier mobility and carrier concentration of RF sputtered boron and phosphorous doped microcrystalline silicon thin films deposited from heavily doped silicon targets, were investigated. Haberle et al. explored the dependence of other types of electrical properties like- sheet resistance and hall mobility on deposition, annealing and diffusion parameters of boron

doped polycrystalline Si on SiO_2 layer [42]. Tabata et al. studied the variation of structural and electrical properties of RF sputtered boron doped hydrogenated microcrystalline Si with respect to film thickness [43].

1.4 Objective of the Thesis

In this current work, a detailed study of the effect of process parameters on the morphological, structural and electrical properties of SiO_2 and boron doped silicon thin films deposited on pure Si substrate using RF magnetron sputtering is presented. The following investigation has been done and reported in this thesis-

- ✓ Implementation of Taguchi Design of Experiment (DOE) to choose nine sets of combinations of process parameters of RF magnetron sputtering to fabricate SiO_2/Si and pSi/Si thin films. Focused process parameters are- RF power, working pressure and Ar gas flow rate.
- ✓ Investigation of structural properties (crystallinity of SiO_2/Si and crystallinity, grain size, micro-strain and dislocation density of pSi/Si thin films) of the fabricated layers.
- ✓ Inspection of morphological properties (surface roughness, surface morphology and surface topology of SiO_2/Si thin films and only surface roughness of pSi/Si thin films).
- ✓ Evaluation of electrical properties (resistivity per unit area (R_{nA}) and capacitance per unit area (C_{nA})) of both types of thin films.
- ✓ Execution of Signal to noise ratio (S/N) analysis and Analysis of variance (ANOVA) to understand the effect of a particular process parameter and their individual contribution to a specific property of the sputtered SiO_2/Si and pSi/Si thin films.

Unlike traditional experiments, which may require a large number of samples to experiment with, the Taguchi method provides a systematic design approach with more efficiency using a lesser number of experimental results [20, 21]. Signal to noise ratio (S/N) analysis is applied to understand how the properties of SiO_2/Si and pSi/Si thin films vary with the change of three major process parameters- RF sputtering power, working pressure and Ar gas flow rate. Analysis of variance, followed by the S/N result, tells us how much each process parameter contributes to a particular property of the thin films. For measuring electrical properties of SiO_2/Si thin film and pSi/Si samples- resistivity per unit area (R_{nA}) and capacitance per unit area (C_{nA}), Impedance spectroscopy was used. Using impedance spectroscopy to understand the electrical properties of thin films has been reported in many previous studies [44-47]. Whereas Bartzsch et al. measured the DC/AC resistivity and dielectric constant [12, 17] of SiO_2 thin films; and Haberle et al. examined sheet resistance and hall mobility of boron doped silicon thin films [42], in current work the frequency was varied from 1Hz to 1MHz and observed the variation of R_{nA} and C_{nA} of the SiO_2/Si and pSi/Si thin films. A particular frequency where the R_{nA} and C_{nA} of the thin films show outliers and more trending data was chosen to perform S/N and ANOVA analysis for understanding the effect of parameter changes on resistivity and capacitance of the SiO_2/Si and pSi/Si thin films. From our data, a regression model for only surface roughness was possible to derive. Electrical properties- resistivity per unit area (R_{nA}) and capacitance per unit area (C_{nA}) did not show a linear outcome, and therefore, it was not possible to derive a regression model for these properties.

CHAPTER II

EXPERIMENTAL SETUP AND METHODOLOGY

The methodology of this research can be divided into three portions.

- Fabrication of the thin films
- Characterization of the thin film properties
- Statistical analysis of the acquired data

In this chapter, the experimental setup and methodology of the experiments are described in detail.

2.1 Fabrication

The first part of this research started with the fabrication of the thin films. Thin films fabrication steps can be split in two section:

- Substrate cleaning and
- Thin film coating by RF Magnetron Sputtering

2.1.1 Substrate Cleaning

Intrinsic Si substrate od diameter 4’’ and thickness of 525±10 µm was first diced into smaller pieces with shape and size according to needs. Then the diced substrates were washed

with deionized water. After that, they were submerged in Acetone (CH_3-CO-CH_3) and then gently shook for 10 minutes. Then, they were submerged in Ethanol (C_2H_5OH) and again, gently shook for 10 minutes. Finally, they were again washed in deionized water carefully and blow dried to get clean substrates.

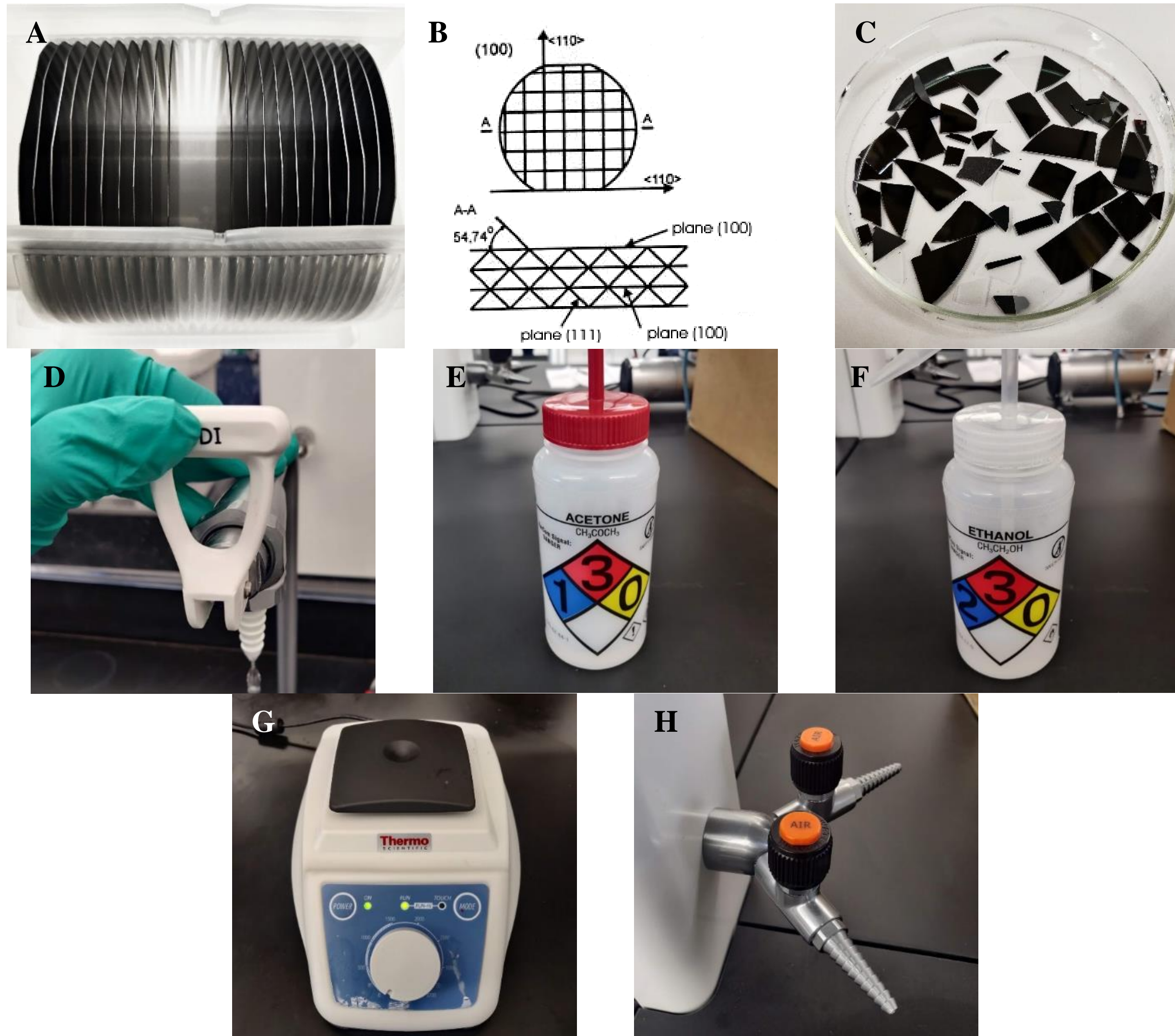

Figure 2.1: Cleaning steps of the Si substrate. A) Si substrate, B) dicing Technique, C) diced Si substrate, D) deionized water tap, E) acetone, F) ethanol, G) shaker and H) air blow nob.

2.1.2 Thin Film Coating by RF Magnetron Sputtering

After cleaning the substrate, the fabrication process began. The main chamber of the sputtering system (AJA ATC Orion 5 UHV) was vacuumed to the scale 10^{-6} Torr to initiate the process. The first step of the sputtering is bias strike. It was done for 10s with 25W RF power, while the pressure in the main chamber was 30mTorr and process gas Ar flow rate was 15sccm. Bias cleaning was done next for 20s with 50W RF power, 3mTorr pressure and 15sccm Ar flow rate.

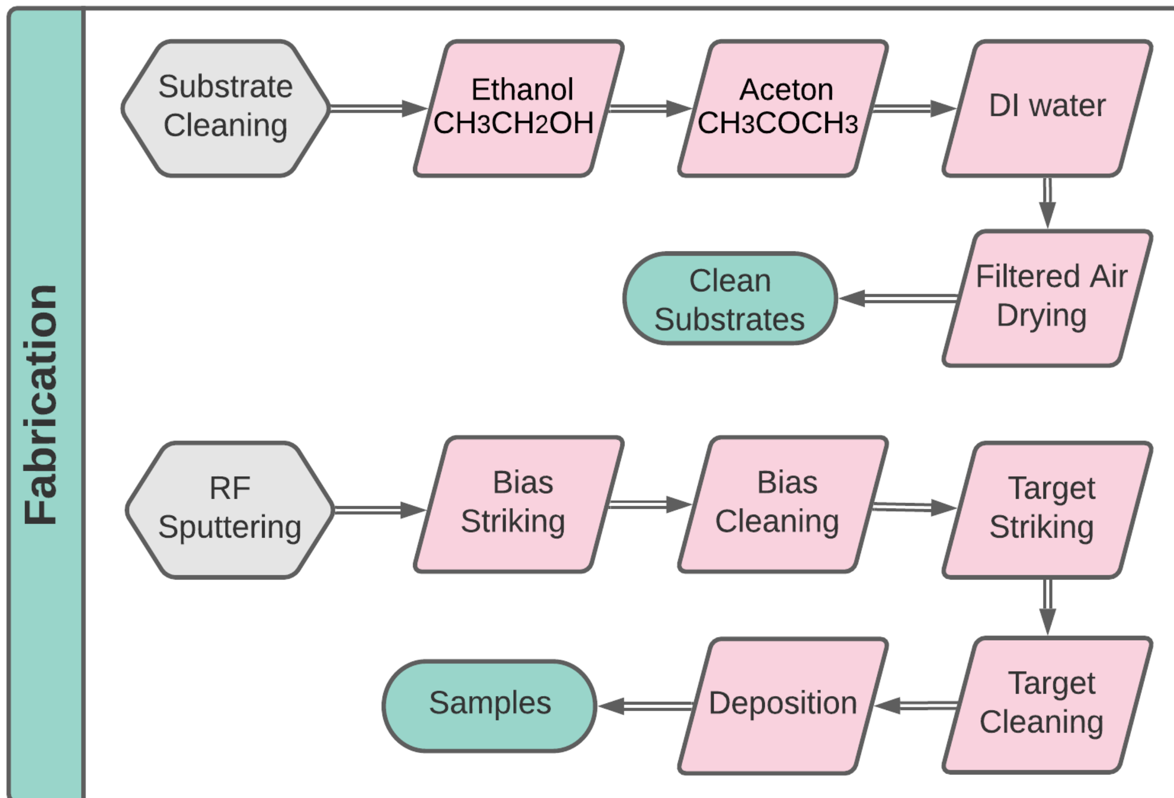

Figure 2.2: Flowchart of the fabrication steps.

A 2" diameter 0.125" thick 99.995% pure SiO_2 and pSi target was used to create thin films. The pSi target was boron doped and the doping concentration was 32 ppm-wt in Si Matrix. Three sets of RF power (150, 200 & 250W- for sputtering SiO_2; 100, 150 & 200 W- for

sputtering pSi), pressure (10, 15 & 20 mTorr) and Ar gas flow rate (5, 10 & 15 sccm) were chosen as process parameters for sputtering. The sets of combinations is given is Taguchi Design of experiment section. RF power was supplied to the sputtering system by 0313 GTC power

Table 2.1: Summary of sputtering process for the thin films

Substrate	pure Si (100), thickness 525±10 µm
Target	SiO_2, diameter -2", thickness- 0.125", purity- 99.995% pSi: Boron doped Si, diameter 2", thickness 0.125", doping concentration 32 ppm-wt in Si Matrix, purity 99.9%
Process Gas	Ar, 99.99% purity
Base Pressure	10^{-6} Torr scale
RF Power Source	13.56 MHz (0313 GTC)
Rotation Speed	36 rpm

source, which has a frequency of 13.56MHz. The targets were subjected to bias strike for 10s with at 30mTorr pressure and 15sccm Ar gas flow rate, while varying the power as according to the sample about to be fabricated from the combination set. SiO_2 and pSi targets was pre-sputtered for 30 mins before commencing the sputtering process. The substrate was being rotated at a constant speed of 36rpm to ensure uniformity of the epitaxial growth. The whole process was remotely monitored by software and the impedance matching network was automatically controlled by an auto-tuner (AIT 600 RF). Each sample was sputtered for 3 hr.

2.2 Characterization

The roughness of the sputtered thin films was measured by Mahr Marsurf 300 C profilometer. XRD analysis was done by Rigaku Miniflex benchtop X-ray diffractometer using a Cu-Kα source of wavelength 1.5406 A° (30KV, 15mA). Surface and cross-sectional micrographs were obtained by scanning electron microscope (Carl Zeiss, Sigma VP). Surface topographic images were obtained using atomic force microscopy (Bruker Bioscope Catalyst). A potentiostat (Metrohm Autolab PGSTAT302N) was used for impedance spectroscopy of the thin films. The Impedance was measured from 1Hz to 1MHz, with a 1V peak to peak sinusoidal signal. Adhesion of the sputtered thin films was performed by scotch tape test.

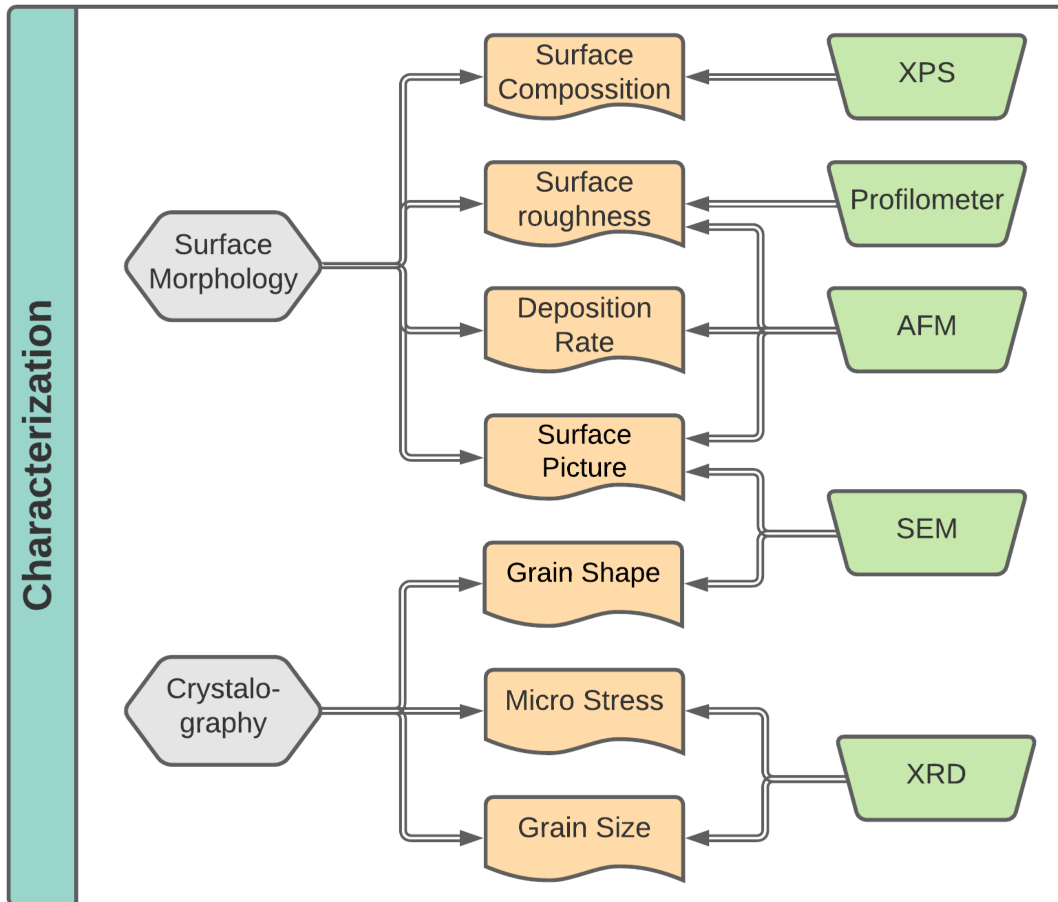

Figure 2.3: Flowchart of characterization of the fabricated thin films

Figure 2.4: SiO_2 (left) and pSi (right) target used for sputtering

2.3 Analysis

Once the characterization data was acquired the statistical analysis- S/N analysis and analysis of variance was performed to understand the effect of individual process parameter on the properties of the thin film. In this section the definitions of the statistical terms is presented.

2.3.1 Taguchi DOE and S/N ratio

Implementing the theory of experimental design and loss function concept, Taguchi design of experiments provides a robust design model [48, 49]. S/N ratio is the most important analysis of Taguchi design. Signals are the controllable process parameters, whereas noise is something we have no control over during production or product use but can be controlled during experimentation. Two types of S/N ratio analysis are applied here-the smaller the better (for surface roughness and $R_{nApSi/Si}$) and the higher the better (for XRD peak of pSi thin films, $R_{nASiO_2/Si}$, $C_{nApSi/Si}$and $C_{nASiO_2/Si}$).

The formula for the smaller-is-better S/N ratio:

$$\frac{S}{N} = -10 \times \log\left(\left(\sum (Y^2)/n\right)\right. \qquad (2.1)$$

The formula for the larger-is-better S/N ratio:

$$\frac{S}{N} = -10 \times \log\left(\left(\sum \frac{1}{Y^2}\right)/n\right) \qquad (2.2)$$

Where Y is responses for the given factor level combination and n is the number of responses in the factor level combination [50].

Three sets of RF power (150, 200 & 250W- for sputtering SiO_2; 100, 150 & 200 W- for sputtering pSi), pressure (10, 15 & 20 mTorr) and Ar gas flow rate (5, 10 & 15 sccm) were chosen as process parameters for sputtering the thin films, which are listed in Table 2.2 and 2.3. 3 level Taguchi design of experiment was applied to create a L^9 (3^3) orthogonal array, which has three columns and nine rows- shown in Table 2.4 and 2.5. Here the fourth column of the L^9 orthogonal array is left vacant for error of experiments [49], as orthogonality is not affected If one column of the array is empty [51, 52]. The nine sets of combinations of process parameters for fabricating SiO_2/Si and pSi/Si samples are charted in Table 2.4 and 2.5 respectively.

Table 2.2: Sputtering parameters for SiO_2/Si thin films

Level	Sputtering parameter	1	2	3
A	RF Power (W)	150	200	250
B	Pressure (mTorr)	10	15	20
C	Ar flow rate (sccm)	5	10	15

Table 2.3: Sputtering parameters for pSi/Si thin films

Level	Sputtering parameter	1	2	3
A	RF Power (W)	100	150	200
B	Pressure (mTorr)	10	15	20
C	Ar flow rate (sccm)	5	10	15

Table 2.4: 9 sets of parameter combinations from Taguchi L^9 orthogonal array for sputtering SiO_2/Si thin films

Sample number	Control factors		
	Power (W) (A)	Pressure (mTorr) (B)	Ar flow rate (sccm) (C)
SiO_2 Sample 1	150 (1)	10 (1)	5 (1)
SiO_2 Sample 2	150 (1)	15 (2)	10 (2)
SiO_2 Sample 3	150 (1)	20 (3)	15 (3)
SiO_2 Sample 4	200 (2)	10 (1)	10 (2)
SiO_2 Sample 5	200 (2)	15 (2)	15 (3)
SiO_2 Sample 6	200 (2)	20 (3)	5 (1)
SiO_2 Sample 7	250 (3)	10 (1)	15 (3)
SiO_2 Sample 8	250 (3)	15 (2)	5 (1)
SiO_2 Sample 9	250 (3)	20 (3)	10 (2)

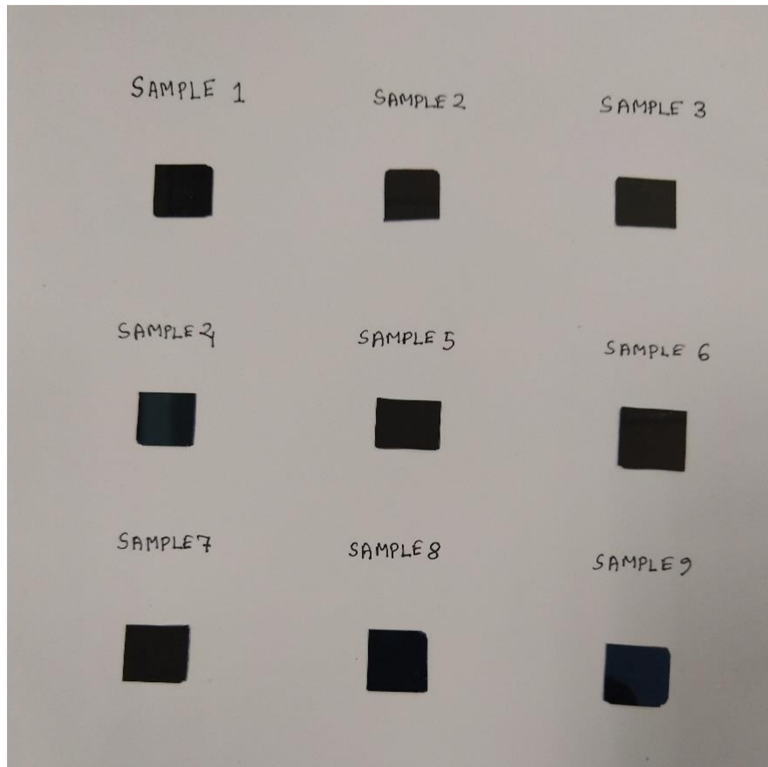

Figure 2.5: 9 RF sputtered SiO_2/Si thin film samples

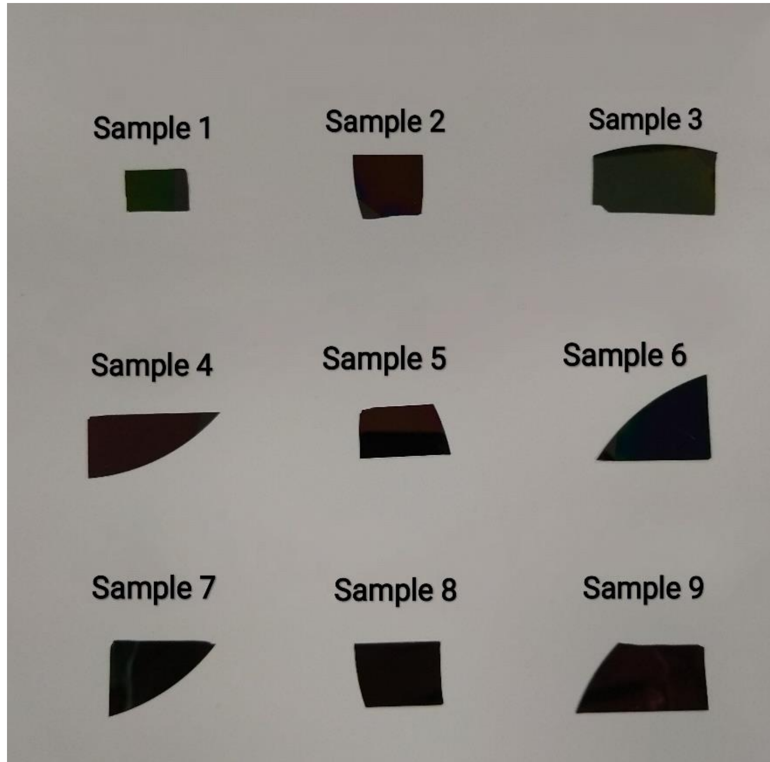

Figure 2.6: 9 RF sputtered SiO_2/Si thin film samples

It should be mentioned that sputtering of SiO_2 and pSi was attempted with 5mTorr working pressure but the plasma failed to generate during sputtering. That is why entry level of working pressure for sputtering the thin films was chosen 10mTorr.

Table 2.5: 9 sets of parameter combinations from Taguchi L^9 orthogonal array for sputtering pSi/Si thin films

Sample number	Control factors		
	Power (W) (A)	Pressure (mTorr) (B)	Ar flow rate (sccm) (C)
pSi Sample 1	100 (1)	10 (1)	5 (1)
pSi Sample 2	100 (1)	15 (2)	10 (2)
pSi Sample 3	100 (1)	20 (3)	15 (3)
pSi Sample 4	150 (2)	10 (1)	10 (2)
pSi Sample 5	150 (2)	15 (2)	15 (3)
pSi Sample 6	150 (2)	20 (3)	5 (1)
pSi Sample 7	200 (3)	10 (1)	15 (3)
pSi Sample 8	200 (3)	15 (2)	5 (1)
pSi Sample 9	200 (3)	20 (3)	10 (2)

2.3.2 Analysis of Variance (ANOVA)

ANOVA was performed to find out which sputtering parameter has a statistically significant effect over a particular output. Two important calculation regarding ANOVA analysis

is F-value and P-value, which indicates the corresponding parameter having a significant impact on response characteristics.

F value indicates if the means between two populations are significantly different. If F is large, the variability between treatments is large relative to the variation within treatments, and we reject the null hypothesis of equal means.

$$F = \frac{Variance\ between\ Treatments}{Variance\ within\ Treatments} \quad (2.3)$$

To determine whether any of the differences between the means are statistically significant, a significant level (α)- indicating a 100α% risk of concluding that a difference exists when there is no actual difference in treatment-is chosen. If the P-value ≤ α, then it means the differences between some of the means are statistically significant.

The following equations were used for ANOVA and F-test of the experimental data [49]:

$$S_{mean} = \frac{(\sum x_i)^2}{n} \qquad S_{Error} = S_{TV} - \sum S_p$$
$$S_{TV} = \sum x_i^2 - S_{mean} \qquad V_p = \frac{S_p}{f_p} \qquad (2.4)$$
$$S_p = \frac{(\sum x_p^2)^2}{n_{rpt}} - S_{mean} \qquad F_p = \frac{V_P}{V_{Error}}$$

Where the total number of experiments is N, x_i denotes the output of each experiment, S_{mean} is the sum of squares due to the means, S_{TV} means the sum of square due to the total variation, S_p stands for sum of square due to a parameter, x_p is the sum of the ith level of a parameter (here i=1,2,3), f_p degree of freedom of parameter P, V_p the variance of parameter P and F_p is the F-value of parameter P.

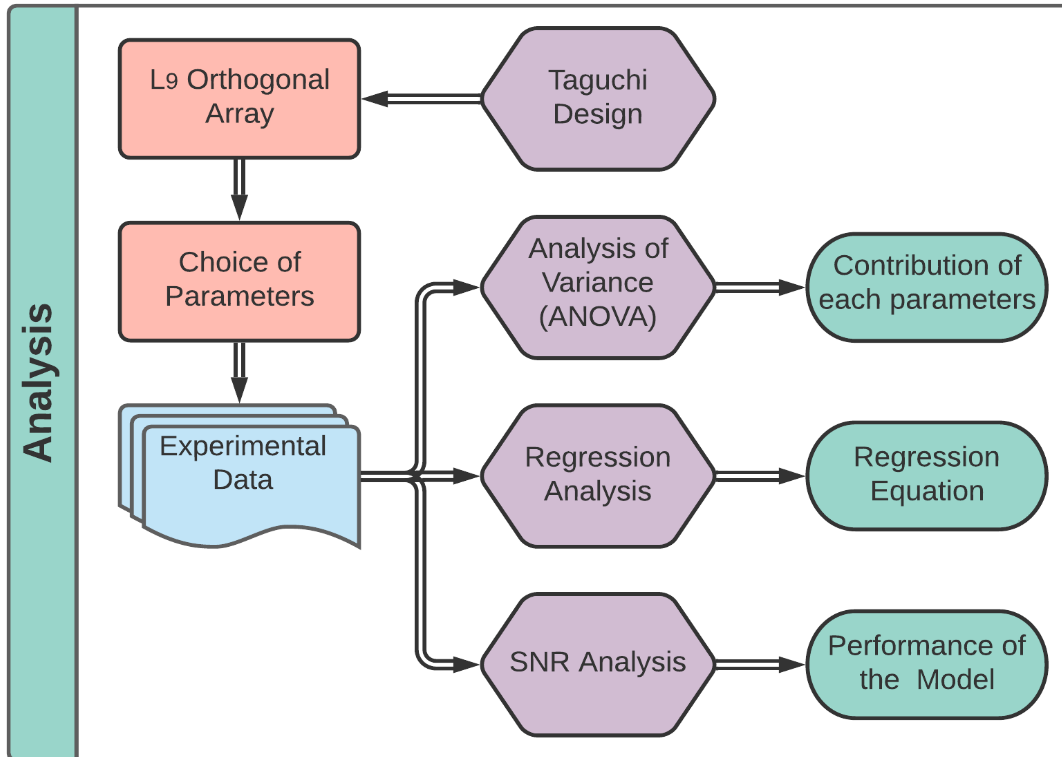

Figure 2.7: Flowchart of performing statistical analysis

2.3.3 Regression Analysis

The purpose of regression analysis is to generate an equation that describes the relationship between the dependent and independent variables and can predict a new observation. A general first-order regression equation can be expressed as follows-

$$y = \beta_0 + \sum_{i=1}^{k} \beta_i x_i + \varepsilon \qquad (2.5)$$

Where β represents the coefficient of each term, k is the number of independent variables and the error is designated by ε.

Short description of notation used in regression analysis is given below [53]:

S calculates the deviation of distances of the data values from the fitted values.

R^2 denotes the variation of the actual response from the fitted model.

R^2(adj) adjusts the statistic based on the number of independent variables in the model.

R^2(pred) predicts the efficiency of the model for a new observation.

The statistical analysis in this research was performed in Minitab software.

CHAPTER III

CHARACTERIZTION OF SiO_2/Si THIN FILMS

The following experiments of characterization of nine samples SiO_2/Si thin films were conducted in this research.

- ✓ Surface Roughness
- ✓ XRD analysis
- ✓ Surface morphology
- ✓ Surface topology
- ✓ Electrical properties (resistance per unit area ($R_{nASiO_2/Si}$) and capacitance per unit area ($C_{nASiO_2/Si}$).

In this chapter the results and discussions of these experiments are presented.

3.1 Surface Roughness of SiO_2/Si Thin Films

Surface roughness for sputtered SiO_2 thin film is important; for optoelectronic devices where these thin films are used as anti-reflection coating, rough surface will cause more scattering of light and henceforth will decrease the efficiency of the device. Roughness is the result of micro-voids and pores on the sputtered thin-film surface. The average surface roughness R_a for the sputtered SiO_2/Si thin film samples is listed in Table 3 .1. Figure 3 .1 shows the S/N

graph for the surface roughness. As it can be seen, roughness increased when working pressure was increased but decreased with increasing power, which agrees well with the theory.

Table 3.1: Summary of surface roughness (R_a) of SiO_2/Si thin films

Sample No.	Roughness R_a (nm)
SiO_2 Sample 1	14.0
SiO_2 Sample 2	14.3
SiO_2 Sample 3	15.2
SiO_2 Sample 4	13.6
SiO_2 Sample 5	13.8
SiO_2 Sample 6	15.0
SiO_2 Sample 7	13.0
SiO_2 Sample 8	13.4
SiO_2 Sample 9	14.4

When the power is high, the process gas atoms bombard against the target with high kinetic energy- this high energy bombardment, known as atomic peening [12, 54]. Atomic peening excites the falling target atoms, generates more nucleation sites and therefore forming a densely packed structure, filling up most of the micro-voids and pores on the surface. Working pressure, on the other hand, has the opposite effect. Higher pressure means less mean free path, so the interatomic collisions between the process gas atoms and falling target atoms diminish the average kinetic energy. A loosely packed structure with high porosity builds up over the substrate as a result.

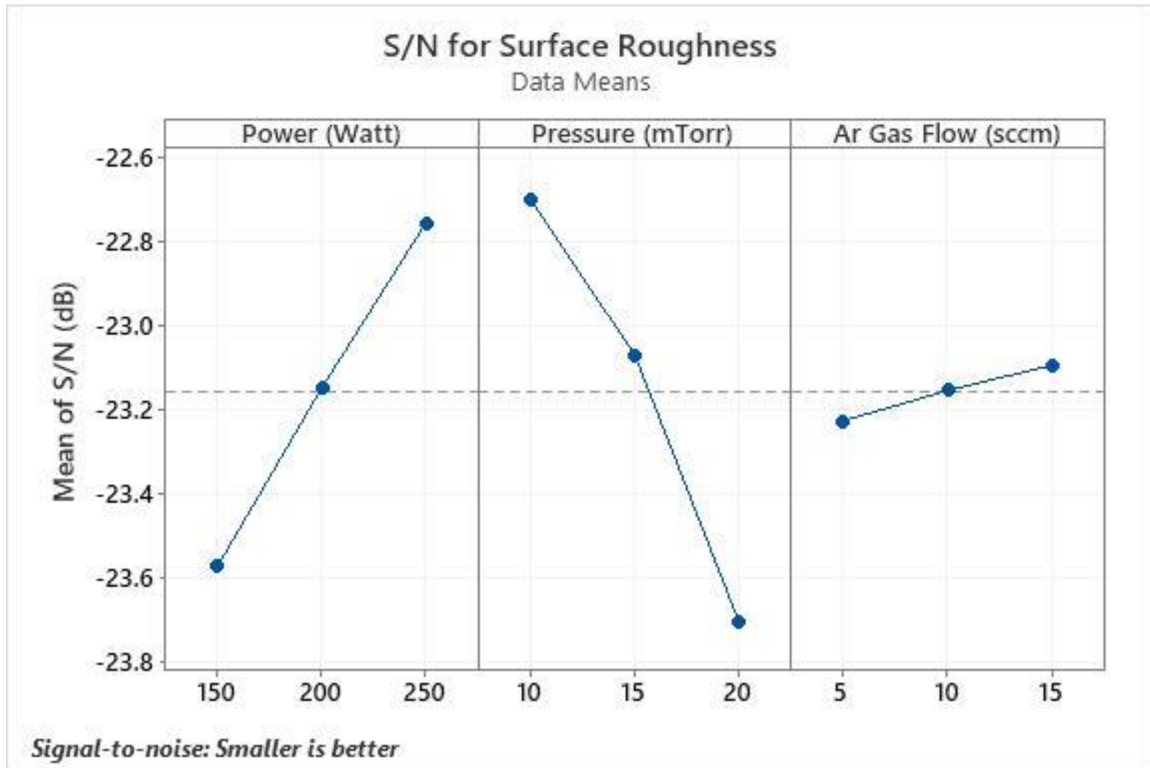

Figure 3.1: S/N response graph for surface roughness of SiO_2/Si thin films

Table 3.2: Summary of ANOVA result for surface roughness (R_a) of SiO_2/Si thin films

Source	DF	Seq SS	Contribution	Adj SS	Adj MS	F-Value	P-Value
Power (Watt)	2	2.73620	37.88%	2.73620	1.36810	27.96	0.035
Pressure (mTorr)	2	4.33687	60.04%	4.33687	2.16843	44.31	0.022
Ar Gas Flow (sccm)	2	0.05287	0.73%	0.05287	0.02643	0.54	0.649
Error	2	0.09787	1.35%	0.09787	0.04893		
Total	8	7.22380	100.00%				

From the analysis of variance of our data (Table 3.2), we can conclude that the contribution of pressure is dominant (60.04%) to the surface roughness compared to the working pressure (37.88%). Although from Figure 3.1, we observed that roughness decreases when Ar gas flow rate is increased, which agrees with previous work [55], ANOVA result however showed that this contribution is not significant at all (P-value > 0.05).

A regression model was derived in case a thin film with a particular roughness is desired. The model summary of the regression analysis is listed in Table 3.3.

$$\text{Roughness } (R_a) \text{ (nm)} = 14.782 - 0.01350 \text{ Power (Watt)} + 0.1677 \text{ Pressure (mTorr)} - 0.0183 \text{ Ar Gas Flow (sccm)} \quad (3.1)$$

Table 3.3: Summary of the regression analysis of surface roughness of SiO_2/Si thin films

S	R-sq	R-sq(adj)	R-sq(pred)
0.211100	96.92%	95.06%	89.14%

3.2 XRD Analysis of SiO_2/Si Thin Films

The XRD patterns of the SiO_2/Si thin film samples (sample 1-sample 9) is shown in Figure 4.2. No peak was detected in all sample scanned from position θ=20° to θ=65°, which led to the conclusion that the deposited SiO_2 layers were amorphous. According to PDF #81-0066 card, if the layered SiO_2 film was crystallized, there would be some conspicuous peaks at θ = 27.3° or θ = 21.6°, indicating quartz (011) or (100) plane respectively [19], which was not the case. A strong peak was detected at position θ=69.1° for each of the samples, but this peak is related to the Si (100) substrate. The amorphous deposited layers of SiO_2 were also reported in

previous literature [19, 29]. The XRD peak intensities in count per second (cps) and peak positions of each sample were tabulated in Table 3.4.

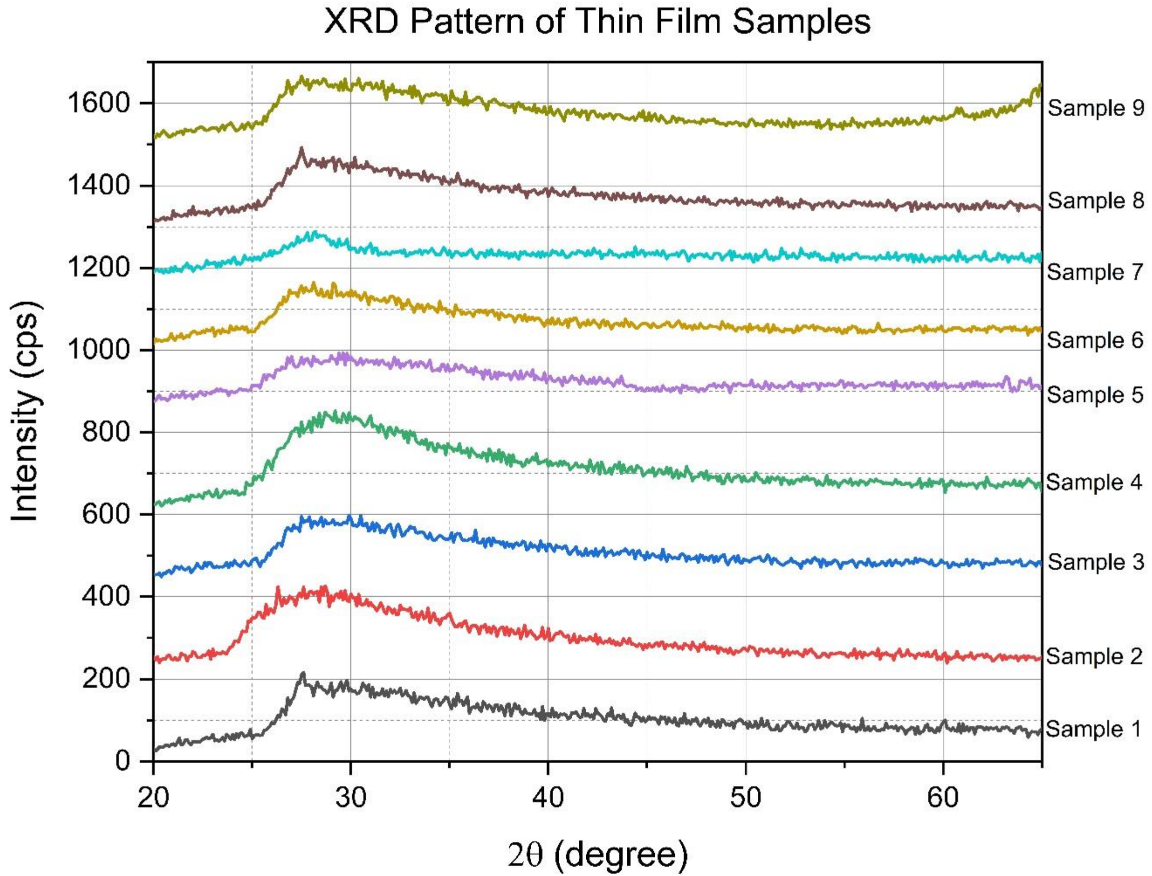

Figure 3.2: XRD pattern of SiO2/Si thin film samples presented in stacked lines by Y offset

Peak positions were obtained between θ= 27.5° to 29.9° range and peak intensities varied arbitrarily from 134 cps (sample 7) to 259.5 cps (sample 4), following no trend. Because of these amorphous XRD patterns, no further information like grain size and micro stress could be derived for the nine SiO_2/Si thin film samples.

Table 3.4: Summary of surface and crystallographic information of SiO_2/Si thin films

Sample No.	Peak position θ/2θ (degree)	Peak intensity (cps)
SiO_2 Sample 1	27.6	216
SiO_2 Sample 2	28.7	240
SiO_2 Sample 3	29.9	177
SiO_2 Sample 4	29.2	259.5
SiO_2 Sample 5	29.6	149.5
SiO_2 Sample 6	28.1	173
SiO_2 Sample 7	28.2	134
SiO_2 Sample 8	27.5	209.5
SiO_2 Sample 9	27.5	181.5

3.3 Surface Morphology & Surface Topography of SiO_2/Si Thin Films

Figure 3.3 depicts surface and cross-sectional SEM images of samples 3,4 and 8 of SiO_2/Si thin films. The surface of sample 3 displayed no ditches, whereas ditch-like morphology appeared on the surface of samples 4 and 8. No pronounced granular shape was noticed in all three samples. This kind of surface morphology was also described in Zhao et al. [19]. Although Zhao et al. attributed the presence of ditches on the sample surface to the decreasing process gas pressure, in this observation, however, the contribution of sputtering power was more profound. Trenches appeared most clearly on the surface of sample 8, which was deposited with the highest RF sputtering power (250 Watt). Sample 4 deposited with 200 Watt RF power showed less visible ditches.

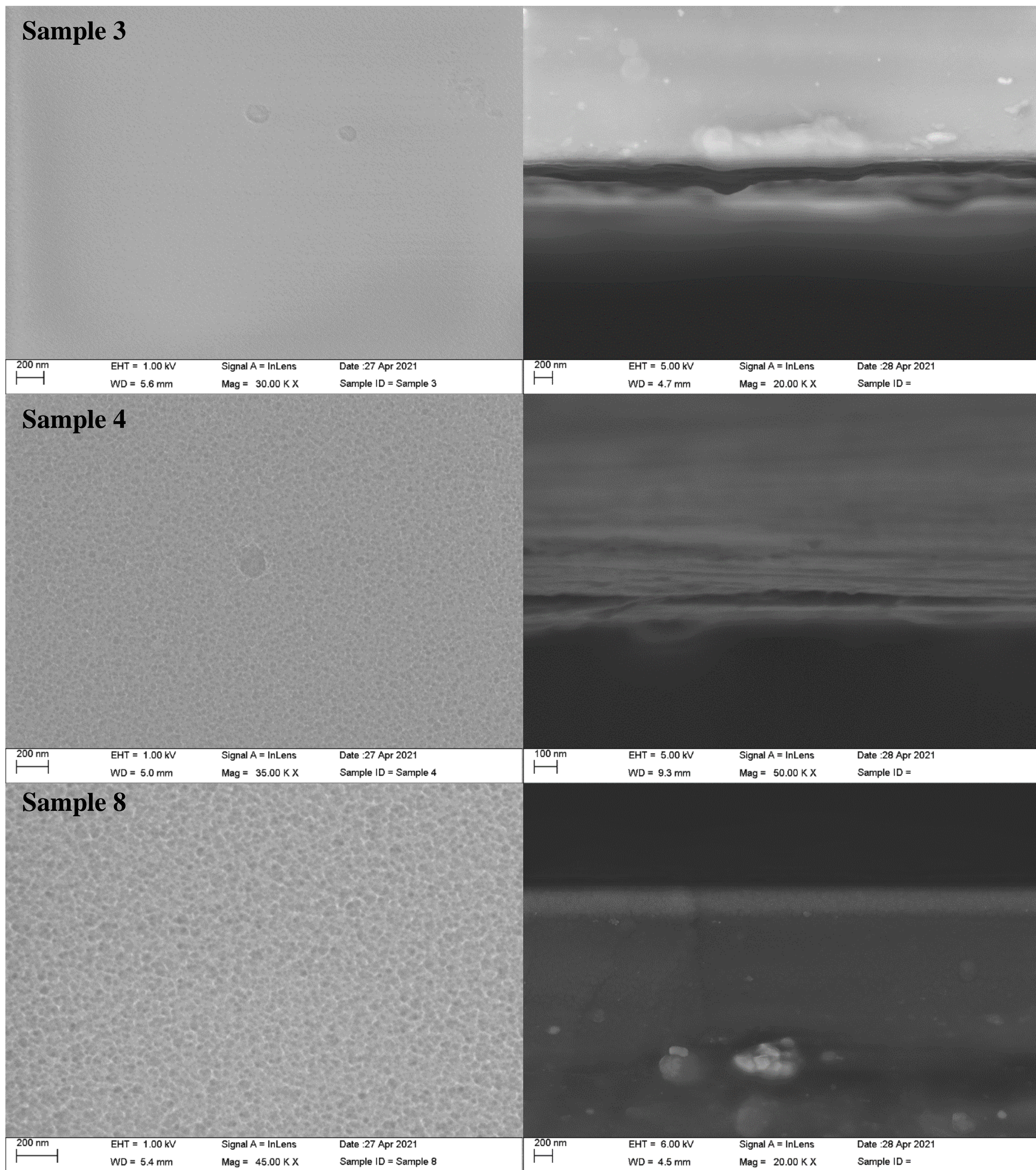

Figure 3.3: Surface (left) and cross-sectional (right) SEM micrograph of the SiO_2/Si thin film samples. SiO_2 Sample 3 in top, SiO_2 Sample 4 in middle and SiO_2 Sample 8 in bottom row.

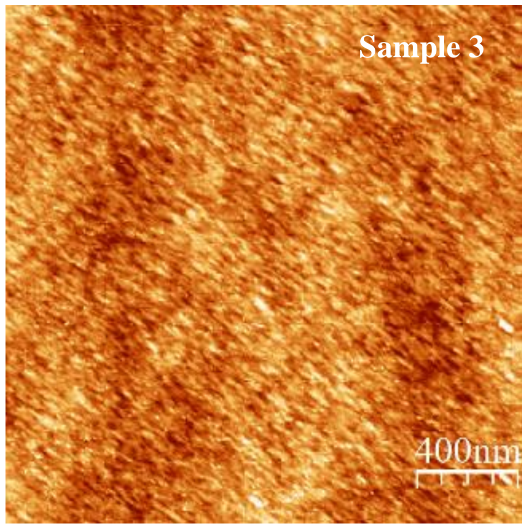

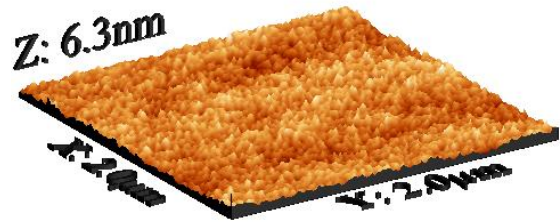

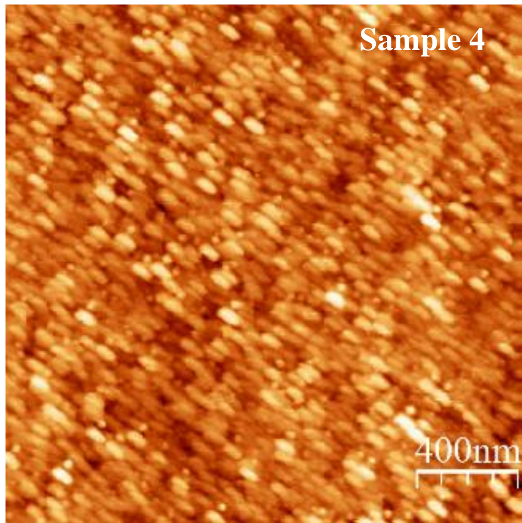

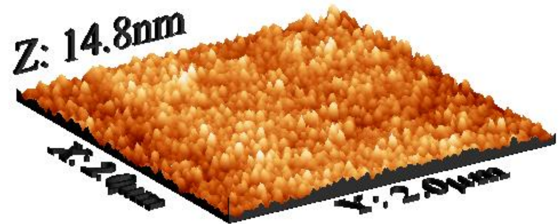

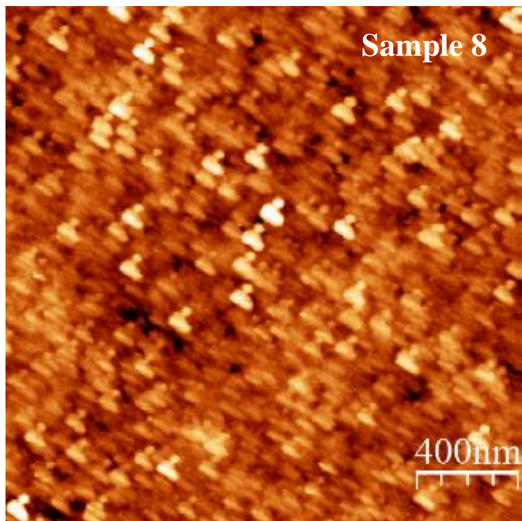

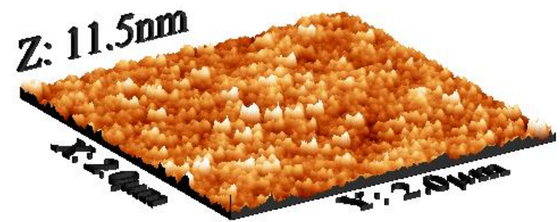

Figure 3.4: AFM images (left 2d and right 3d) of the SiO_2/Si thin film samples

SEM cross-sectional images did not provide enough information. One reason for this was the deposited layers were not thick enough for the micro-structures to be visible. The cross-sectional SEM image of sample 8 vaguely showed domain-like shapes with no columnar microstructure. 2D and 3D AFM images of surface topographies of samples 3, 4 and 8 are shown in Figure 3.4.

3.4 Electrical Properties of SiO_2/Si Thin Films

Electrical properties (resistance per unit area $R_{nASiO_2/Si}$, and capacitance per unit area $C_{nASiO_2/Si}$) of SiO_2/Si thin films were examined with impedance spectroscopy. Impedance spectroscopy gives bode plot (impedance $Z_{nSiO_2/Si}$ & phase angle vs. frequency) and nyquist plot ($Z_{nSiO_2/Si}$ (img) vs. $Z_{nSiO_2/Si}$ (real)) of the films.

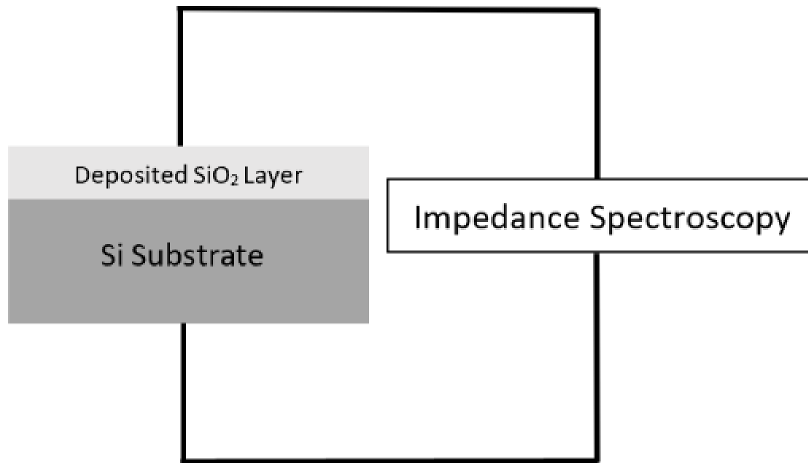

Figure 3.5: Connection diagram SiO_2/Si thin film samples for impedance spectroscopy measurement

$Z_{nSiO_2/Si}$ (real) can be attributed to resistance of the thin film and the capacitance of the SiO_2/Si thin film contributes to the $Z_{nSiO_2/Si}$ (img) part of the impedance spectroscopy.

To get the resistance and capacitance of the nth sample, we used the following equations.

$$R_{nSiO_2/Si} = Z_{nASiO_2/Si}(real)$$
$$C_{nSiO_2/Si} = \frac{1}{2\pi f Z_{nASiO_2/Si}(img)} \qquad (3.2)$$

Where f is the frequency. Now, as from the connection in Figure 3.5, the deposited SiO_2 superstrate and the Si substrate are in series. So, we can write the following equations:

$$R_{nSiO_2/Si} = R_{Si} + R_{nSiO_2}$$
$$\frac{1}{C_{nSiO_2/Si}} = \frac{1}{C_{Si}} + \frac{1}{C_{nSiO_2}} \qquad (3.3)$$

Further we can write:

$$\frac{R_{nSiO_2/Si}}{A_n} = \frac{R_{Si}}{A_n} + \frac{R_{nSiO_2}}{A_n}$$

Or,

$$R_{nASiO_2/Si} = \frac{R_{Si}}{A_n} + \frac{R_{nSiO_2}}{A_n}$$

And, (3.4)

$$\frac{1}{\frac{C_{nSiO_2/Si}}{A_n}} = \frac{1}{\frac{C_{Si}}{A_n}} + \frac{1}{\frac{C_{nSiO_2}}{A_n}}$$

Or,

$$\frac{1}{C_{nASiO_2/Si}} = \frac{1}{\frac{C_{Si}}{A_n}} + \frac{1}{\frac{C_{nSiO_2}}{A_n}}$$

Now, R_{Si} and C_{Si} are both constant for a particular frequency, which makes $\frac{R_{Si}}{A_n}$ and $\frac{C_{Si}}{A_n}$ also constant. Thus, for a particular frequency, the changes of $R_{nSiO_2/Si}$ and $C_{nSiO_2/Si}$ are simply due to the change in R_{nSiO_2} and C_{nSiO_2}. Process parameters variation during sputtering changes the structure of the

deposited SiO_2 thin film over Si substrate and therefore, the electrical properties of the thin films change with it. Each sample was deposited for 3hours, so deposition time was not a parameter for our observation.

Table 3.5: Summary of electrical properties of SiO_2/Si thin film samples

Sample No.	$R_{nASiO_2/Si}$ at 50kHz (Ω/cm^2)	$C_{nASiO_2/Si}$ at 50kHz (μF/cm^2)	$R_{nASiO_2/Si}$ at 10kHz (Ω/cm^2)	$C_{nASiO_2/Si}$ at 10kHz (μF/cm^2)
SiO_2 Sample 1	2.69×10^{4}	5.24×10^{-6}	4.82×10^{4}	5.83×10^{-6}
SiO_2 Sample 2	3.48×10^{4}	5.92×10^{-6}	6.16×10^{4}	6.60×10^{-6}
SiO_2 Sample 3	2.81×10^{4}	6.12×10^{-6}	5.62×10^{4}	6.95×10^{-6}
SiO_2 Sample 4	1.44×10^{4}	6.56×10^{-6}	3.13×10^{4}	7.01×10^{-6}
SiO_2 Sample 5	2.75×10^{4}	7.49×10^{-6}	4.54×10^{4}	8.56×10^{-6}
SiO_2 Sample 6	1.93×10^{4}	7.24×10^{-6}	3.35×10^{4}	8.43×10^{-6}
SiO_2 Sample 7	2.62×10^{4}	3.69×10^{-6}	5.62×10^{4}	3.96×10^{-6}
SiO_2 Sample 8	3.52×10^{4}	4.75×10^{-6}	5.59×10^{4}	5.17×10^{-6}
SiO_2 Sample 9	2.16×10^{4}	4.06×10^{-6}	3.38×10^{4}	4.46×10^{-6}

Figure 3.6-3.8 shows the impedance spectroscopy result and Figure 3.9- 3.17 shows the resistance/area ($R_{nSiO_2/Si}$) and capacitance/area ($C_{nSiO_2/Si}$) vs. frequency plots for sample 1-9. Normalizing with sample area (A_n) was intentionally carried out to omit the area difference effect on the electrical properties. In all cases, $R_{nSiO_2/Si}$ and $C_{nSiO_2/Si}$decreased with increasing frequency. Table 3.5 shows $R_{nSiO_2/Si}$and $C_{nSiO_2/Si}$ at 50kHz and 10kHz.

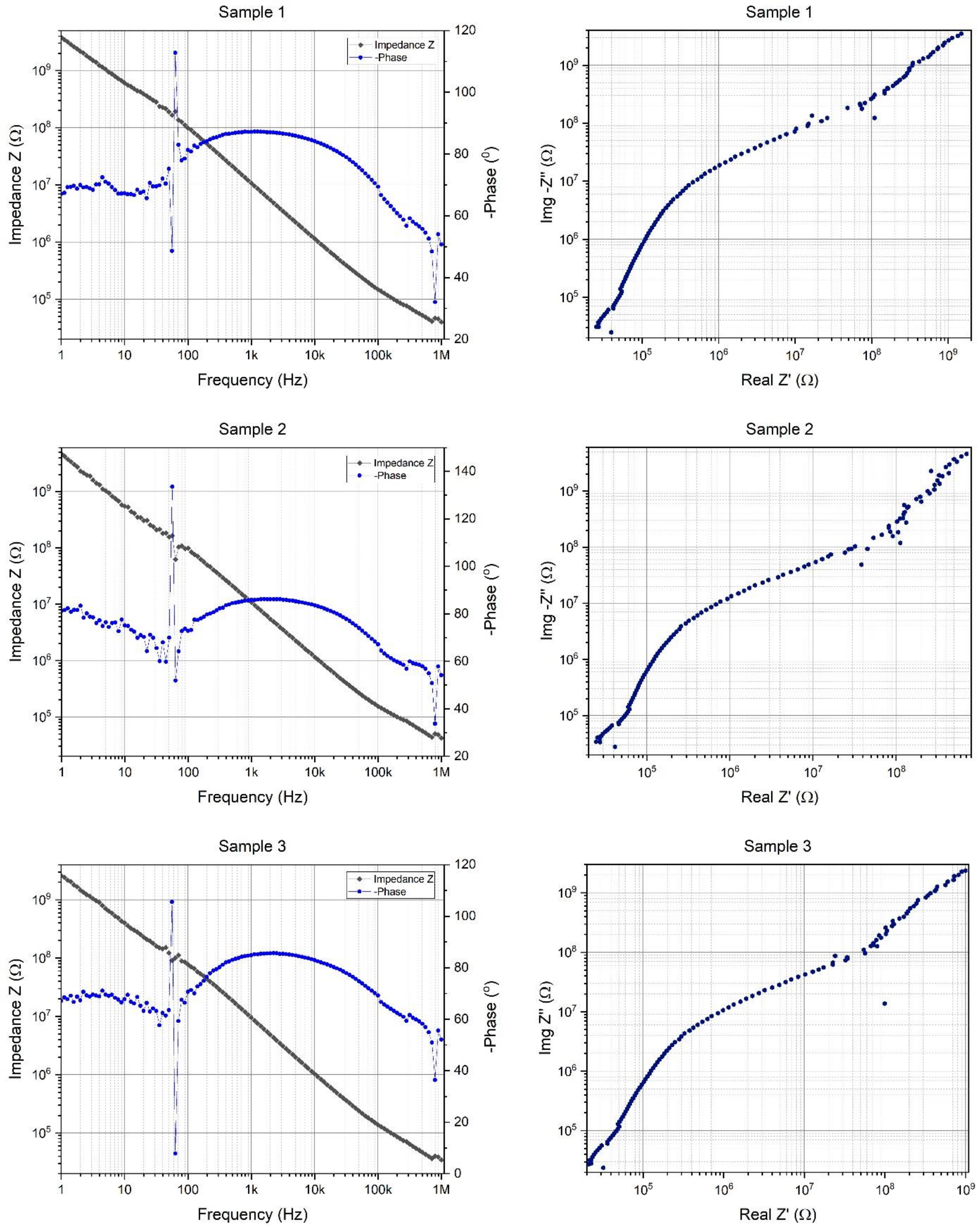

Figure 3.6: Bode plots (right) and Real Z' vs Img Z'' scatter plot (left) for SiO_2/Si thin film sample 1-3

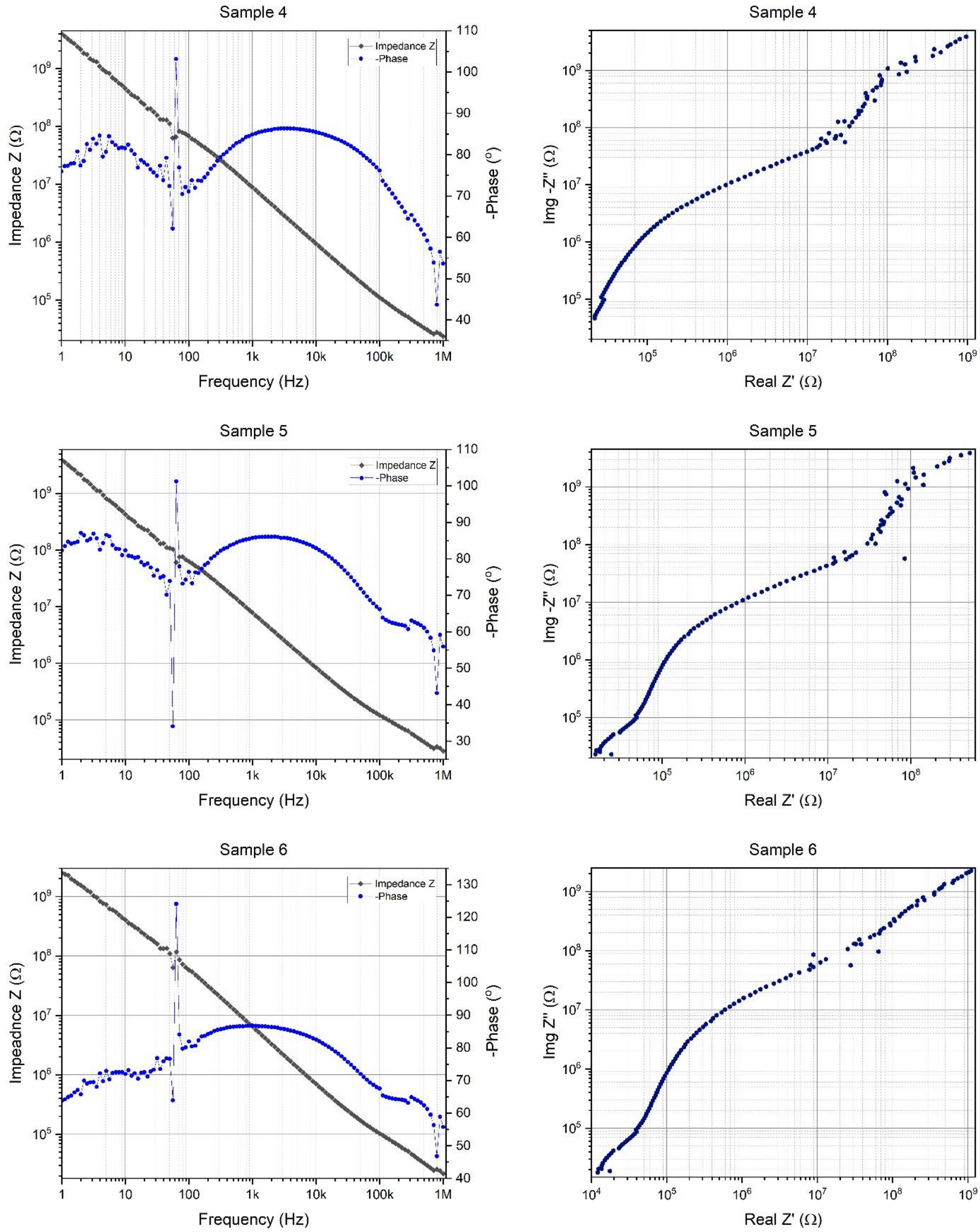

Figure 3.7: Bode plots (right) and Real Z' vs Img Z'' scatter plot (left) for SiO_2/Si thin film sample 4-6

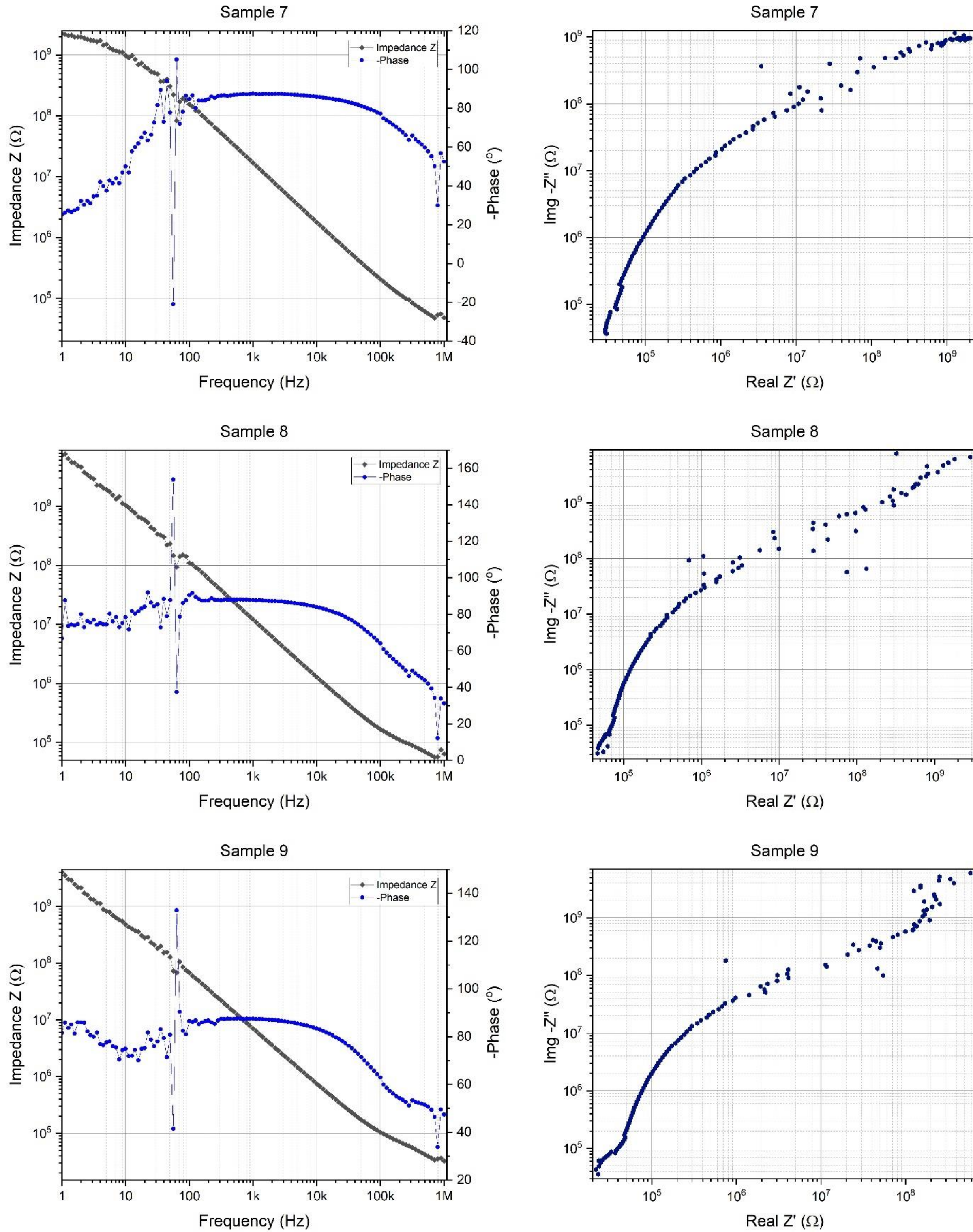

Figure 3.8: Bode plots (right) and Real Z' vs Img Z'' scatter plot (left) for SiO_2/Si thin film sample 7-9

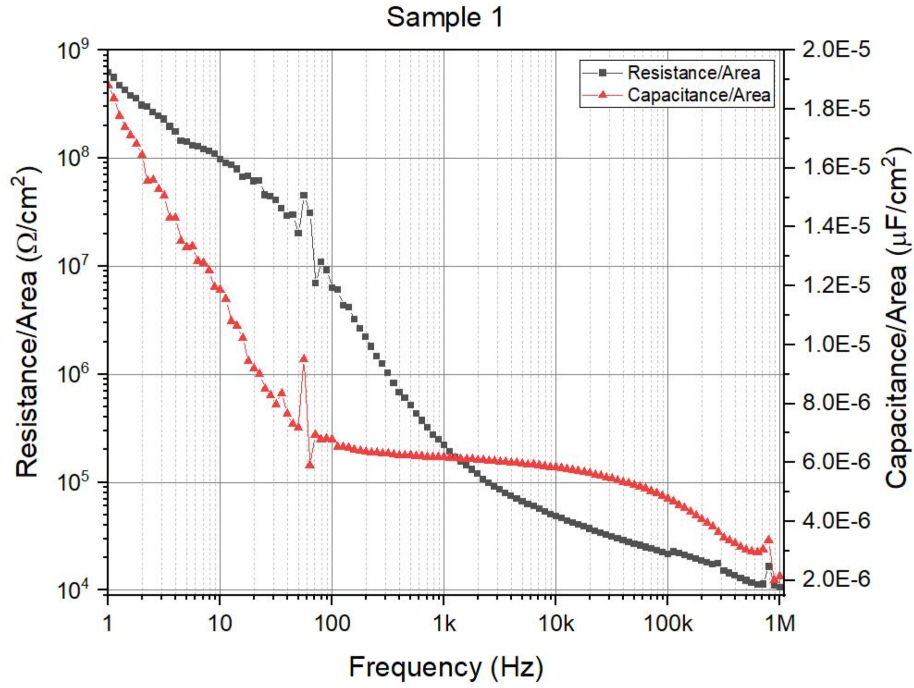

Figure 3.9: Resistance/area ($R_{nASiO_2/Si}$) and capacitance/area ($C_{nASiO_2/Si}$) vs. frequency plots for SiO_2/Si Sample 1

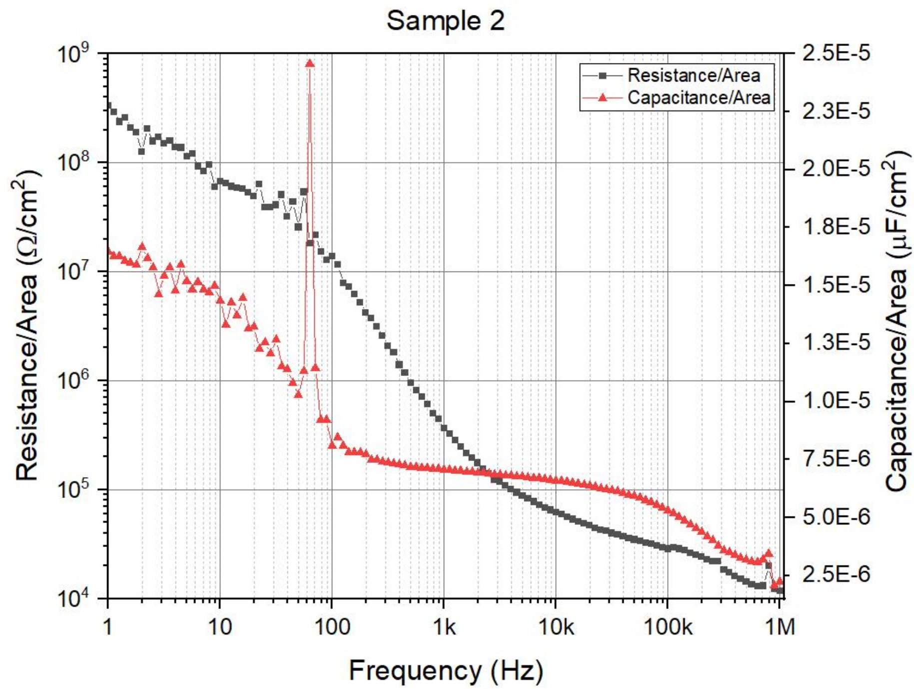

Figure 3.10: Resistance/area ($R_{nASiO_2/Si}$) and capacitance/area ($C_{nASiO_2/Si}$) vs. frequency plots for SiO_2/Si Sample 2

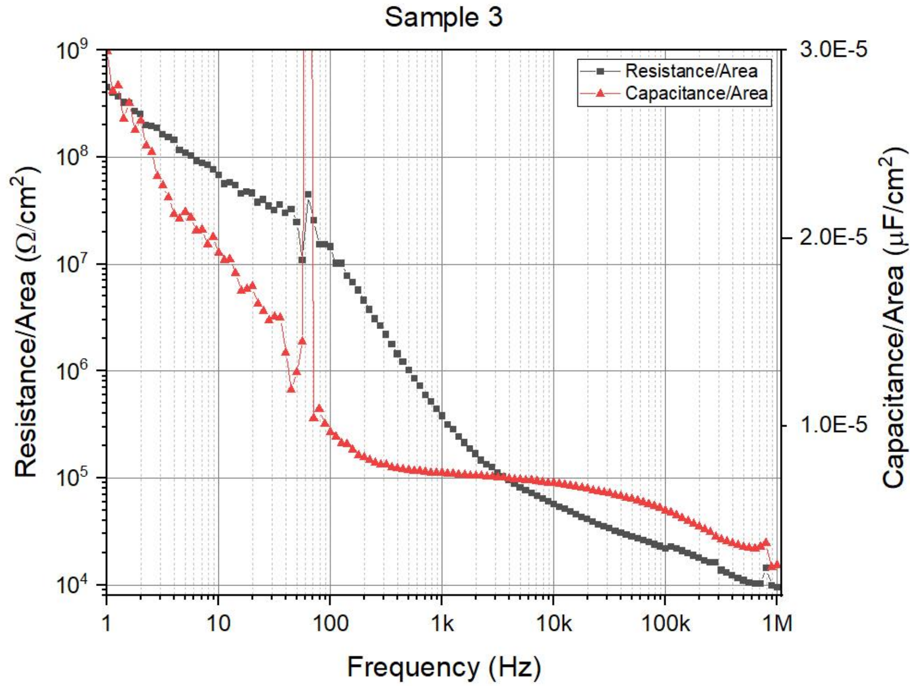

Figure 3.11: Resistance/area ($R_{nASiO_2/Si}$) and capacitance/area ($C_{nASiO_2/Si}$) vs. frequency plots for SiO_2/Si Sample 3

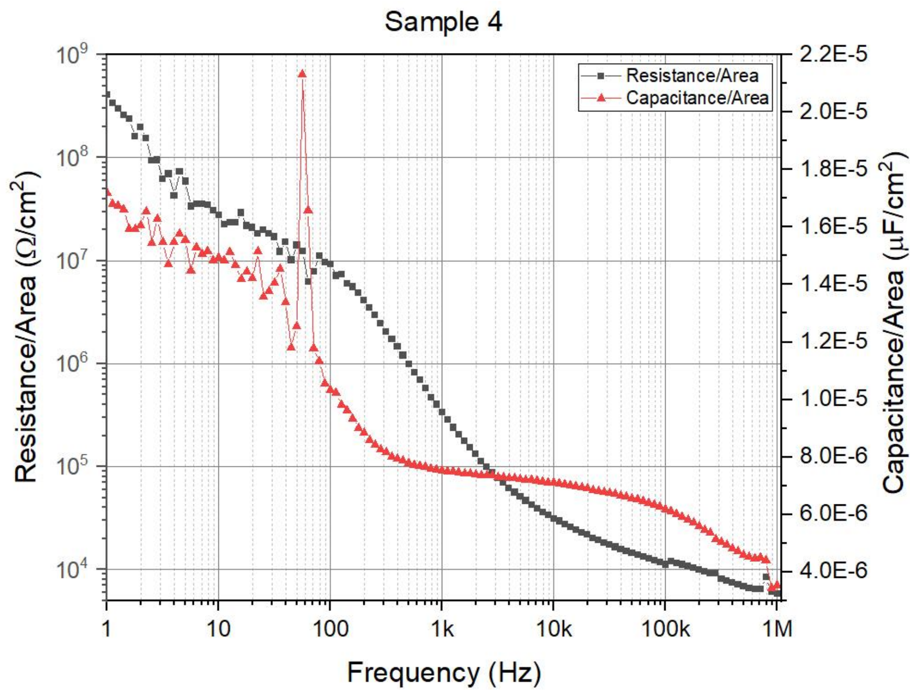

Figure 3.12: Resistance/area ($R_{nASiO_2/Si}$) and capacitance/area ($C_{nASiO_2/Si}$) vs. frequency plots for SiO_2/Si Sample 4

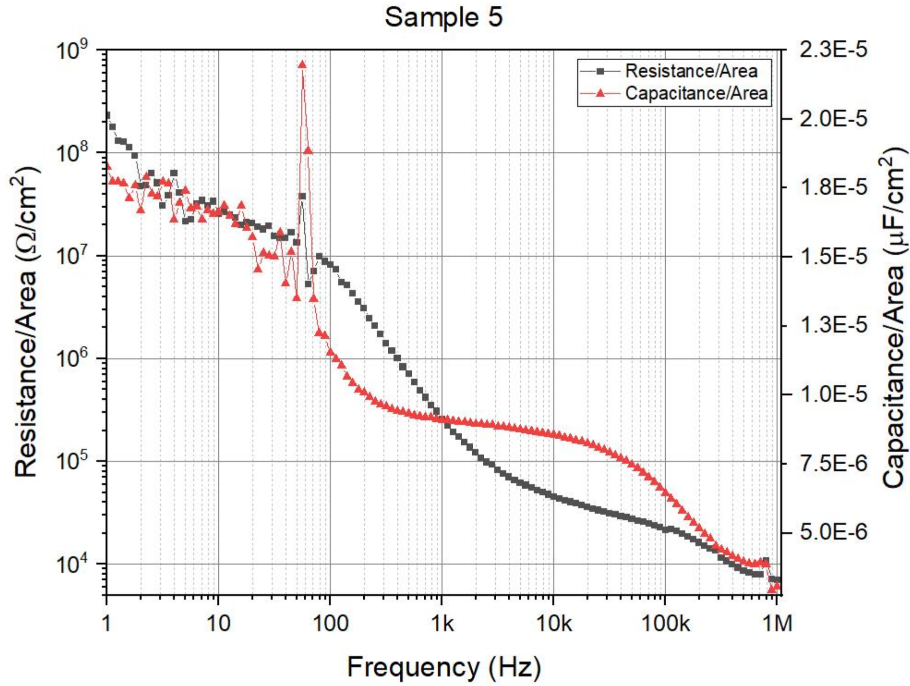

Figure 3.13: Resistance/area ($R_{nASiO_2/Si}$) and capacitance/area ($C_{nASiO_2/Si}$) vs. frequency plots for SiO_2/Si Sample 5

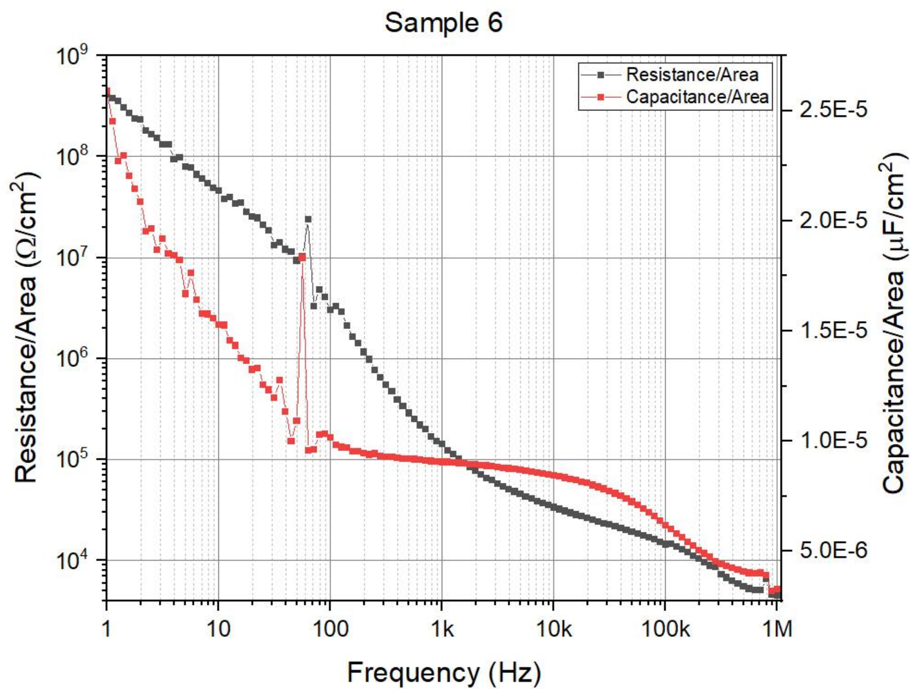

Figure 3.14: Resistance/area ($R_{nASiO_2/Si}$) and capacitance/area ($C_{nASiO_2/Si}$) vs. frequency plots for SiO_2/Si Sample 6

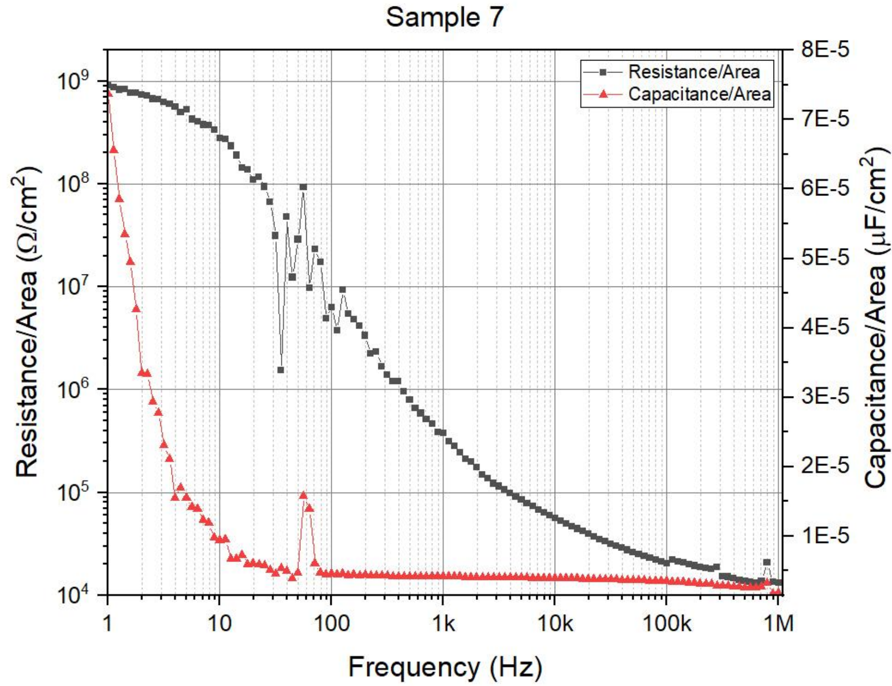

Figure 3.15: Resistance/area ($R_{nASiO_2/Si}$) and capacitance/area ($C_{nASiO_2/Si}$) vs. frequency plots for SiO_2/Si Sample 7

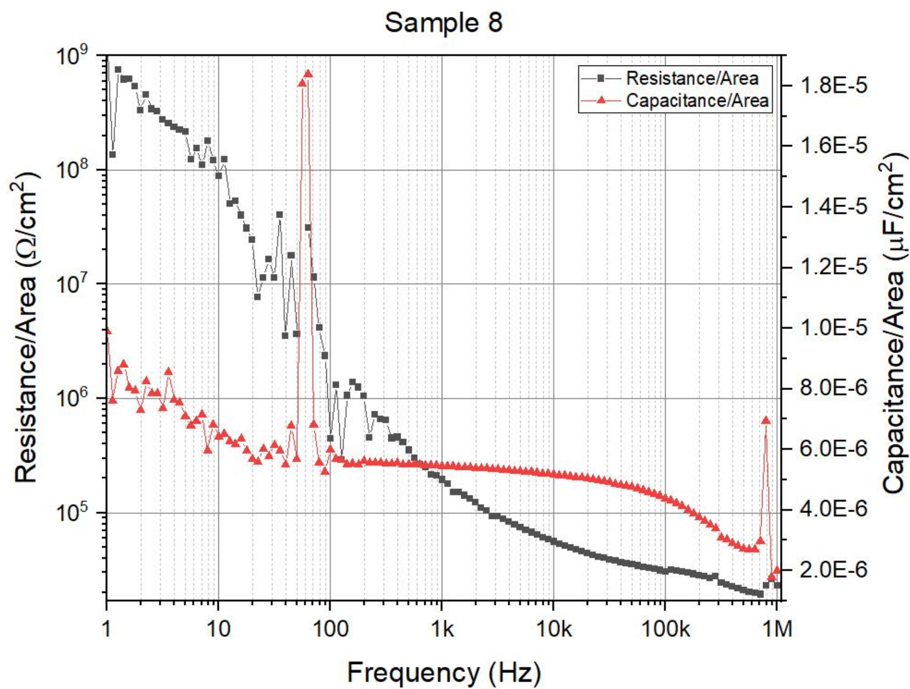

Figure 3.16: Resistance/area ($R_{nASiO_2/Si}$) and capacitance/area ($C_{nASiO_2/Si}$) vs. frequency plots for SiO_2/Si Sample 8

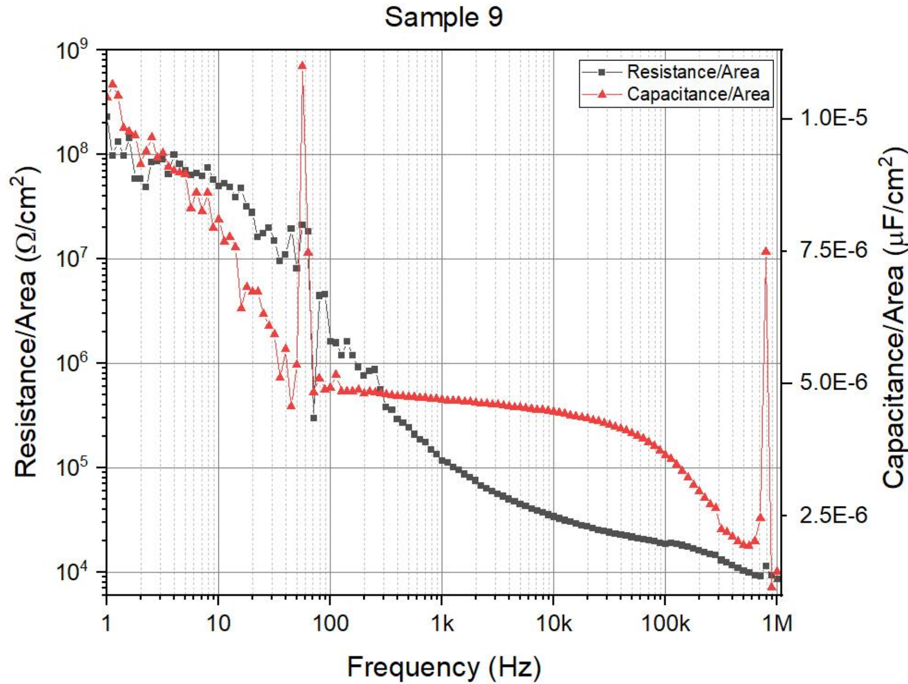

Figure 3.17: Resistance/area ($R_{nASiO_2/Si}$) and capacitance/area ($C_{nASiO_2/Si}$) vs. frequency plots for SiO_2/Si Sample 9

From Figure 3.9- 3.17, we can see that in all cases, $R_{nASiO_2/Si}$ and $C_{nASiO_2/Si}$ decreased with increasing frequency. The rate of decline of $R_{nASiO_2/Si}$ with frequency was not always the same for the SiO_2/Si thin film samples and $R_{nASiO_2/Si}$ vs. frequency curves can be divided into three regions. The first region where $R_{nASiO_2/Si}$ drops steeply ranges from 1Hz to about 300 Hz. This rate slowed down in the second region ranging from 300Hz to about 70kHz, then again fell down faster in somewhat about 70kHz to 1MHz range. Although, $R_{nASiO_2/Si}$ vs. frequency curves of all samples showed these three regions, however, the rate of decrease and the range limit of frequency in the mentioned three regions of the $R_{nASiO_2/Si}$ vs. frequency curve varies from sample to sample. From the $C_{nASiO_2/Si}$ vs. frequency plots of the thin film samples, it was observed that at higher frequency (>7kHz), the decrease rate of $C_{nASiO_2/Si}$ with frequency was less than that at lower

frequencies. Also, similar to $R_{nASiO_2/Si}$vs. frequency curves, the decline rate of $C_{nASiO_2/Si}$with frequency varied in each sample.

For SiO_2/Si thin films Data at 50 kHz was used to analyze Taguchi DOE. In this region, as shown in Figure 3.9- 3.17, the data is more trending with lesser outliers. S/N graphs for electrical properties of the SiO_2/Si thin film samples are shown in Figure 3.18 & 3.19 and the ANOVA results for resistance/area (R_{nA}) and capacitance/area (C_{nA}) are tabulated in Table 3.6 and 3.7, respectively. Taguchi analysis for 10kHz was also performed Figure 3.20 & 3.21, which showed almost similar results as Figure 3.18 & 3.19, but the ANOVA analysis for resistance/area (R_{nA}) resulted in P-value>0.05 (sputtering power had the smallest P-value=0.157) for each of the parameters (Table 3.8).

In order to explain the S/N graph in Figure 3.18 & 3.19, we first look at what changes the electrical properties SiO_2/Si thin films. Here two factors are influencing R_{nA} and C_{nA}. The first one is the layer thickness d_n and the other is the number of nucleation sites on the substrate surface and nucleation growth, or, in different words, the amount of micro-voids and pores present in the thin film structures. Note that the substrate thickness d_{Si} is constant. The layer thickness d_n of the thin films is a function of process parameters, so SiO_2 layer thicknesses vary from sample to sample. Increasing the sputtering power creates more nucleation sites on the surface of the substrate [56]. Because of the high kinetic energy of the falling target atoms at higher power, more atoms can reach the surface initially and act as nucleation sites. The deposition rate increases with sputtering power as well [12]. The resistance of the thin film is directly proportional and the capacitance is inversely proportional to the layer thickness d_n. When the sputtering power begins to rise, increased nucleation sites on the substrate surface and higher nucleation growth start to fill up the micro-voids and cavities in the layer structure faster than the deposition rate.

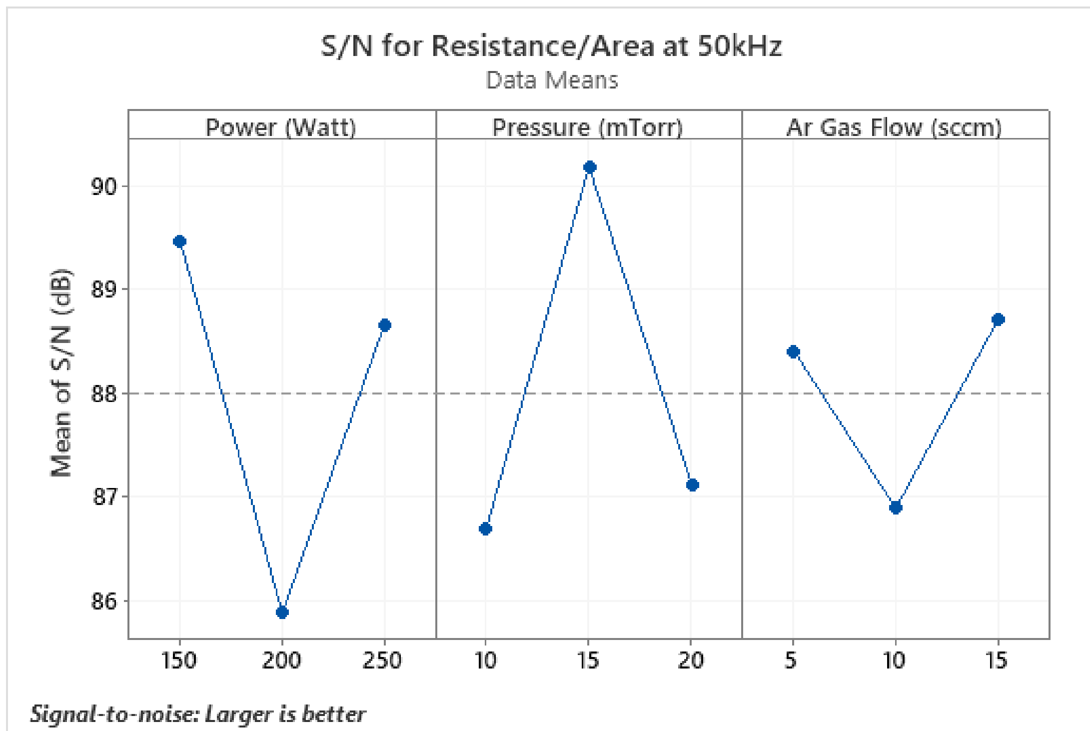

Figure 3.18: S/N graph for the resistance/area ($R_{nASiO_2/Si}$) of SiO_2/Si thin films at 50kHz

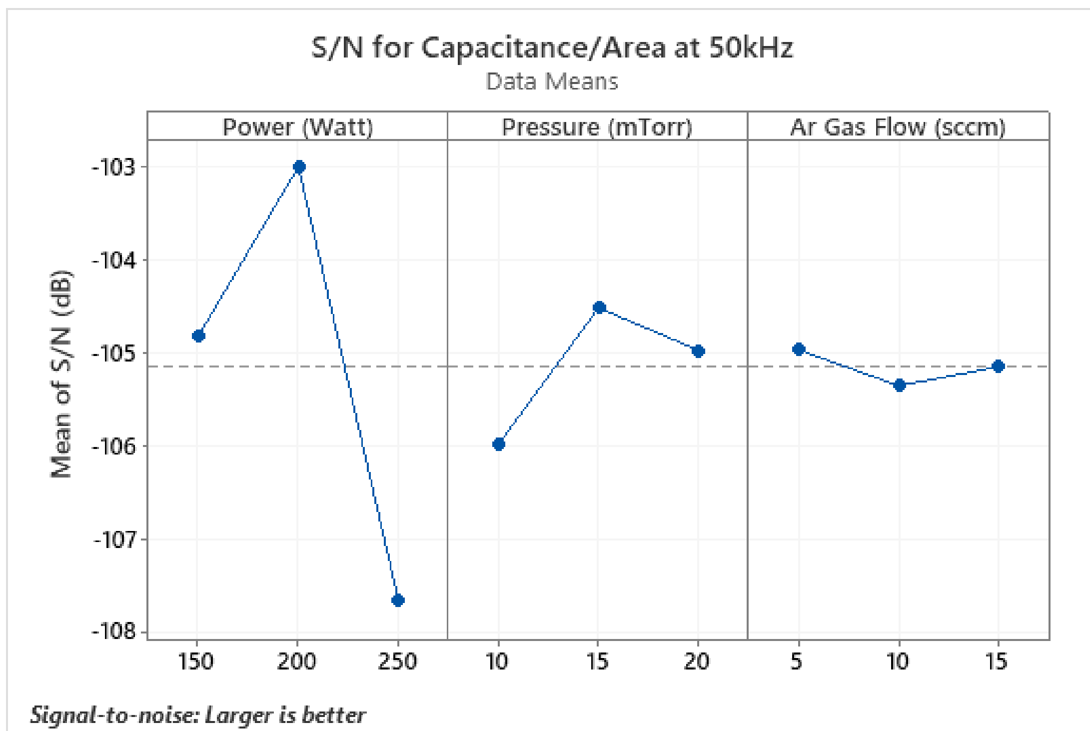

Figure 3.19: S/N graph for the capacitance/area ($C_{nASiO_2/Si}$) of SiO_2/Si thin films at 50kHz

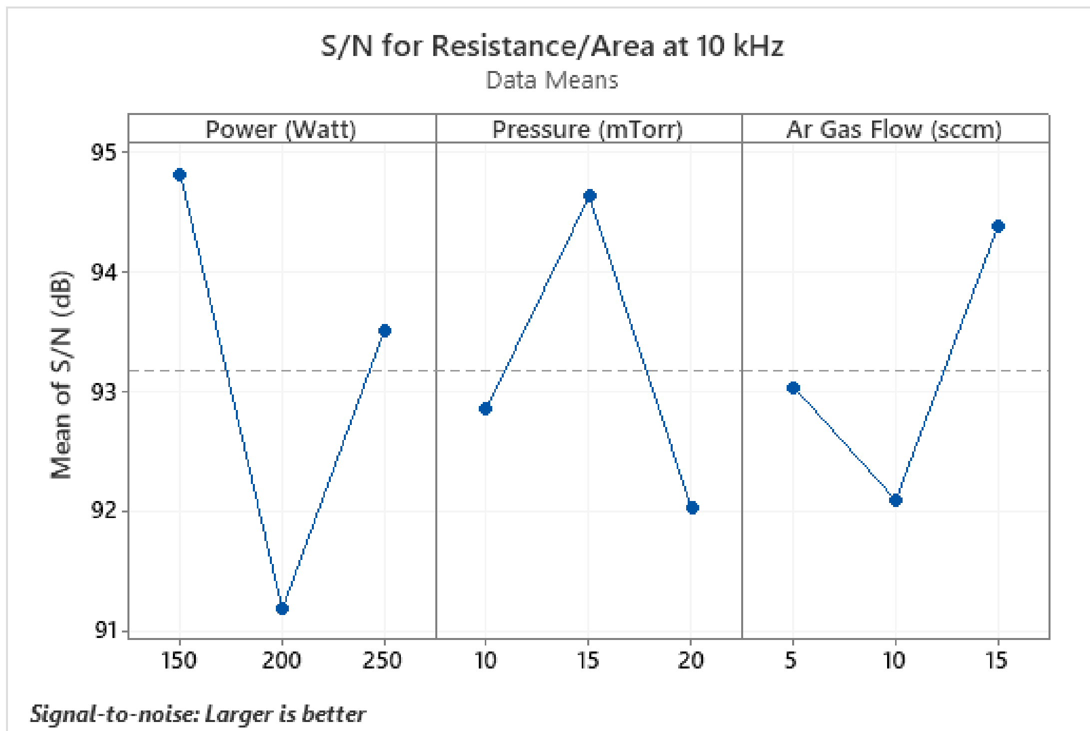

Figure 3.20: S/N graph for the resistance/area ($R_{nASiO_2/Si}$) of SiO_2/Si thin films at 10kHz

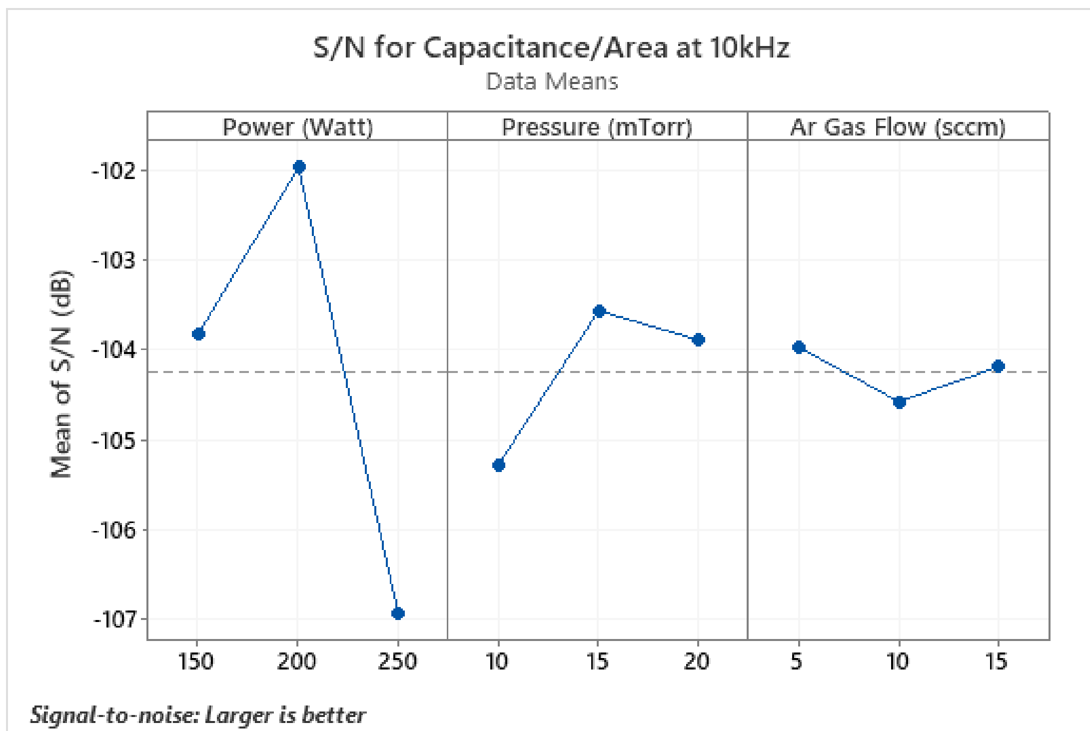

Figure 3.21: S/N graph for the capacitance/area ($C_{nASiO_2/Si}$) of SiO_2/Si thin films at 10kHz

Table 3.6: Summary of ANOVA result for resistance/area ($R_{nASiO_2/Si}$) at 50 kHz frequency for SiO_2/Si thin films

Source	DF	Seq SS	Contribution	Adj SS	Adj MS	F-Value	P-Value
Power (Watt)	2	1.48E+8	40.40%	1.48E+8	7.44E+7	47.60	0.021
Pressure (mTorr)	2	1.90E+8	51.71%	1.90E+8	9.52E+7	60.93	0.016
Ar Gas Flow (sccm)	2	2.59E+7	7.04%	2.59E+7	1.30+7	8.30	0.108
Error	2	3.13E+6	0.85%	3.13E+6	1.56E+7		
Total	8	3.68E+8	100.00%				

Table 3.7: Summary of ANOVA result for resistance/area ($C_{nASiO_2/Si}$) at 50 kHz frequency for SiO_2/Si thin films

Source	DF	Seq SS	Contribution	Adj SS	Adj MS	F-Value	P-Value
Power (Watt)	2	0.000000	89.79%	0.000000	0.000000	155.01	0.006
Pressure (mTorr)	2	0.000000	8.81%	0.000000	0.000000	15.21	0.062
Ar Gas Flow (sccm)	2	0.000000	0.82%	0.000000	0.000000	1.41	0.415
Error	2	0.000000	0.58%	0.000000	0.000000		
Total	8	0.000000	100.00%				

Table 3.8: Summary of ANOVA result for resistance/area ($R_{nASiO_2/Si}$) at 10 kHz frequency for SiO_2/Si thin films

Source	DF	Seq SS	Contribution	Adj SS	Adj MS	F-Value	P-Value
Power (Watt)	2	5.32E+8	49.83%	5.32E+8	2.66E+7	5.39	0.157
Pressure (mTorr)	2	2.71E+8	25.38%	2.71E+8	1.36E+7	2.74	0.267
Ar Gas Flow (sccm)	2	1.66E+7	15.54%	1.66E+7	8.30+7	1.68	0.373
Error	2	9.88E+6	9.25%	9.88E+6	4.94E+7		
Total	8	1.07E+9	100.00%				

Table 3.9: Summary of ANOVA result for resistance/area ($C_{nASiO_2/Si}$) at 10 kHz frequency for SiO_2/Si thin films

Source	DF	Seq SS	Contribution	Adj SS	Adj MS	F-Value	P-Value
Power (Watt)	2	0.000000	86.32%	0.000000	0.000000	1388.07	0.001
Pressure (mTorr)	2	0.000000	11.60%	0.000000	0.000000	186.59	0.005
Ar Gas Flow (sccm)	2	0.000000	2.02%	0.000000	0.000000	32.41	0.030
Error	2	0.000000	0.06%	0.000000	0.000000		
Total	8	0.000000	100.00%				

In this period, the resistance of the deposited layer decreases and capacitance increases. However, increasing power only boosts the deposition rate after a certain power range, as the number of nucleation sites on the surface strats to saturate. So, this event forces the resistance to go up and capacitance to go down as the growing layer thickness is the dominating factor now. This is why S/N for $R_{nASiO_2/Si}$ decreased and S/N for $C_{nASiO_2/Si}$ increased first. After 200W, escalating power reduced $C_{nASiO_2/Si}$but $R_{nASiO_2/Si}$ improved. The effect of pressure on the $R_{nASiO_2/Si}$ of the thin films should be the opposite. Because of the shrunk mean free path, increased inter-atomic collisions between target and process gas atoms at higher pressure impede the target atom from reaching the substrate surface and acting as nucleation sites. Consequently, nucleation growth slows down, deposited layers become less dense with full of voids and gaps and produce highly resistive films. A lower deposition rate at high pressure also leads to thinner films. As a result, rising the pressure from 10mTorr to 15 mTorr improved both $R_{nASiO_2/Si}$ and $C_{nASiO_2/Si}$ However, from the pressure range 15mTorr to 20mTorr, $R_{nASiO_2/Si}$ and $C_{nASiO_2/Si}$ both degrade. In this pressure range, reducing film thicknesses affecting $R_{nASiO_2/Si}$ more and the influecne of excessive micro-voids in the layer structure on the relative permittivity overcomes the impact of the shortening film thickness d_n on the capacitance of the film, which in consequence, decreases $C_{nASiO_2/Si}$.

The ANOVA analysis in Table 3.6 reveals working pressure has the highest contribution on $R_{nASiO_2/Si}$ (51.71%). Power has slightly less contribution 40.40%. Both of the contributions are significant. For $C_{nASiO_2/Si}$ (Table 3.7), power is the dominant factor (contribution 89.79%) in contrast to pressure contribution (8.81%). The contribution of Ar gas flow rate can be ignored as it is not very significant (7.04% for $R_{nASiO_2/Si}$ and 0.82% for $C_{nASiO_2/Si}$ and in both cases P-value > 0.05). The non-linear behavior of the S/N graphs for the electrical properties of the SiO_2/Si thin

films is the reason why no regression model could not be derived for resistance/area ($R_{nASiO_2/Si}$) and capacitance/area ($C_{nASiO_2/Si}$).

3.5 Adhesion

The adhesion of the SiO_2/Si thin films was examined by scotch tape test. All nine samples passed the adhesion test. They remain adhered to the substrate even after pulling off the tape.

3.6 Conclusion

SiO_2 thin film samples were deposited over Si substrate by radio frequency (RF) magnetron sputtering system. Taguchi DOE and ANOVA analysis were performed to understand the effect of three process parameters-power, pressure and Ar gas flow rate and their individual contribution on surface, morphological and electrical properties of the SiO_2/Si thin films. It was determined that power and pressure are the dominant factors that influence the significant percentage of the properties in most cases. Ar gas flow rate has little effect on the properties of the sputtered SiO_2/Si thin films.

CHAPTER IV

CHARACTERIZTION OF pSi/Si THIN FILMS

The following experiments of characterization of nine samples SiO_2/Si thin films were conducted in this research.

- ✓ Surface Roughness
- ✓ Structural properties from XRD analysis- crystallinity, micro-strain and dislocation density.
- ✓ Electrical properties (resistance per unit area ($R_{nApSi/Si}$) and capacitance per unit area ($C_{nApSi/Si}$).

In this chapter the results and discussions of these experiments are presented.

4.1 Surface Roughness of pSi/Si Thin Films

The surface roughness of nine pSi/Si thin films is given in Table 4.1. S/N response of surface roughness of deposited pSi films is shown in Figure 4.1 and the result of the ANOVA analysis is shown is Table 4.2. The result of the surface roughness of pSi/Si is almost similar to the result of SiO_2/Si thin films. With the rise of sputtering power, atomic peening effect [12, 54] as described previously, fill up most of the voids and pores on the surface. Highly condensed layer with smooth surface is produced as the outcome. Contrastively, when the working pressure is rising, the loss of kinetic energy of the falling target atoms due to the collisions with the

pressurized process gas atoms construct a loosely packed layer with pores and voids, which in result, increases the roughness of the deposited surface. Similar observation on the surface roughness of the deposited films has been described in [40].

Table 4.1: Summary of surface roughness (R_a) of pSi/Si thin films

Sample No.	Roughness R_a (nm)
pSi Sample 1	21.2
pSi Sample 2	22.0
pSi Sample 3	22.6
pSi Sample 4	18.8
pSi Sample 5	19.3
pSi Sample 6	20.1
pSi Sample 7	14.0
pSi Sample 8	15.6
pSi Sample 9	16.3

It was seen that the power contribution to surface roughness is greater 93.56% comparing to the working pressure (5.85%). With the increase of the process gas flow rate, roughness of the surface improves. The impact is not described rigorously in previous works, only mentioned in [55]. Coarse grains at the surface deposited at low flow rate increases the roughness, according to [55]. However, the significance of effect is ignorable (contribution 0.38%).

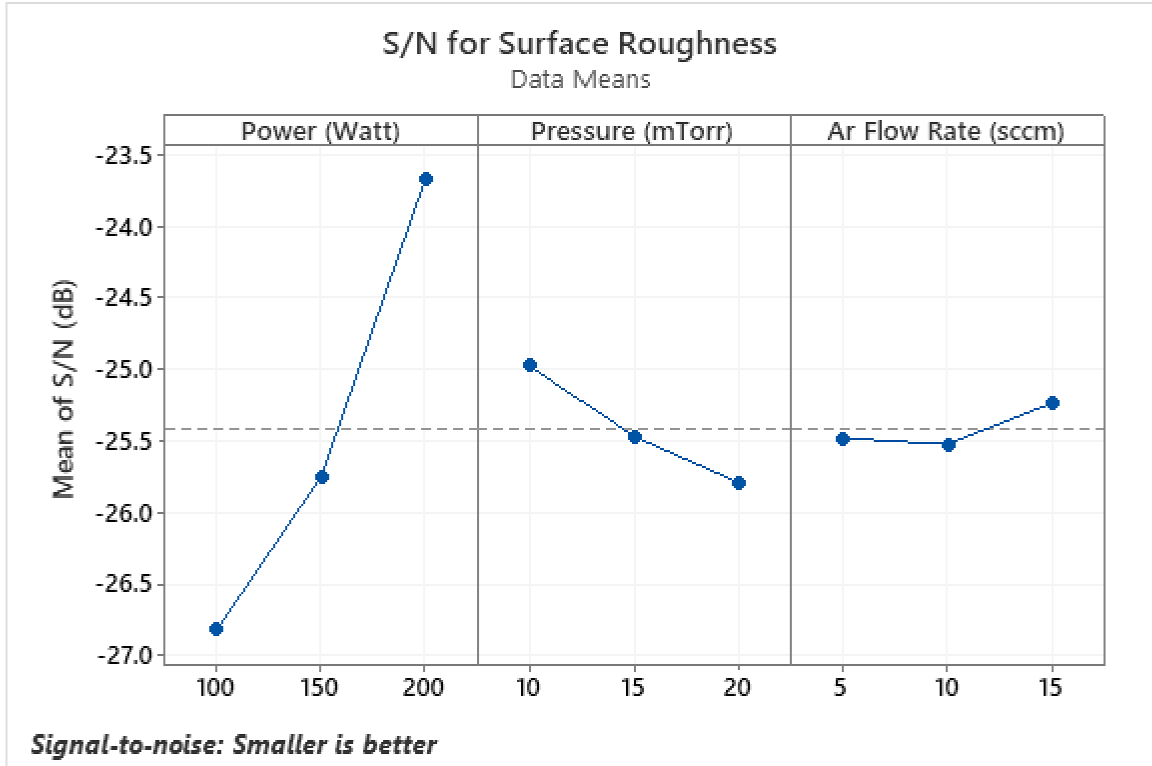

Figure 4.1: S/N response graph for surface roughness of pSi/Si thin film.

Table 4.2: Summary of ANOVA result for surface roughness (R_a) of pSi/Si thin films

Source	DF	Seq SS	Contribution	Adj SS	Adj MS	F-Value	P-Value
Power (Watt)	2	67.2289	93.56%	67.2289	33.6144	451.54	0.002
Pressure (mTorr)	2	4.2022	5.85%	4.2022	2.1011	28.22	0.034
Ar Gas Flow (sccm)	2	0.2756	0.38%	0.2756	0.1378	1.85	0.351
Error	2	0.1489	0.21%	0.1489	0.0744		
Total	8	71.8556	100.00%				

A regression analysis was also performed with the surface roughness data and its performance is given in Table 4.3.

$$\text{Roughness } (R_a) \text{ (nm)} = \begin{array}{c} 26.66 - 0.06633 \text{ Power (Watt)} + 0.1667 \text{ Pressure (mTorr)} \\ - 0.0333 \text{ Ar Flow Rate (sccm)} \end{array} \quad 4.1$$

Table 4.3: Summary of the regression analysis of surface roughness of pSi/Si thin films

S	R-sq	R-sq(adj)	R-sq(pred)
0.551463	97.88%	96.61%	92.60%

4.2 XRD Analysis of pSi/Si Thin Films

According to RRUFF database (Si, RRUFF ID: R050145, [57]) and literature, XRD pattern of the following planes of Si has been identified- Si [1 1 1] at $2\theta \sim 28.44^o$ [37], Si [2 0 0] at $2\theta \sim 33^o$ [58], Si [2 2 0] at $2\theta \sim 47.3^o$ [37], Si [3 2 1] at $2\theta \sim 51^o$ [37], Si [3 1 1] at $2\theta \sim 56.28^o$ [37] Si [2 2 2] reflection about $2\theta \sim 58.9^o$ [58] and Si [1 0 0] or Si [4 0 0] at $2\theta \sim 69.1^o$ [59]. The substrate used in this experiment was intrinsic Si with [1 0 0] miller index. The XRD pattern of the substrate is shown Figure 4.2. The Cu-Kα peak was achieved at $2\theta = 68.5^o$ with intensity (cps) about over 100k, which means the substrate was highly crystallized. There was also a secondary peak at $2\theta = 61^o$, which is attributed to Cu-Kβ X-ray. The intensity of this peak was about 3000 cps, which is far less than the primary peak at $2\theta = 68.5^o$. The XRD pattern of the nine pSi/Si thin films is shown in Figure 4.3. All the peaks were achieved at about $2\theta = 68.2^o$ - 69°. These peaks means that the deposited pSi grew along [1 0 0] plane. Similar XRD peak of the deposited pSi is described in [57, 59]. However, the intensity of these peaks were far less that the substrate peak at $2\theta = 68.5^o$.

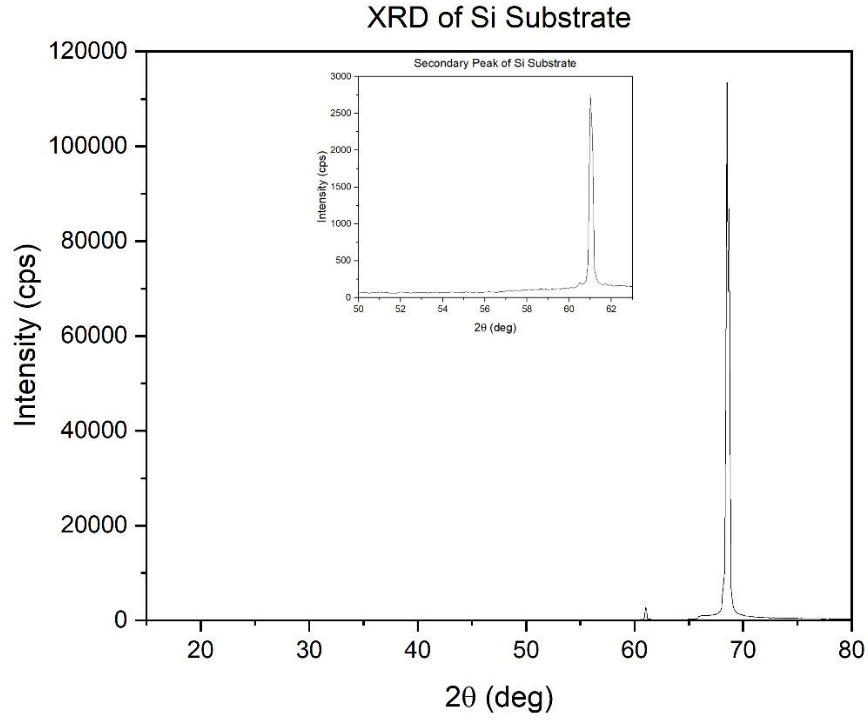

Figure 4.2: XRD pattern of the Si [1 0 0] substrate.

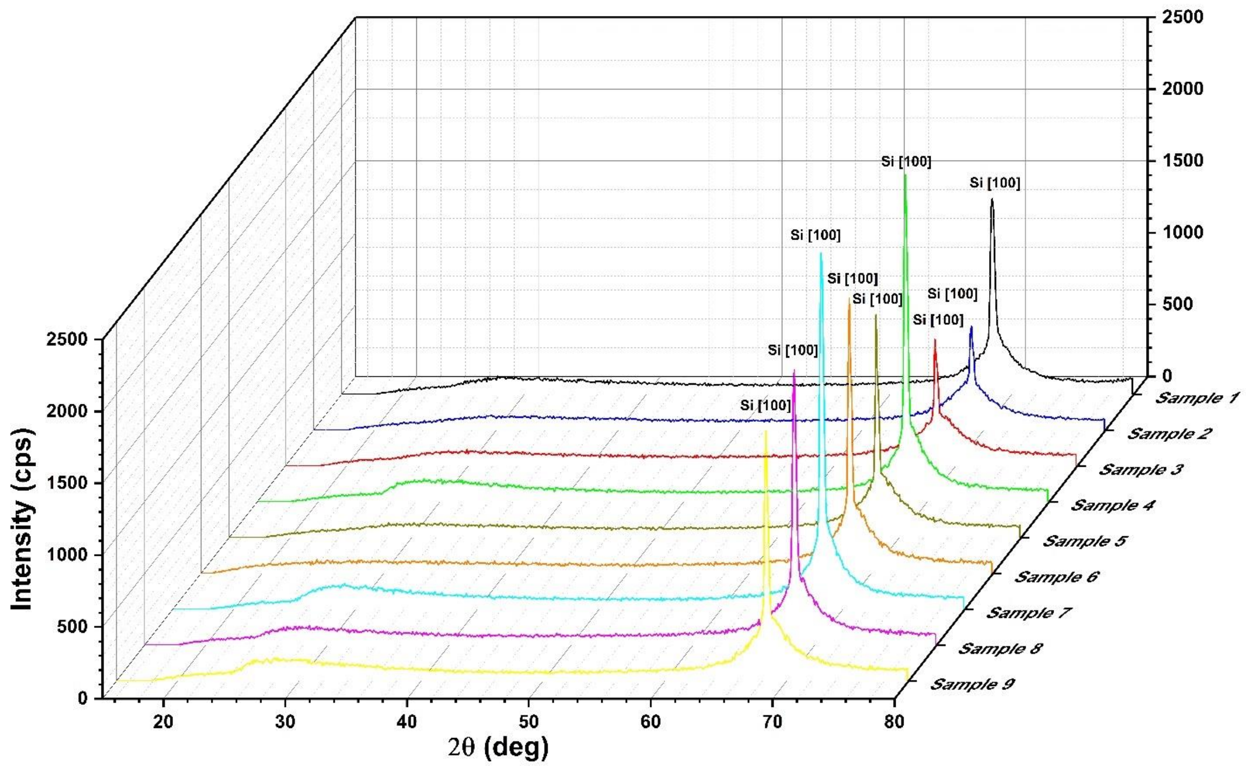

Figure 4.3: XRD pattern of 9 pSi/Si thin film samples

The highest peak was achieved from sample 7 (intensity 2480.67). This fall from intensity was expected, as the sputtered thin films would not have the high crystallinity as the substrate. Also, no secondary peak at $2\theta = 61^o$ was seen in any samples. The summary of the XRD analysis is tabulated in Table 4.4. From the XRD analysis several structural properties-crystallinity, grain size, micro-strain and dislocation density can be studied. Table 4.4 contains grain size, micro-strain and dislocation density of the nine pSi/Si thin film samples.

Table 4.4: Summary of the XRD analysis of pSi/Si thin films

Sample No.	Peak Position 2θ (deg)	Peak Intensity (cps)	FWHM β (deg)	Grain Size D (nm)	Micro-strain $\boldsymbol{\varepsilon}$ ($\times 10^{-3}$)	Dislocation Density δ (nm^{-2})
pSi Sample 1	68.4	1362.33	0.64767	14.83	4.15	4.54
pSi Sample 2	69	722.667	1.24677	7.73	7.92	16.7
pSi Sample 3	68.3	883.333	0.81522	11.78	5.23	7.20
pSi Sample 4	68.2	2278.33	0.58207	16.49	3.75	3.68
pSi Sample 5	68.1	1553	0.6365	15.07	4.10	4.40
pSi Sample 6	68.2	1914.5	0.60843	15.77	3.92	4.02
pSi Sample 7	68.2	2480.67	0.60259	15.93	3.88	3.94
pSi Sample 8	68.3	1914	0.59788	16.06	3.84	3.88
pSi Sample 9	68.3	1743	0.59444	16.15	3.82	3.83
Substrate	68.5	113593				
	61	2762.33				

4.2.1 Crystallinity

The peak of the XRD pattern signifies the crystallinity of the thin film. The peak positions or the Brags' angle of nine pSi/Si sample and their associated peaks are listed in Table 4.4. The S/N ratio of the XRD peaks or the crystallinity of the pSi/Si thin film samples is shown in Figure 4.4 and Table 4.5 shows the summary of the ANOVA analysis.

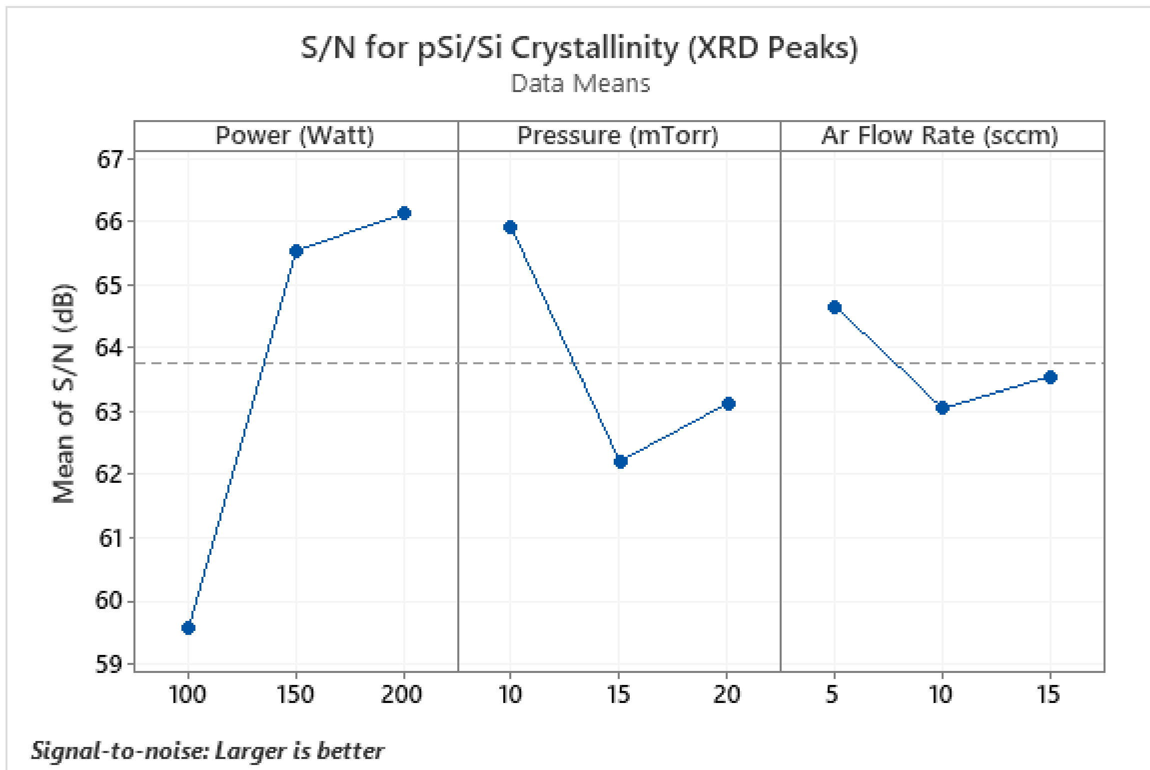

Figure 4.4: S/N response graph for Crystallinity of the pSi/Si thin films.

From Figure 4.4 it can be seen that the XRD peak of the pSi/Si thin films increaes with rising power, which agrees with [60]. With high power, atomic peening effect- described in [12, 54] creates more nucleation sites, which in turns improves crystallinity and also, the boosted nucleation growth on the surface builds up a thicker layer [60, 61]. However, as the Figure 4.4 suggests, the steep at 150-200 Watt power is lesser than that at 100-150 Watt power. Described

in Section 4.4, when the sputtering power goes over a certain limit, the nucleation sites on the surface start to saturate. So, improvement of the crystallinity does not change much after a certain point. The lesser steep 150-200 Watt crystallinity region supports this explanation.

Table 4.5: Summary of ANOVA result for crystallography (XRD peaks) of pSi/Si thin films.

Source	DF	Seq SS	Contribution	Adj SS	Adj MS	F-Value	P-Value
Power (Watt)	2	1990307	71.77%	1990307	995153	46.28	0.021
Pressure (mTorr)	2	705846	25.45%	705846	352923	16.41	0.057
Ar Gas Flow (sccm)	2	33841	1.22%	33841	16921	0.79	0.560
Error	2	43010	1.55%	43010	21505		
Total	8	2773004	100.00%				

The rising pressure should have the oppisite effect on the crystallinity. As the collisions between target atoms and process gas atoms increases with rising pressure due to the shorter mean free path between gas atoms, the loosely packed porous layer developed over the substrate manifests declining crystallographic quality [61]. When the pressure was risen from 10mTorr to 15mTorr, the XRD peaks decreses, which concurs with the thoery. But as the pressure was further increased from 15mTorr to 20mTorr, XRD peak demonstrated more intensity. To be precise, pSi sample 3 and 6 displayed more intense peaks than sample 2 & 5. Even so, the rate of increase of the XRD intensity from 15 to 20mTorr was not as prominent as the declining rate of intensity from 10 to 15mTorr. From our data, the contribution of the sputtering power to the crystallography is most significant (71.77%). Working pressure has quite a significant

contribution (25.45%) with a p-value just over 0.05 (=0.057). The effect of Ar gas flow rate can not be described from our data because the p-value is far above 0.05 (0.560) and the correnpoding contribution to XRD peak is ignorable (1.22%, less than error- 1.55%).

4.2.2 Grain Size

The grain size of the thin film for XRD analysis can be calculated from the Scherrer equation as follows-

$$D\ (Grain\ Size) = \frac{0.9\ \lambda}{\beta\ cos\theta}$$

Where-

λ = The wavelength of the x-ray, here CuKα- 1.506 A^{o}

β = Full width at half maximum (FWHM)

θ = Bragg's angle

Grain size is directy related to the XRD peaks of the thin film. For more intense and sharp peak, the FWHM β should be less, so grain size would be bigger and vise versa. From the the observation of the data of this experiement, as the power increased, average size of of the grains became larger, as can be seen from Table 4.4. pSi Sample 7-9 set had the largest average grain size. Higher power assures better crystal growth, so size of the crystallite improves. But when the power jumped from 150W (pSi sample 4-6) to 200W (pSi sample 7-9) there was a slight increase in grain size comparing to the increase of grain size when power jumped from 100W (pSi sample 1-3) to 150W (pSi sample 4-6). This is because of the saturation of the necleation sites at higher power level. As the number nucleation sites does not increase much at very high power, the sizes of the grain also become almost constant at this condition. At lower power levels (100W and 150W), with the variation of pressure, change of grain size was also noticable. As the pressure

rose from 10mTorr to 15mTorr, grain size decreased significantly. In constrast to that, jumping from 15mTorr to 20mTorr presssure grain size increased.

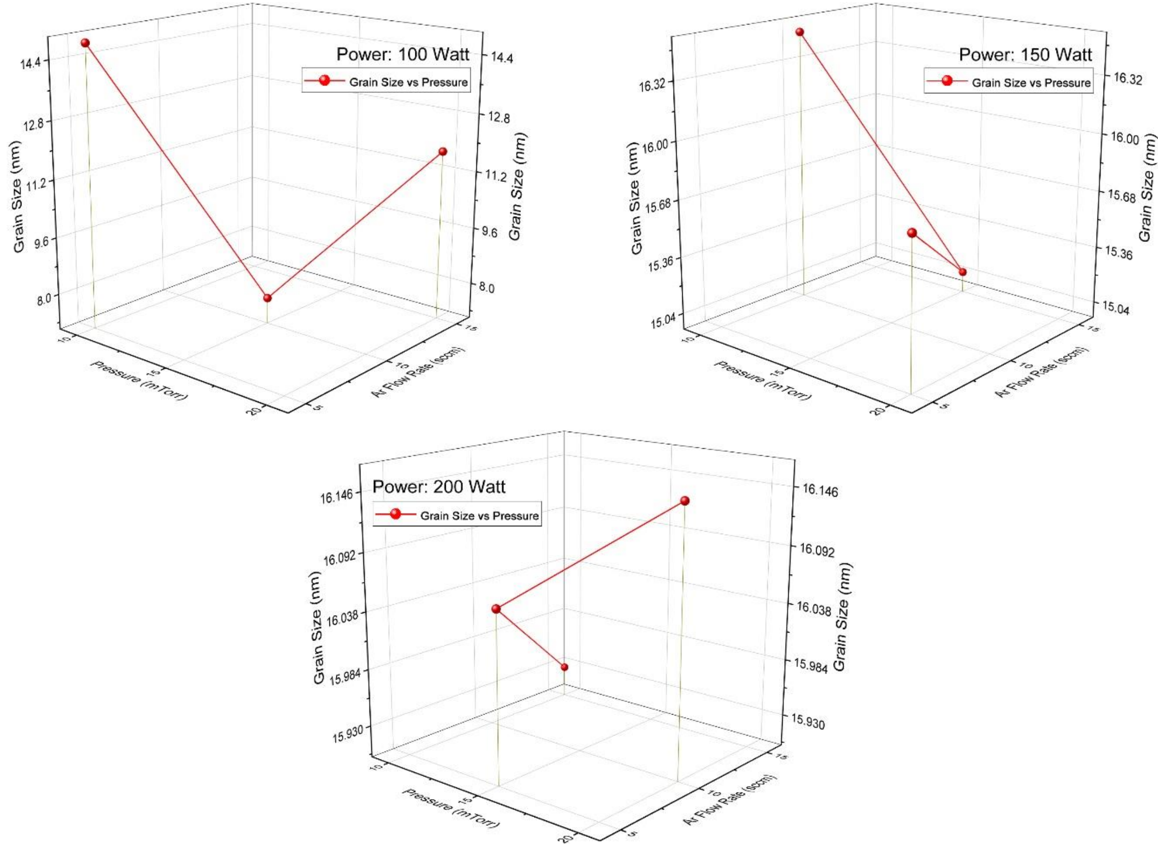

Figure 4.5: Grain size of the pSi/Si thin films. Power is constant in each graph- 100W (top-left), 150W (top-right) and 200W (bottom). The line in each graph shows the variation with pressure.

At high power level (200W), due the saturation of nucleation sites on the surface, the grain size does not vary much with the change of pressure (pSi sample 7 had 15.93nm, pSi sample 9 had 16.15nm). Figure 4.5 show the variation of grain size at each power level with the change of pressurre and Ar Gas flow rate. The connecting line shows the variation of grain size with variation of pressure at constant power.

4.2.3 Micro-strain

The formula to determine micro-strain from XRD analysis is as following:

$$\varepsilon\ (Microstrain) = \frac{\beta}{4\ tan\theta}$$

Where-

β = Full width at half maximum (FWHM)

θ = Bragg's angle

The micro-strain of nine pSi thin films is listed in Table 4.4. Figure 4.6 shows the variation of micro-strain with pressure and Ar gas flow rate at each power level. The connecting line depicts the change in micro-strain when pressure changes.

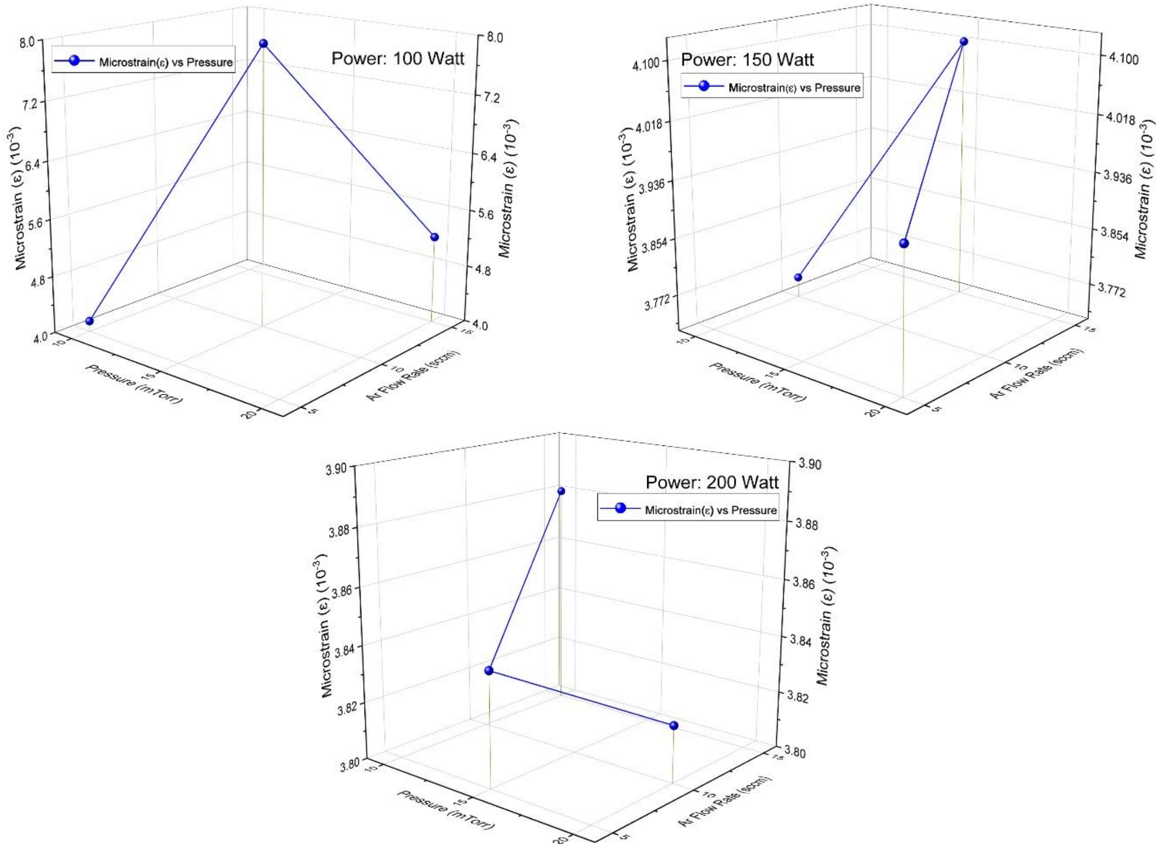

Figure 4.6: Mirco-strain of the pSi/Si thin films. Power is constant in each graph- 100W (top-left), 150W (top-right) and 200W (bottom). The line shows the variation with pressure.

Similar to the grain size, micro-strain in pSi thin films deposited at lower power levels (100W & 150W) showed a drastic variation with the change of pressure. At high power level this change had a little effect on the micro-strain.

4.2.4 Dislocation Density

Dislocation density of the thin film can be measured using following equation:

$$\delta\ (Dislocation\ density) = \frac{n}{D^2}$$

Where-

n = A factor, almost equal to unity for minimum dislocation density

D = Grain size

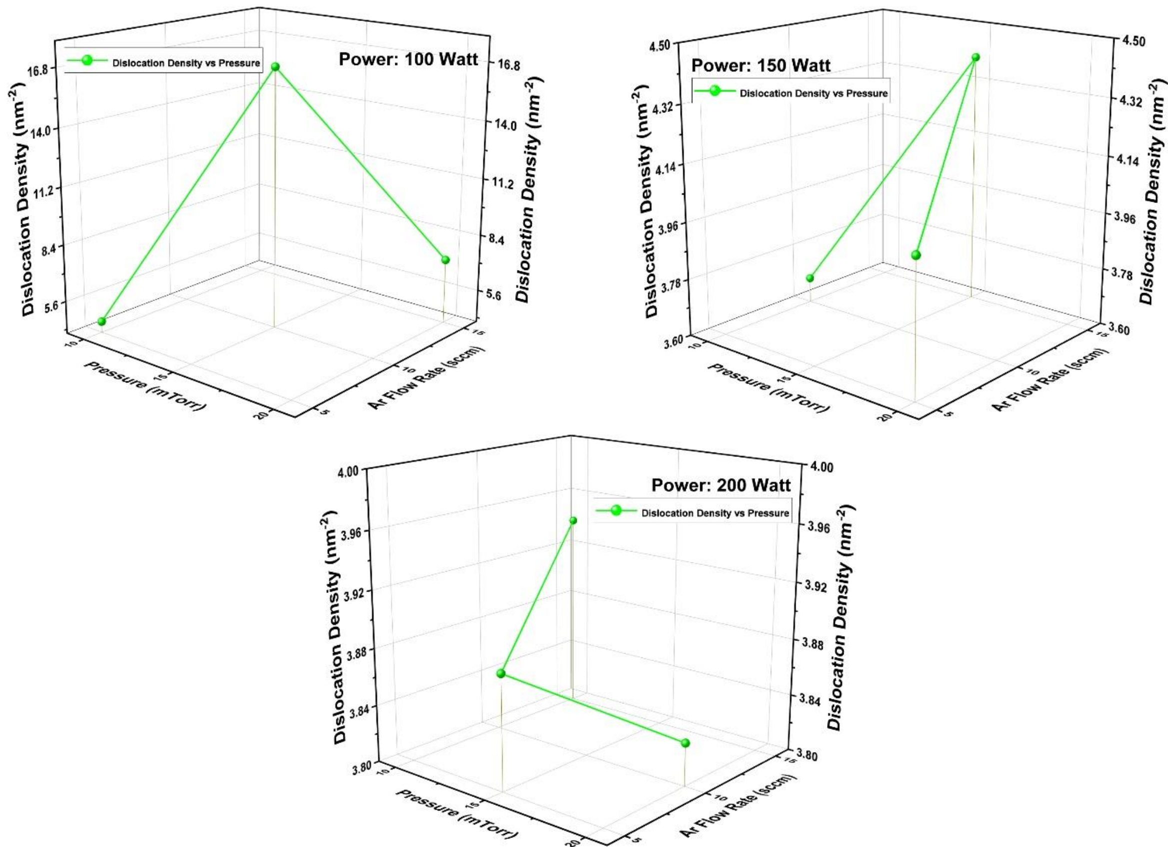

Figure 4.7: Dislocation density of the pSi/Si thin films. Power is constant in each graph- 100W (top-left), 150W (top-right) and 200W (bottom). The line shows the variation with pressure.

Dislocation density of the nine pSi thin films tabulated in Table 4.4 shows similar trends as grain size and micro-strain, that is lower power level (100W and 150W) showed noticeable variation in dislocation density with respect to pressure, whereas at high power level (200W) this change was not very notable.

4.3 Electrical Properties of pSi/Si Thin Films

Thoroughly described section 4.4 (Electrical properties of SiO_2/Si Thin Films- page 33,34), similar technique was used in measurement of the electrical properties of pSi/Si thin films- resistance per unit area $R_{nApSi/Si}$, and capacitance per unit area $C_{nspSi/Si}$. Figure 4.8-4.10 show the impedance spectroscopy results of pSi/Si thin films. Figure 4.11-4.19 show the resistance per unit area $R_{nApSi/Si}$, and capacitance per unit area $C_{nspSi/Si}$ of pSi/Si thin films. It is mentioned before that normalizing with sample area (A_n) was intentionally carried out to omit the area difference effect on the electrical properties.

Similar to the resistance per unit area $R_{nASiO_2/Si}$ and capacitance per unit area $C_{nASiO_2/Si}$ of the SiO_2/Si thin films, resistance per unit area $R_{nApSi/Si}$ and capacitance per unit area $C_{nspSi/Si}$ vs frequency curve of pSi/Si thin films can also be divided into three parts. At low frequency (>1kHz) the declining rate of $R_{nApSi/Si}$ and $C_{nApSi/Si}$ is very steep. At medium frequency range (<1kHz & >100kHz) this rate slows down a bit and at high frequency (>100kHz) the negative slope become steeper again. Table 4.6 shows the $R_{nApSi/Si}$ & $C_{nApSi/Si}$ at 25kHz and 50kHz. Those data were used for S/N analysis and analysis of variance (ANOVA).

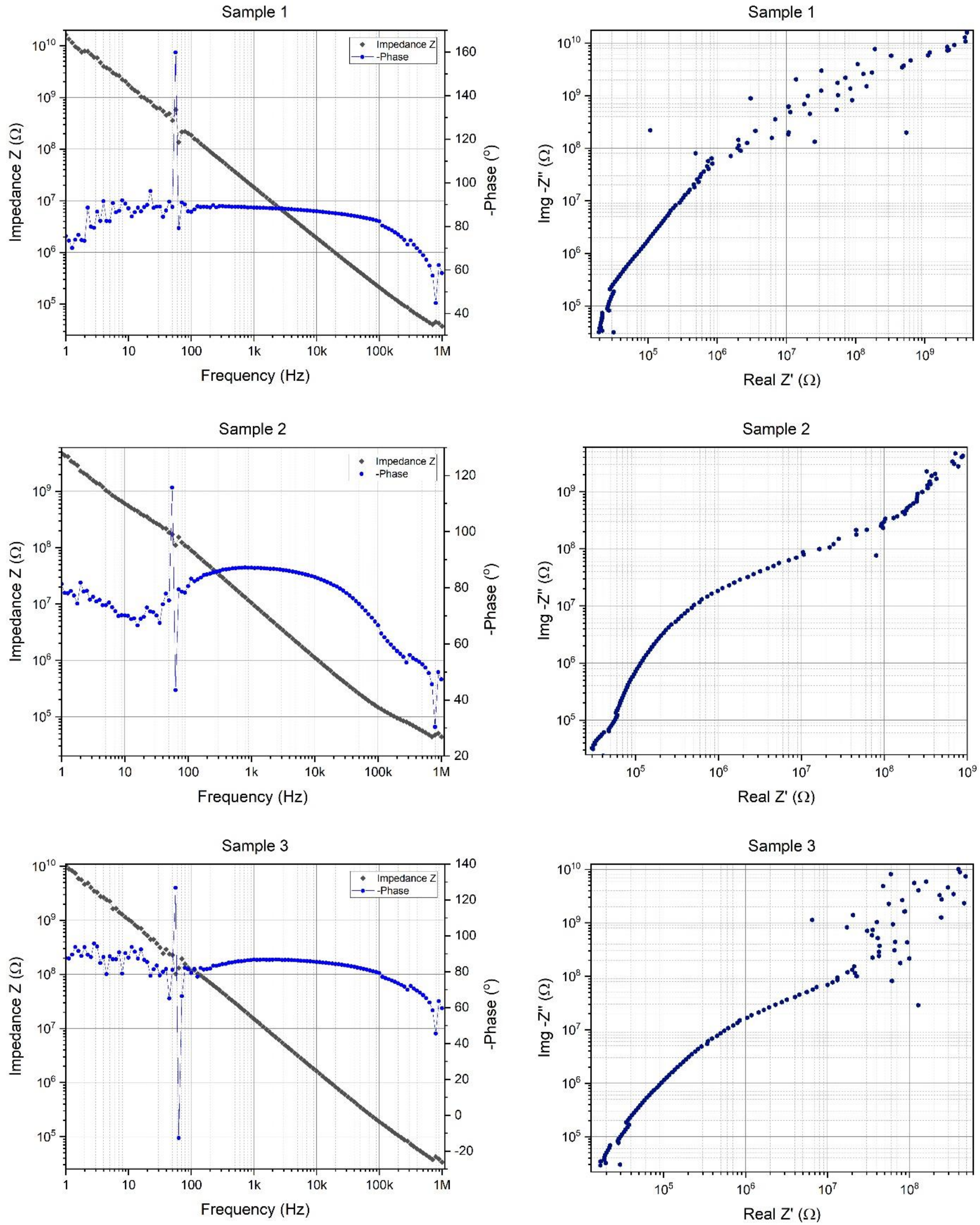

Figure 4.8: Bode plots (right) and Real Z' vs Img Z'' scatter plot (left) for pSi/Si thin film sample

1-3

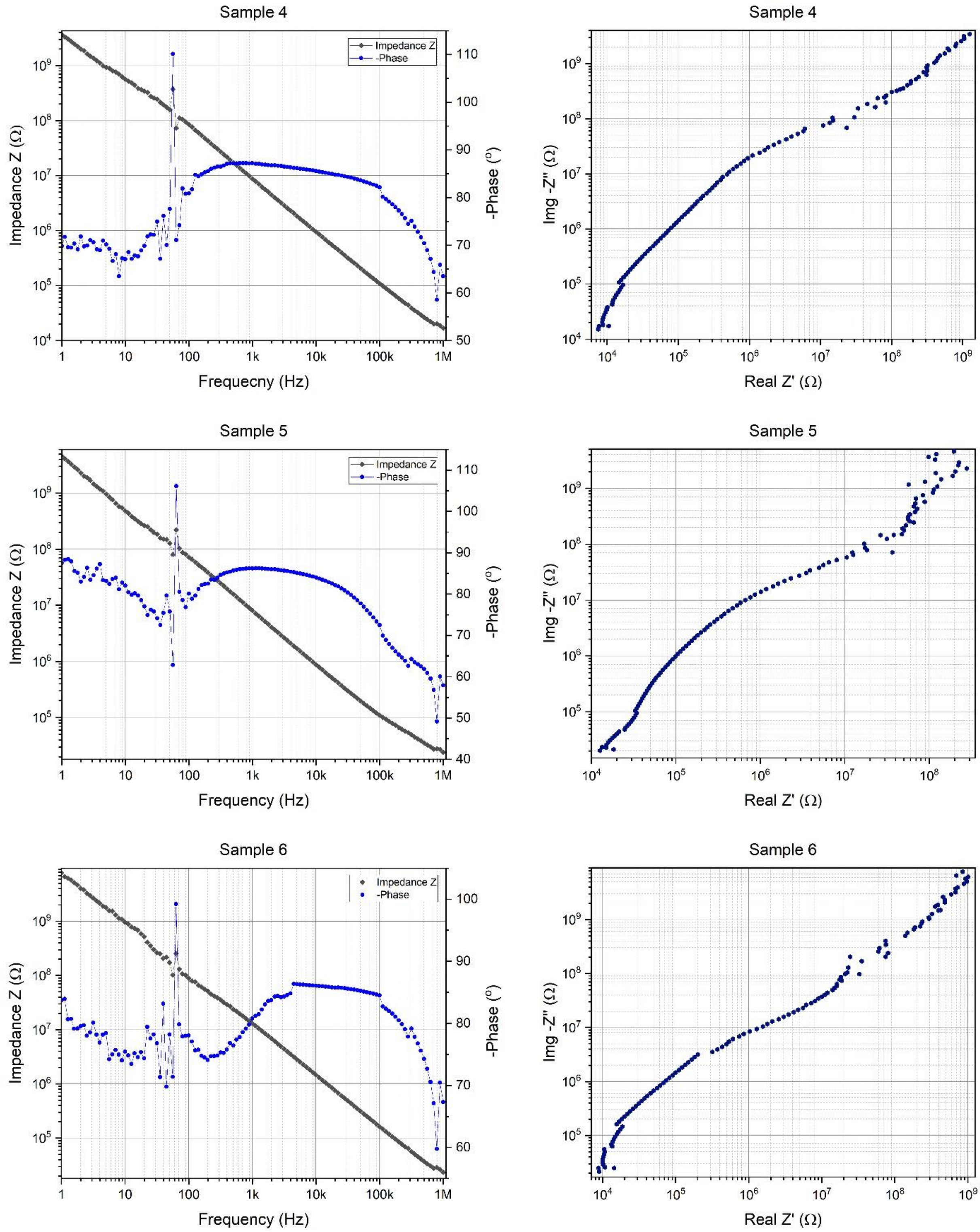

Figure 4.9: Bode plots (right) and Real Z' vs Img Z'' scatter plot (left) for pSi/Si thin film sample 4-6

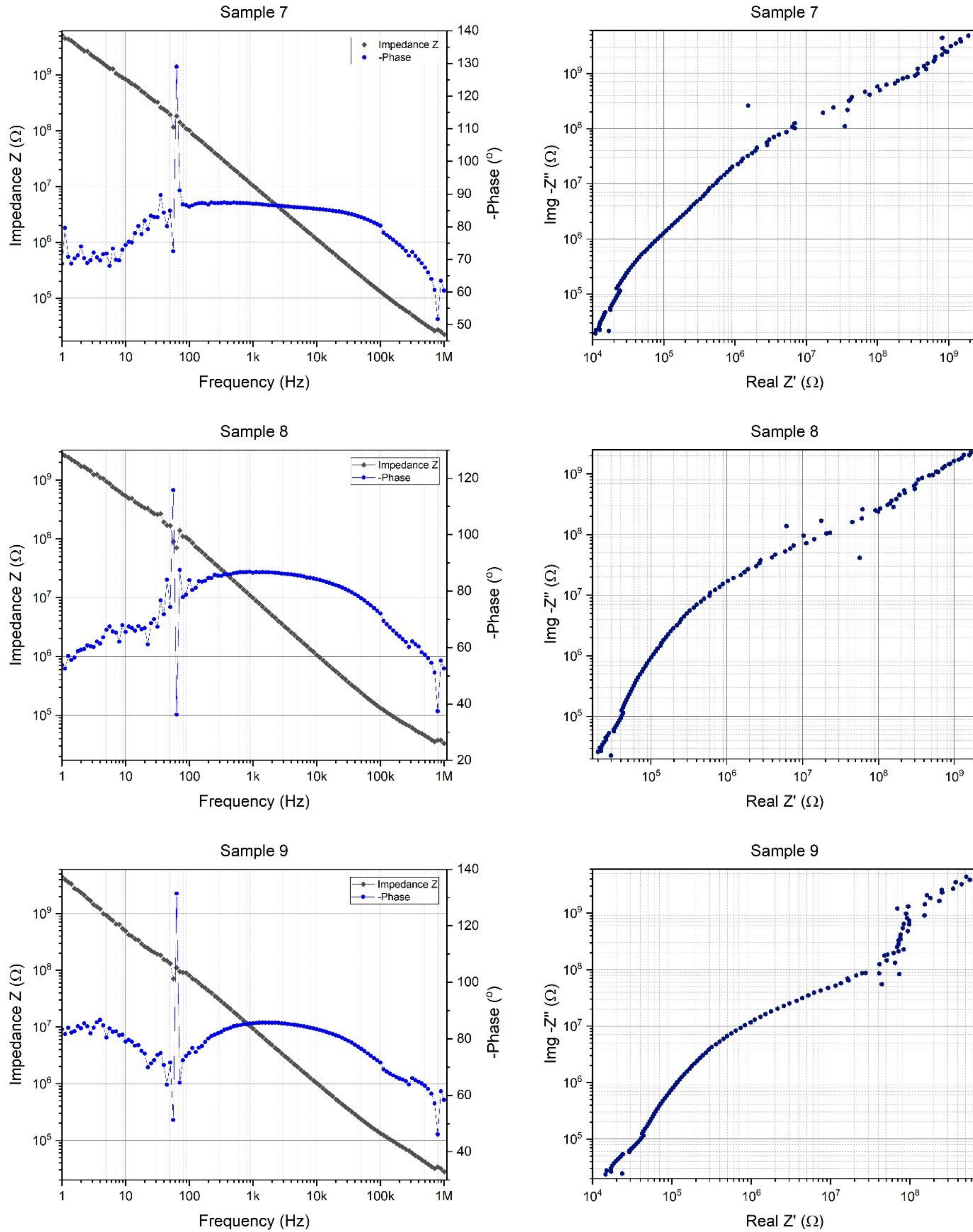

Figure 4.10: Bode plots (right) and Real Z' vs Img Z'' scatter plot (left) for pSi/Si thin film sample 7-9

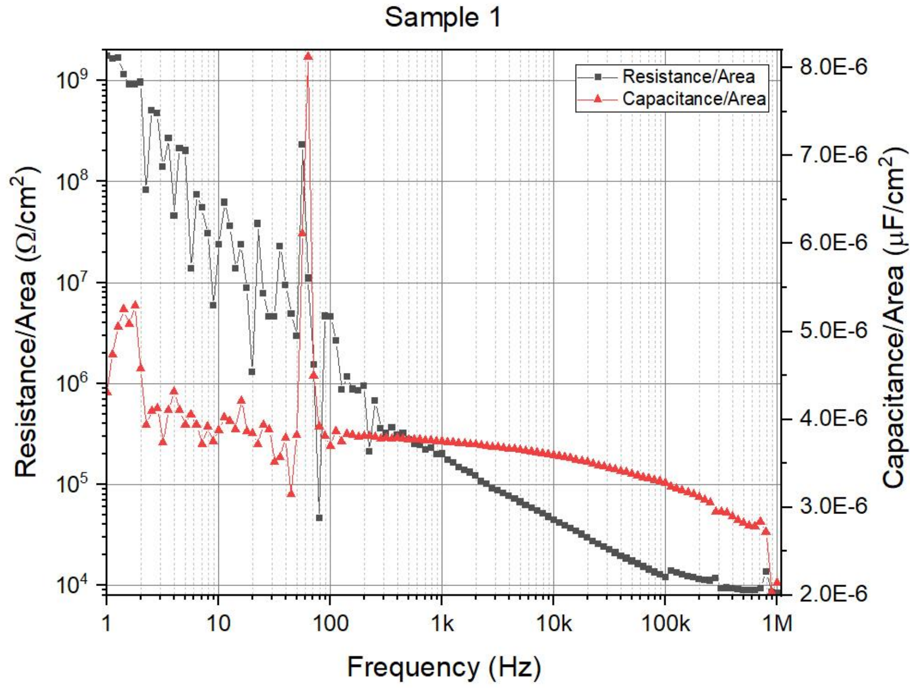

Figure 4.11: Resistance/area ($R_{nApSi/Si}$) and capacitance/area ($C_{nApSi/Si}$) vs. frequency plots for pSi/Si Sample 1

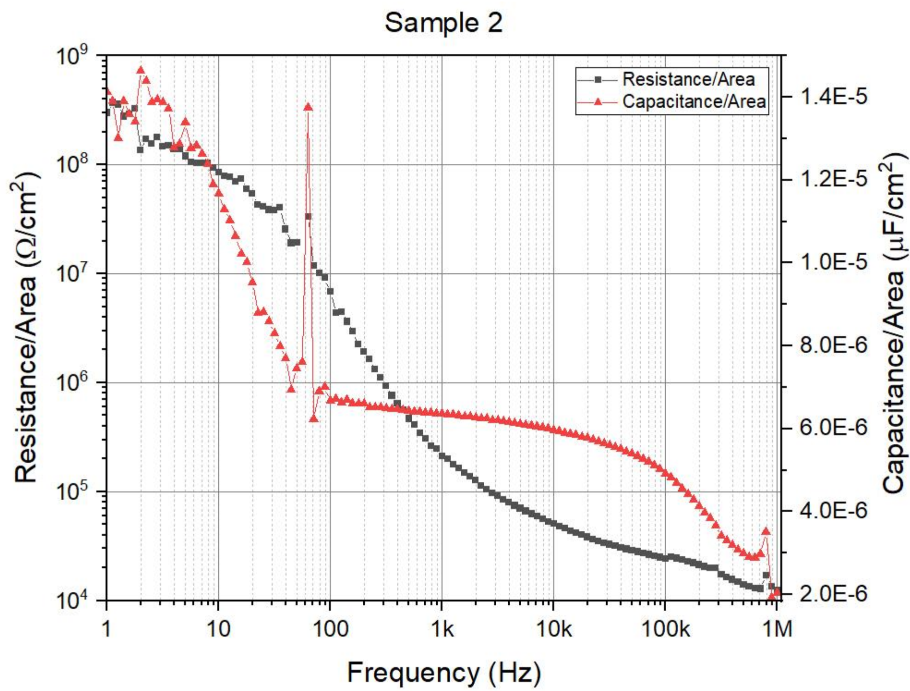

Figure 4.12: Resistance/area ($R_{nApSi/Si}$) and capacitance/area ($C_{nApSi/Si}$) vs. frequency plots for pSi/Si Sample 2

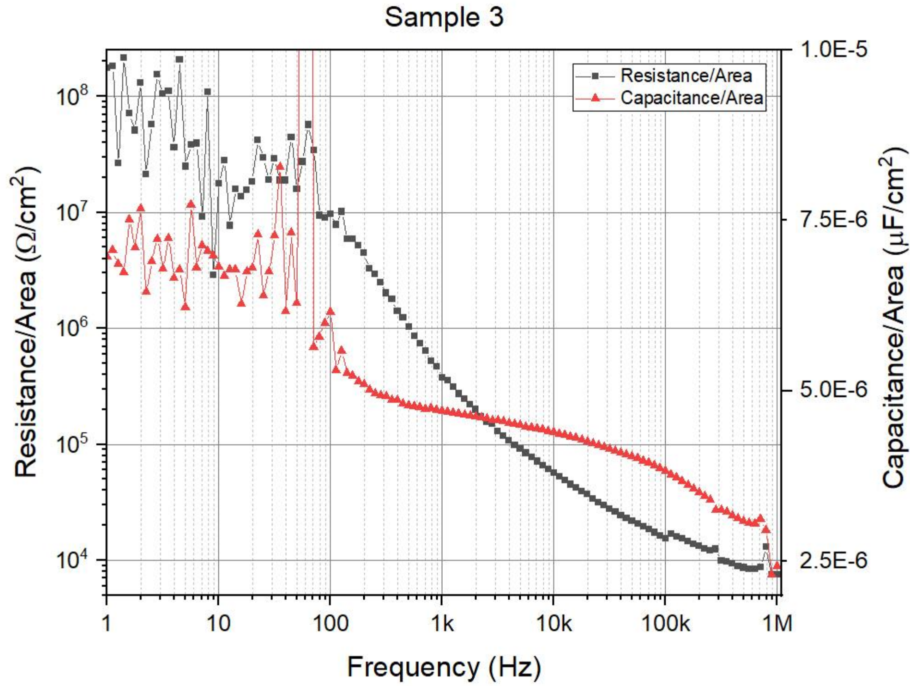

Figure 4.13: Resistance/area ($R_{nApSi/Si}$) and capacitance/area ($C_{nApSi/Si}$) vs. frequency plots for pSi/Si Sample 3

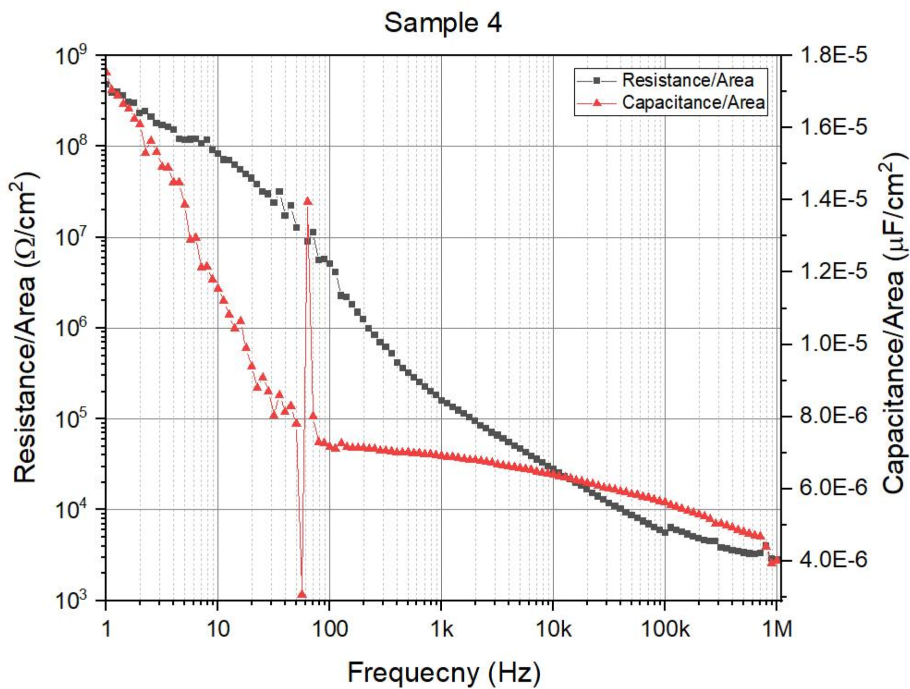

Figure 4.14: Resistance/area ($R_{nApSi/Si}$) and capacitance/area ($C_{nApSi/Si}$) vs. frequency plots for pSi/Si Sample 4

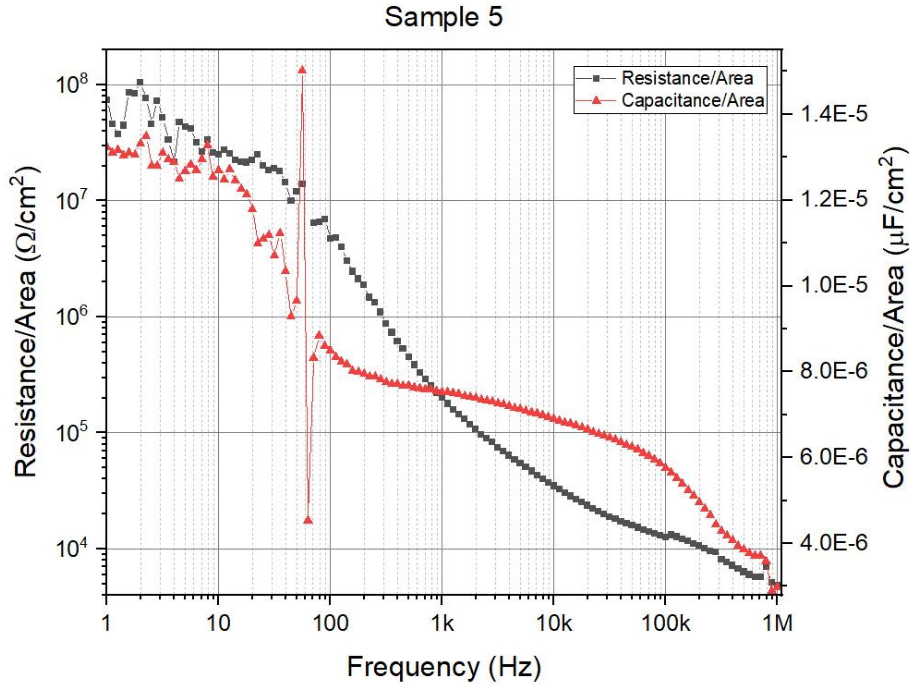

Figure 4.15: Resistance/area ($R_{nApSi/Si}$) and capacitance/area ($C_{nApSi/Si}$) vs. frequency plots for pSi/Si Sample 5

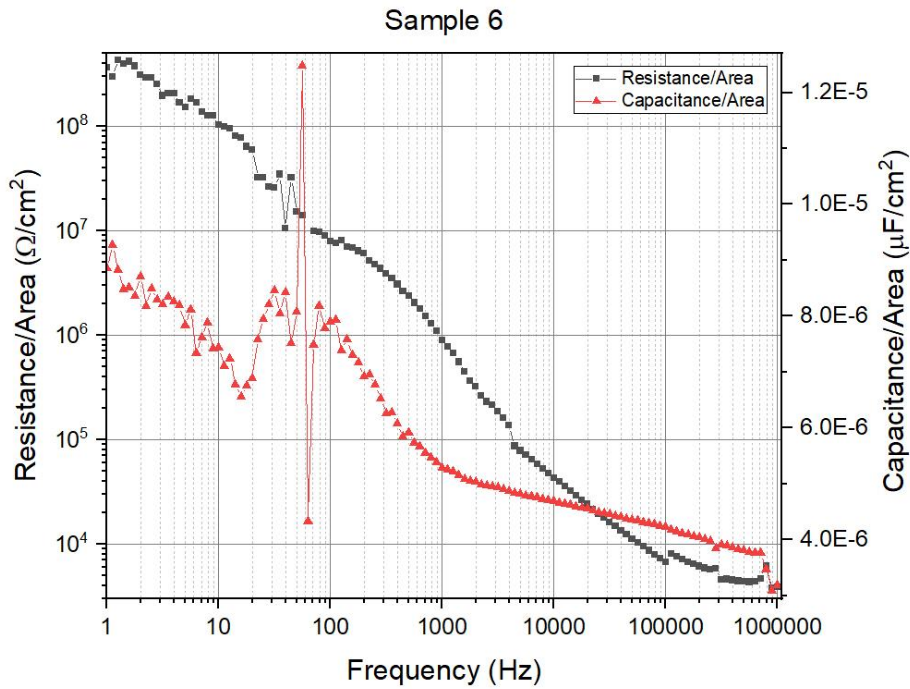

Figure 4.16: Resistance/area ($R_{nApSi/Si}$) and capacitance/area ($C_{nApSi/Si}$) vs. frequency plots for pSi/Si Sample 6

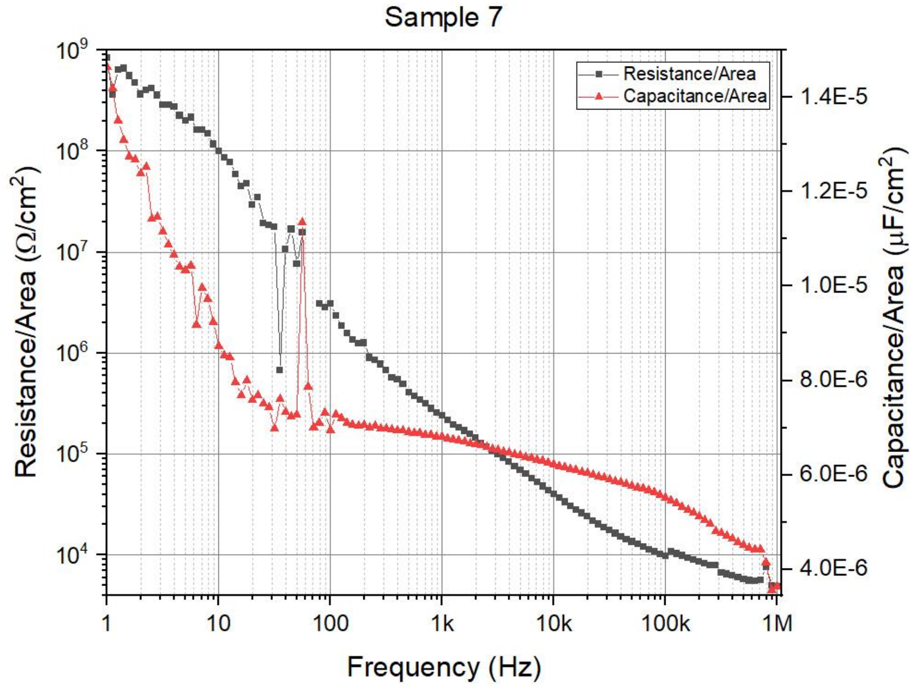

Figure 4.17: Resistance/area ($R_{nApSi/Si}$) and capacitance/area ($C_{nApSi/Si}$) vs. frequency plots for pSi/Si Sample 7

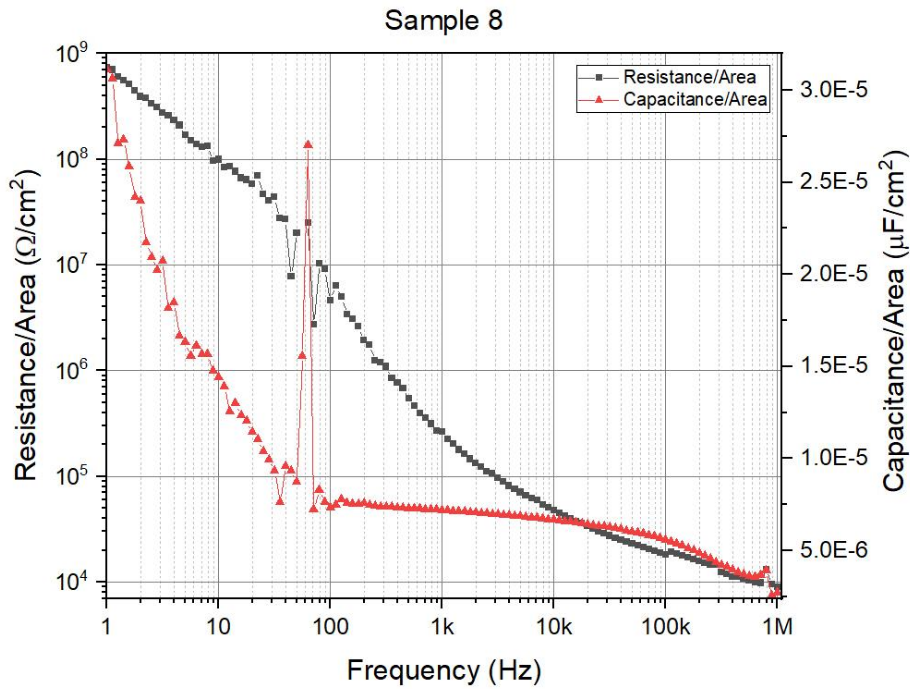

Figure 4.18: Resistance/area ($R_{nApSi/Si}$) and capacitance/area ($C_{nApSi/Si}$) vs. frequency plots for pSi/Si Sample 8

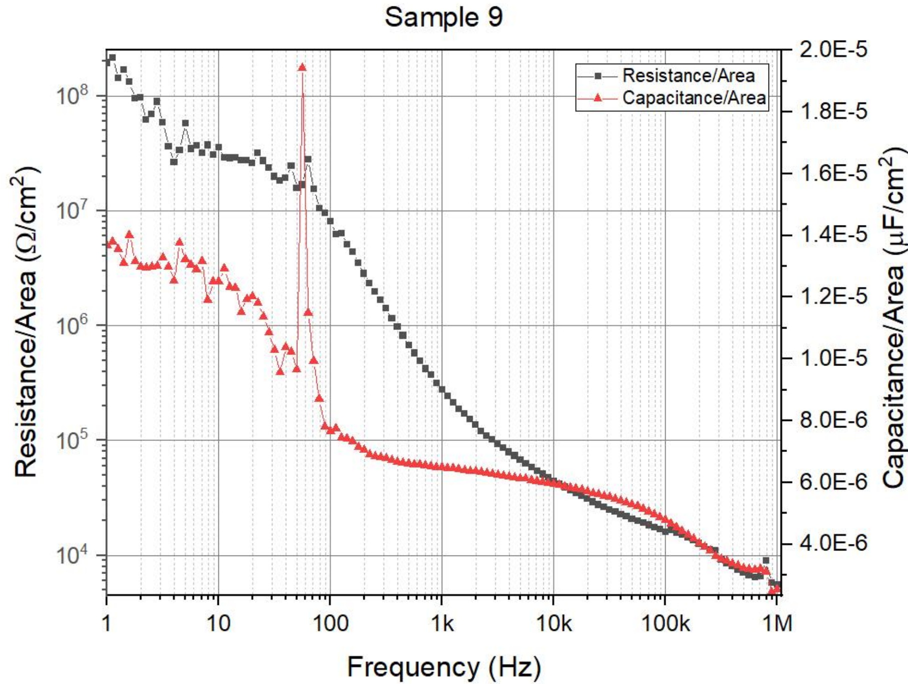

Figure 4.19: Resistance/area ($R_{nApSi/Si}$) and capacitance/area ($C_{nApSi/Si}$) vs. frequency plots for pSi/Si Sample 9

$C_{nApSi/Si}$ at both 25kHz and 50kHz showed good performance in ANOVA analysis that is at least one parameter P-value was less than 0.05. At 25 kHz for $C_{nApSi/Si}$, both power and pressure had a P-value less than 0.05 (0.04 & 0.048 respectively); at 50 kHz power had a P-value less than 0.05 (0.048) and pressure had a P-value slightly over 0.05 (0.061). $R_{nApSi/Si}$ at 25kHz showed good ANOVA performance (power P-value 0.002<0.05 and pressure P-value 0.004<0.05). However, at 50 kHz ANOVA performance of $R_{nApSi/Si}$ was not statistically significant (all parameters P-value > 0.05, closest is power- P-value 0.084). S/N response of $R_{nApSi/Si}$ at 25kHz is shown in Figure 4.20, at 50kHz shown in Figure 4.21. For $C_{nApSi/Si}$, Figure 4.22 shows the S/N response at 25kHz, Figure 4.23 shows the S/N response at 50kHz. Table 4.7 and 4.8 shows the summary of ANOVA analysis for $R_{nApSi/Si}$ at 25kHz and 50kHz respectively. Table 4.9 and 4.10 shows the summary of ANOVA analysis for $C_{nApSi/Si}$ at 25kHz

and 50kHz respectively. Both $R_{nApSi/Si}$ and $C_{nApSi/Si}$ responded in similar fashion at 25kHz and 50kHz, but as previously mentioned $R_{nApSi/Si}$ data at 25kHz showed better ANOVA performance.

Table 4.6: Summary of electrical properties of pSi/Si thin film samples.

Sample No.	$\frac{Resistance}{Area}$ at 25kHz (Ω/cm^2)	$\frac{Resistance}{Area}$ at 50kHz (Ω/cm^2)	$\frac{Capacitance}{Area}$ at 25kHz (Ω/cm^2)	$\frac{Capacitance}{Area}$ at 50kHz (Ω/cm^2)
pSi Sample 1	2.57×10^{4}	1.74×10^{4}	3.48×10^{-6}	3.38×10^{-6}
pSi Sample 2	$3..52\times10^{4}$	2.89×10^{4}	5.69×10^{-6}	5.40×10^{-6}
pSi Sample 3	3.17×10^{4}	2.19×10^{4}	4.21×10^{-6}	4.04×10^{-6}
pSi Sample 4	1.41×10^{4}	0.87×10^{4}	6.08×10^{-6}	5.86×10^{-6}
pSi Sample 5	2.10×10^{4}	1.59×10^{4}	6.56×10^{-6}	6.25×10^{-6}
pSi Sample 6	1.95×10^{4}	1.12×10^{4}	4.50×10^{-6}	4.36×10^{-6}
pSi Sample 7	2.02×10^{4}	1.35×10^{4}	5.97×10^{-6}	5.78×10^{-6}
pSi Sample 8	3.02×10^{4}	2.31×10^{4}	6.36×10^{-6}	6.05×10^{-6}
pSi Sample 9	2.76×10^{4}	2.08×10^{4}	5.62×10^{-6}	5.29×10^{-6}

The power and pressure S/N response for resistance/area ($R_{nApSi/Si}$)of pSi/Si thin films is almost similar to the S/N response for resistance/area ($R_{nSiO_2/Si}$) of SiO_2/Si thin films. As detailed explanation has been given in section 4.4 about the reasons which attributed this kind of S/N response for resistance/area ($R_{nSiO_2/Si}$) of SiO_2/Si thin films, it is not described in this section again for resistance/area ($R_{nApSi/Si}$)of pSi/Si thin films. Similar to $R_{nSiO_2/Si}$, the effect of Ar gas flow rate on $R_{nApSi/Si}$ is very little and also not satistically significant (P-value >>0.05 at both 25kHz and 50kHz).

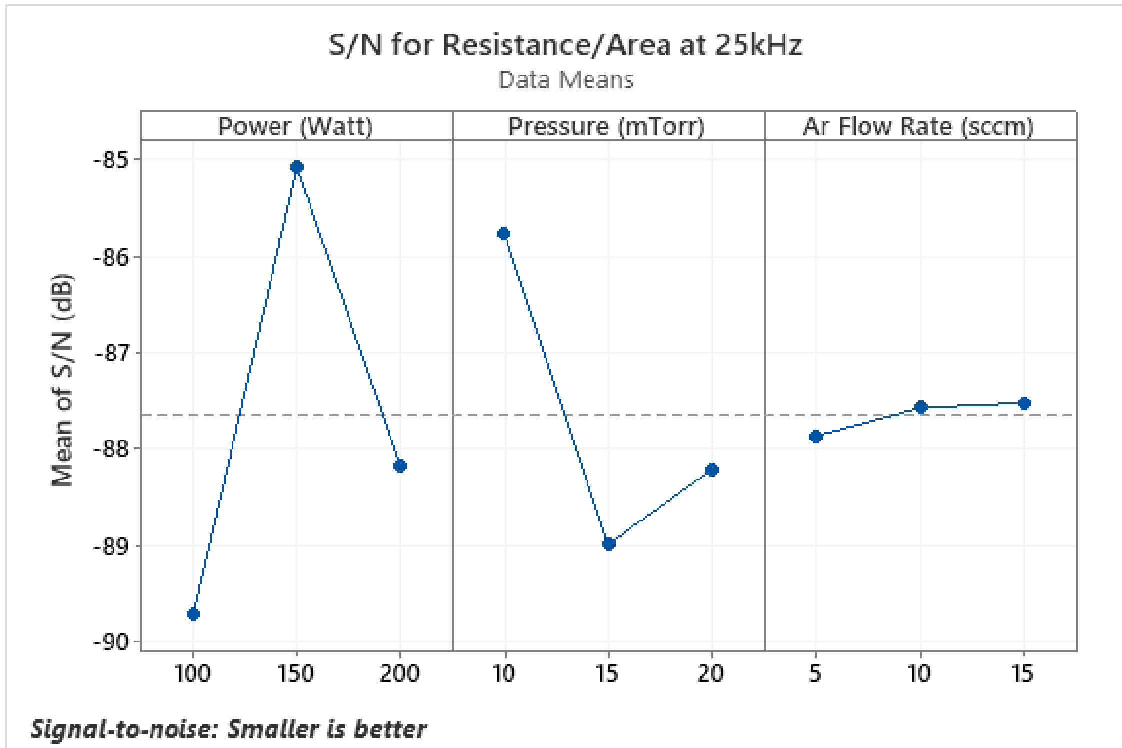

Figure 4.20: S/N graph for the resistance/area ($R_{nApSi/Si}$) of pSi/Si thin films at 25kHz

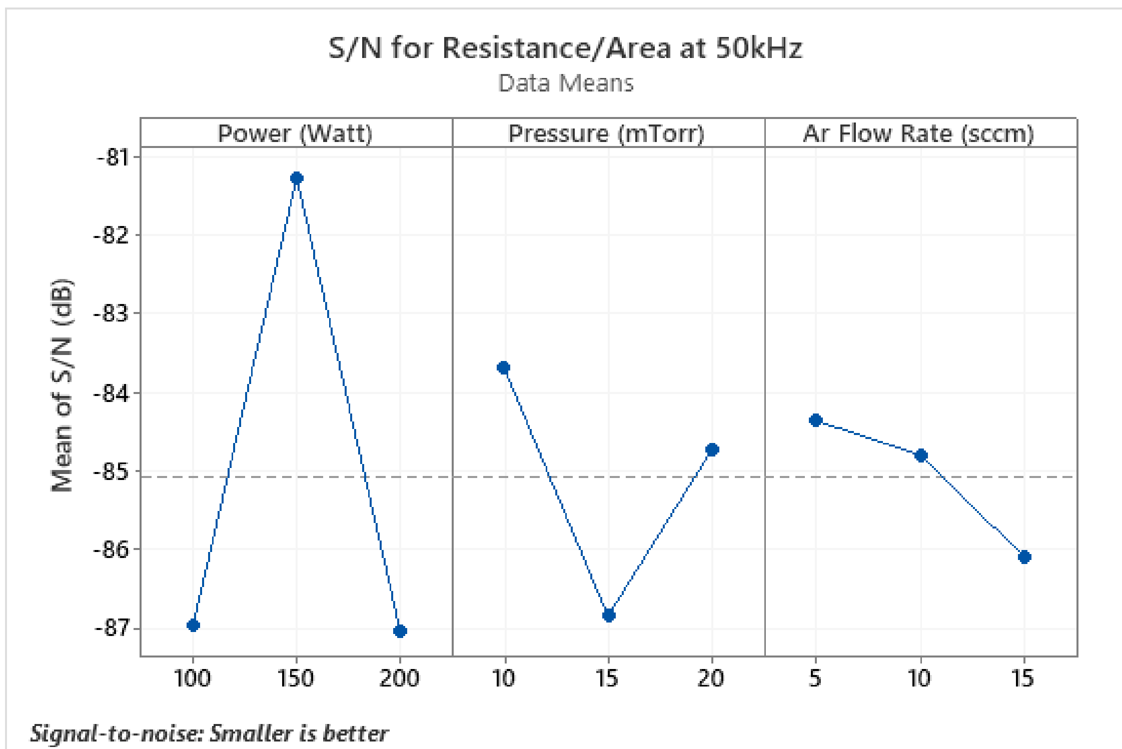

Figure 4.21: S/N graph for the resistance/area ($R_{nApSi/Si}$) of pSi/Si thin films at 50kHz

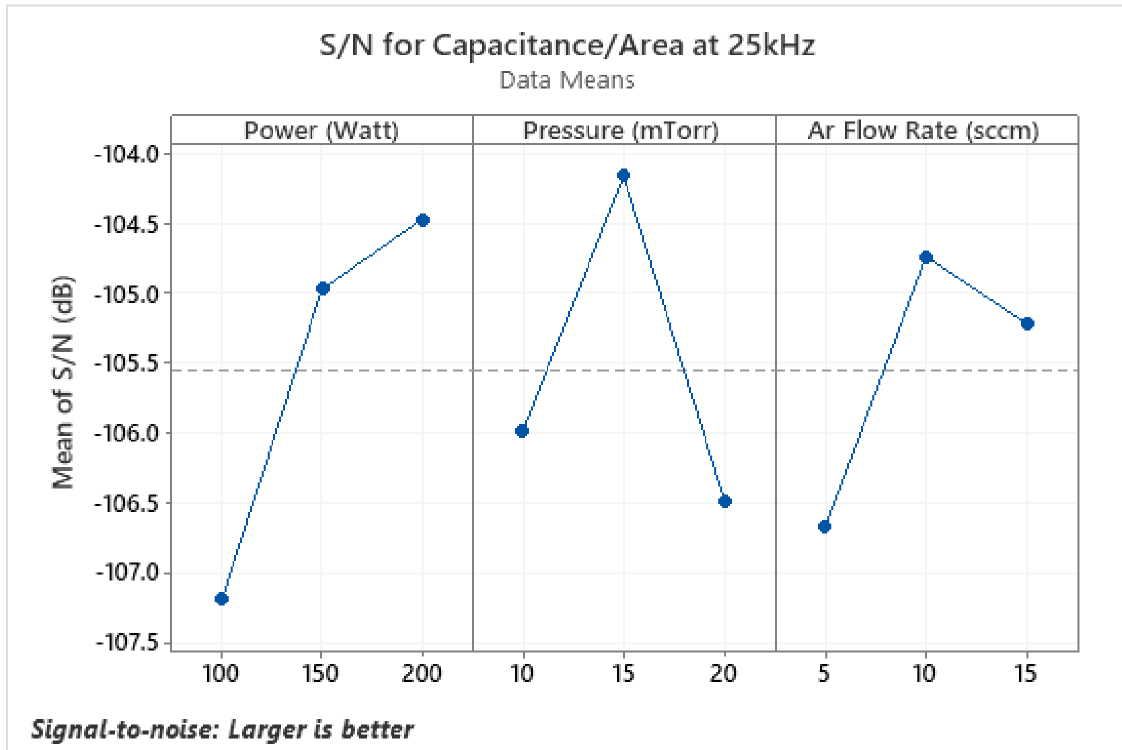

Figure 4.22: S/N graph for the capacitance/area ($C_{nApSi/Si}$) of pSi/Si thin films at 25kHz

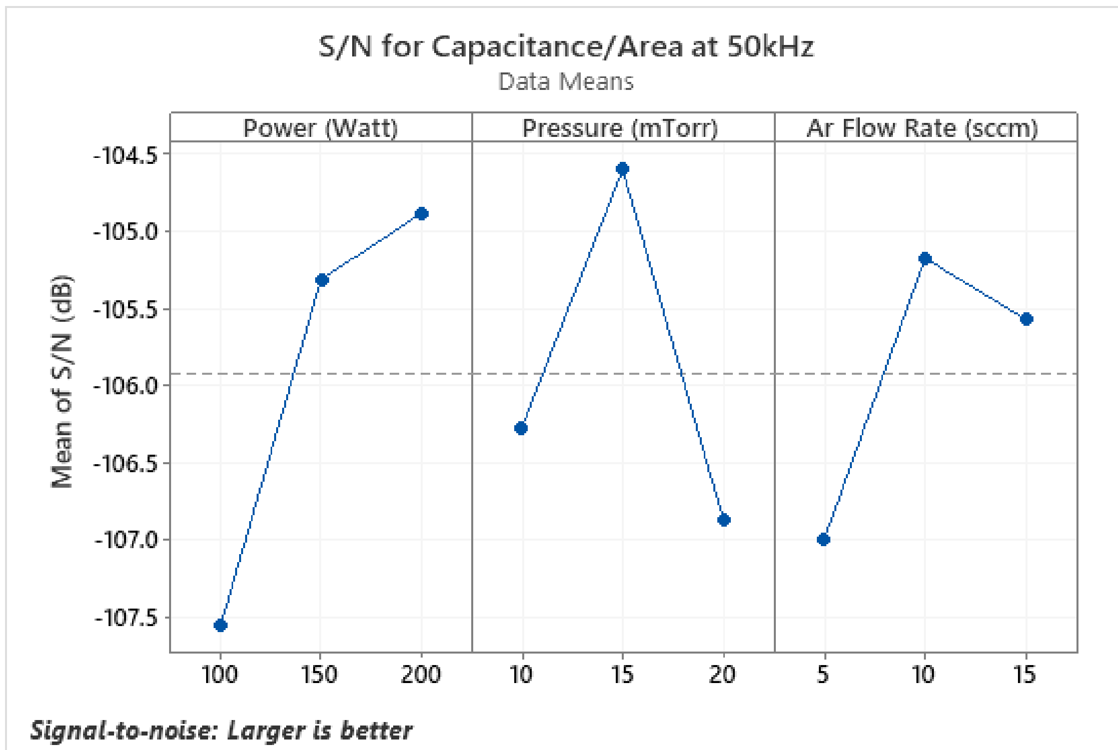

Figure 4.23: S/N graph for the capacitance/area ($C_{nApSi/Si}$) of pSi/Si thin films at 50kHz

Table 4.7: Summary of ANOVA result for resistance/area ($R_{nApSi/Si}$) at 25 kHz frequency for pSi/Si thin films

Source	DF	Seq SS	Contribution	Adj SS	Adj MS	F-Value	P-Value
Power (Watt)	2	2.45E+8	65.97%	2.45E+8	1.22E+8	494.33	0.002
Pressure (mTorr)	2	1.23E+8	33.16%	1.23E+8	6.16E+7	248.47	0.004
Ar Gas Flow (sccm)	2	2.72E+6	0.73%	2.72E+6	1.36+6	5.49	0.154
Error	2	4.96E+5	0.13%	4.96E+5	2.48E+5		
Total	8	3.71E+8	100.00%				

Table 4.8: Summary of ANOVA result for resistance/area ($R_{nApSi/Si}$) at 50 kHz frequency for pSi/Si thin films

Source	DF	Seq SS	Contribution	Adj SS	Adj MS	F-Value	P-Value
Power (Watt)	2	2.28E+8	69.88%	2.28E+8	1.14E+8	10.87	0.084
Pressure (mTorr)	2	6.10E+7	18.74%	6.10E+7	3.05E+7	2.92	0.255
Ar Gas Flow (sccm)	2	1.62E+7	4.96%	1.62E+7	8.08+6	0.77	0.564
Error	2	2.09E+7	6.43%	2.09E+7	1.05E+5		
Total	8	3.26E+8	100.00%				

Table 4.9: Summary of ANOVA result for capacitance/area ($C_{nApSi/Si}$) at 25 kHz frequency for pSi/Si thin films

Source	DF	Seq SS	Contribution	Adj SS	Adj MS	F-Value	P-Value
Power (Watt)	2	0.000000	43.58%	0.000000	0.000000	24.27	0.040
Pressure (mTorr)	2	0.000000	35.72%	0.000000	0.000000	19.89	0.058
Ar Gas Flow (sccm)	2	0.000000	18.91%	0.000000	0.000000	10.53	0.087
Error	2	0.000000	1.80%	0.000000	0.000000		
Total	8	0.000000	100.00%				

Table 4.10: Summary of ANOVA result for capacitance/area ($C_{nApSi/Si}$) at 50 kHz frequency for pSi/Si thin films

Source	DF	Seq SS	Contribution	Adj SS	Adj MS	F-Value	P-Value
Power (Watt)	2	0.000000	44.82%	0.000000	0.000000	19.98	0.048
Pressure (mTorr)	2	0.000000	34.80%	0.000000	0.000000	15.51	0.061
Ar Gas Flow (sccm)	2	0.000000	18.14%	0.000000	0.000000	8.09	0.110
Error	2	0.000000	2.24%	0.000000	0.000000		
Total	8	0.000000	100.00%				

One distinctive aspect of capacitance/area ($C_{nApSi/Si}$) of pSi/Si thin films from capacitance/area ($C_{nSiO_2/Si}$) of SiO_2/Si thin films is that $C_{nSiO_2/Si}$ went up from low to mid power level (150W to 200W) and descended down again from mid to high power level (200W to 250W), but $C_{nApSi/Si}$ only rose up when sputtering power is increased (Figure 4.22 & 4.23). At high power level, the slope, however, was less steep that that at low power level. In section 4.4 the reason behind the S/N response of $C_{nSiO_2/Si}$ was explained comprehensively. Same attributes were also in play for $C_{nApSi/Si}$. If the power level was a little bit higher (250W), it is to be expected same response as $C_{nSiO_2/Si}$ would have been observed for $C_{nApSi/Si}$, as at 200W the saturation of nucleation sites and rising nucleation growth and increasing layer thickness d_n already held down the increasing rate of $C_{nSiO_2/Si}$.

Since same pressure levels were used for depositing pSi/Si and SiO_2/Si thin films, pressure S/N response for $C_{nApSi/Si}$ and $C_{nSiO_2/Si}$ are identical, as expected. From the data in Table 4.9 and 4.10, it can be seen that Ar gas flow rate has a significant contribution (about 18%, P-values for both 25kHz and 50kHz are near to 0.05) to $C_{nApSi/Si}$ and the effect is analogous to pressure. It is hard to explain the sole effect of Ar gas flow rate on $C_{nApSi/Si}$ from the limited experiment carried out in this work and more extensive study needs to be performed to understand the effect of this parameter.

4.4 Adhesion

The adhesion of the pSi/Si thin films was examined by scotch tape test. All nine samples passed the adhesion test. They remain adhered to the Si substrate even after pulling off the tape.

4.5 Conclusion

pSi thin film samples were deposited over Si substrate by radio frequency (RF) magnetron sputtering system. Three sets of inputs for the three process parameters were chosen for sputtering pSi thin films- power levels were 100W, 150W and 200W; 5mTorr, 10mTorr and 15mTorr were chosen for pressure and three Ar gas flow rate levels at 5, 10 and 15 sccm were selected. Taguchi DOE and ANOVA analysis were performed to understand the effect of three process parameters-power, pressure and Ar gas flow rate and their individual contribution on surface, structural and electrical properties of the SiO_2/Si thin films. It was determined that power and pressure are the dominant factors that influence the significant percentage of the properties in most cases. Ar gas flow rate has little effect on most of the properties of the sputtered pSi/Si thin films except capacitance/area ($C_{nApSi/Si}$).

CHAPTER V

FUTURE WORKS

The works that has been done in this research are characterizations of RF sputtered SiO_2/Si and pSi/Si thin films and study of the effect of the process parameter on their structural, morphological and electrical properties. The effect of three process parameters- power, pressure and Ar gas flow rate was investigated. There is another process parameter of importance; that is thermal annealing. The effect of thermal annealing on the deposited SiO_2/Si and pSi/Si thin film is one potential future work. Characterization of RF sputtered nSi/Si thin films and study of the effect of the process parameter on their structural, morphological and electrical properties is another research that can be performed based on this research work. So, let's point out the potential future work in numerical order:

1. Characterization of RF sputtered nSi/Si thin films and study of the effect of the process parameter on their structural, morphological and electrical properties.
2. Investigation of the effect of thermal annealing on SiO_2 thin films on Si substrate.
3. Investigation of the effect of thermal annealing on pSi thin films on Si substrate.
4. Investigation of the effect of thermal annealing on nSi thin films on Si substrate.

5.1 Fabrication of Enhancement Mode n-MOSFET by Physical Vapor Deposition

The ultimate target after characterizing the pSi/Si, nSi/Si and SiO_2/Si thin films is to fabricate n-MOSFET by Physical Vapor Deposition technique using sputtering system. A

growing methodology can be used to sputter the MOSFET layers which is depicted in Figure 5.1. First on the pSi substrate pSi overlayers will be sputtered. Between the overlayers nSi will be sputtered which will act as n-wells. SiO_2 insulation layer will be deposited on the middle pSi overlayer. Finally, source, gate, drain and body contact will be deposited. Any conducting metal can be used as contact.

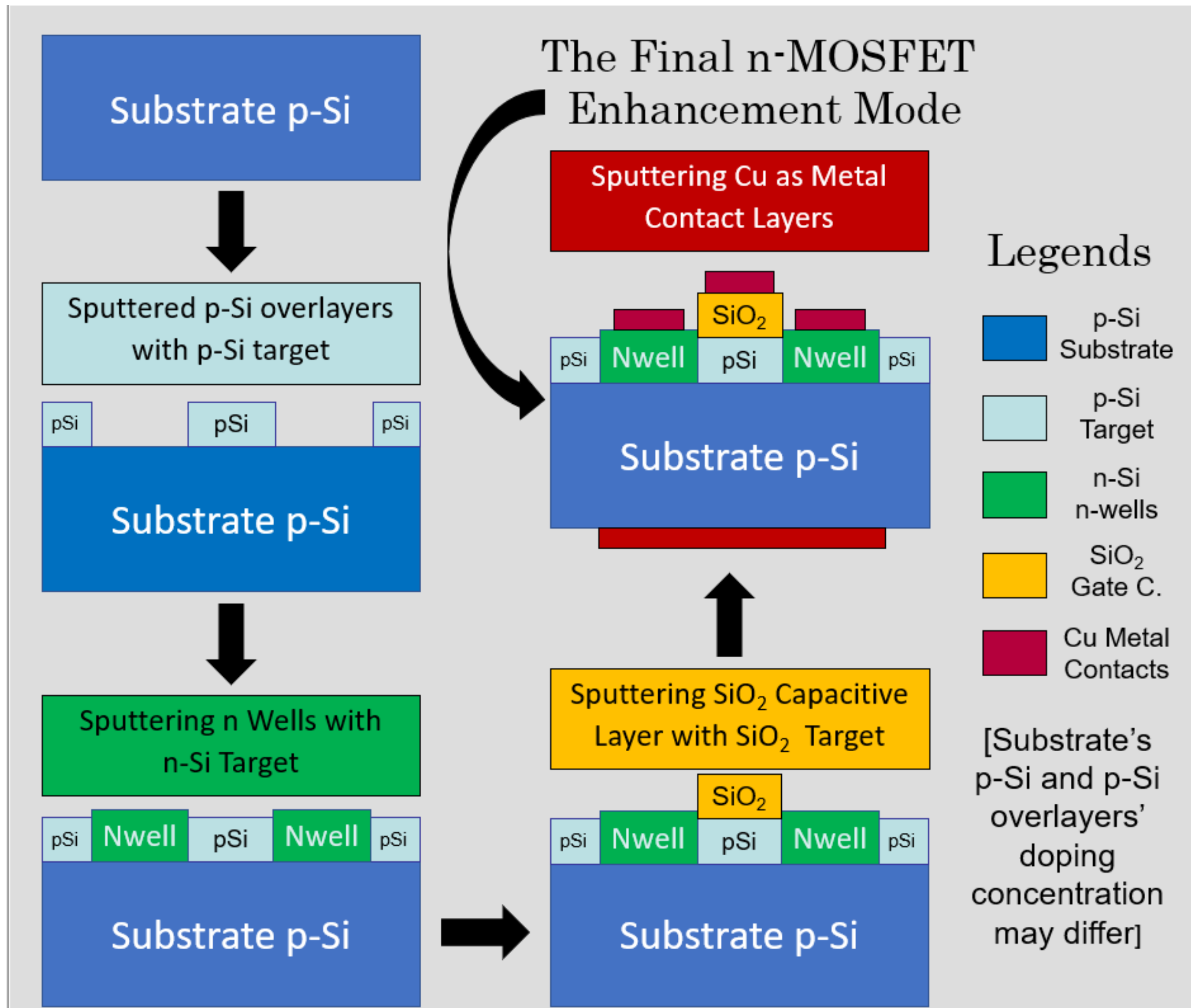

Figure 5.1: Methodology of MOSFET Fabrication by Physical Vapor Deposition

Some sample MOSFET were fabricated before the characterization experiments using the process parameters listed in Table 5.1 to deposit the pSi overlayers, nwells and SiO_2 insulation

layer. The fabricated enchance mode n-MOSFET using the sputtering system is shown in Figure 5.2. The I-V characteristics of one fabricated MOSFET sample is given in Figure 5.3.

Table 5.1: Process parameters used to deposit different layers of enchance mode n-MOSFET

Parameters / Layers	RF power (W)	Working pressure (mTorr)	Ar gas flow rate (sccm)	Deposition time (hour)
pSi overlayers	200	15	15	10
nSi nwells	200	15	15	13
SiO_2 insulation	200	15	15	8

Figure 5.2: Steps of n-MOSFET Fabrication. Si sample substrate (topleft), p-Si overlayers deposition and channel length (topright), n-well deposition and length (bottomleft) and final n-MOSFET samples with Cu contact layers (bottom right)

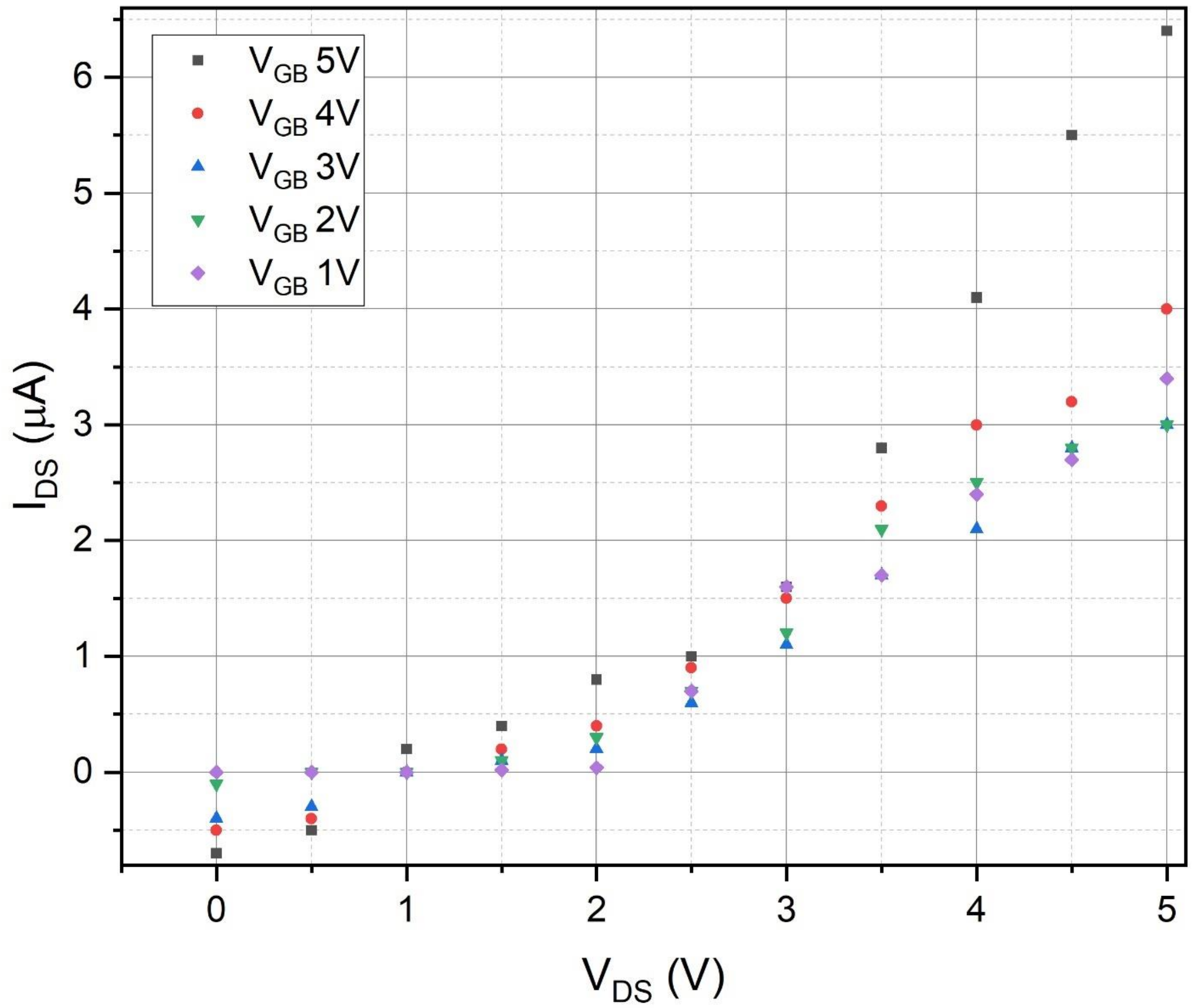

Figure 5.3: I-V characteristics of enhancement mode nMOSFET fabricated by Physical Vapor Deposition (PVD) technique.

The I-V characteristics of the PVD fabricated nMOSFET shows resemblences with the ideal MOSFET characteristics. From the characterization of pSi, SiO_2 and nSi, if suitable process parameters are chosen to fabricate the MOSFET layers with proper masking, then it can be expected that the PVD fabricated nMOSFET I-V performance will be identical to ideal nMOSFET I-V characteristics.

REFERENCES

[1] H. Föll. "Semiconductor Technology." https://www.tf.uni-kiel.de/matwis/amat/semitech_en/kap_3/backbone/r3_2_2.pdf (accessed).

[2] "Thin Film Material Market Size, Share & Trends Analysis Report By Application, Regional Outlook, Competitive Strategies, And Segment Forecasts, 2019 To 2025." https://www.grandviewresearch.com/industry-analysis/thin-film-material-market (accessed).

[3] Transperency Market Research. "Thin and Ultra-thin Films Market Size, Share, Trends, Growth, Export Value, Volume & Trade, Sales, Pricing Forecast." https://www.transparencymarketresearch.com/pressrelease/thin-ultra-thin-films-market.htm (accessed).

[4] Adroit Market Research, "Global Thin Film Market Size, Share & Industry Forecast 2020-2028." [Online]. Available: https://www.adroitmarketresearch.com/industry-reports/thin-film-market.

[5] J. Thirumalai, *Thin Film Processes: Artifacts on Surface Phenomena and Technological Facets*. InTechOpen, 2017.

[6] J. O. Carneiro, V. Teixeira, and S. Azevedo, "Residual Stresses in Thin Films Evaluated by Different Experimental Techniques," in *Encyclopedia of Thermal Stresses*, R. B. Hetnarski Ed. Dordrecht: Springer Netherlands, 2014, pp. 4222-4231.

[7] G. Abadias *et al.*, "Review Article: Stress in thin films and coatings: Current status, challenges, and prospects," *Journal of Vacuum Science & Technology A: Vacuum, Surfaces, and Films,* vol. 36, no. 2, 2018, doi: 10.1116/1.5011790.

[8] R. W. Hoffman, "Stress distributions and thin film mechanical properties," *Surface and Interface Analysis,* vol. 3, no. 1, pp. 62-66, February 1981, doi: https://doi.org/10.1002/sia.740030113.

[9] Y. Choi and S. Suresh, "Size effects on the mechanical properties of thin polycrystalline metal films on substrates," *Acta Materialia,* vol. 50, no. 7, pp. 1881-1893, doi: https://doi.org/10.1016/S1359-6454(02)00046-0.

[10] M. Hughes. "What is RF Sputtering?" Semicore Equipment, Inc. http://www.semicore.com/news/92-what-is-rf-sputtering (accessed).

[11] O. Briot. "RF magnetron sputtering." Laboratoire Charles Coulomb. (accessed).

[12] V. Bhatt and S. Chandra, "Silicon dioxide films by RF sputtering for microelectronic and MEMS applications," *Journal of Micromechanics and Microengineering,* vol. 17, no. 5, pp. 1066-1077, 2007, doi: 10.1088/0960-1317/17/5/029.

[13] W.-F. Wu and B.-S. Chiou, "Optical and mechanical properties of reactively sputtered silicon dioxide films," *Semiconductor Science and Technology,* vol. 11, no. 9, pp. 1317-1321, 1996.

[14] H. Pierson, O., *Handbook of Chemical Vapor Deposition (CVD)*, 2nd ed. (Principles, Technology and Applications). Park Ridge, New Jersey, USA: Noyes Publications.

[15] S. Robles, E. Yieh, and B. Nguyen, C., "Moisture resistance of plasma enhanced chemical vapor deposited oxides used for ultra-large scale integrated device applications," *Journal of The Electrochemical Society,* vol. 142, 2, pp. 580-585, 1995.

[16] Z. Cao, T.-Y. Zhang, and X. Zhang, "Microbridge testing of plasma-enhanced chemical-vapor deposited silicon oxide films on silicon wafers," *Journal of Applied Physics,* vol. 97, no. 10, 2005, doi: 10.1063/1.1898449.

[17] V. Jaecklin, P., C. Linder, N. de Rooij, F. , J. Moret, M., and R. Vuilleumier, "Line-addressable torsional micromirrors for light modulator arrays," *Sensors and Actuators A: Physical,* vol. 41, no. 1-3, pp. 324-329, April 1994, doi: https://doi.org/10.1016/0924-4247(94)80131-2.

[18] W. Tang, C., T. Nguyen, C., H., and R. Howe, T., "Laterally driven polysilicon resonant microstructures," in *IEEE International Conference on Micro Electro Mechanical Systems*, Salt Lake City, UT, USA, 1989: IEEE, p. 6, doi: 10.1109/MEMSYS.1989.77961.

[19] L. Zhao, C. Zhao, J. Liu, Z. Liu, and Y. Chen, "Effect of sputtering pressure on the structure and properties of SiO2 films prepared by magnetron sputtering," *Micro & Nano Letters,* vol. 15, no. 12, pp. 872-876, 2020, doi: 10.1049/mnl.2020.0222.

[20] İ. Kanmaz and A. ÜZÜM, "Silicon dioxide thin films prepared by spin coating for the application of solar cells," *International Advanced Researches and Engineering Journal,* vol. 5, no. 1, pp. 14-18, 2021, doi: 10.35860/iarej.784328.

[21] W. J. Ho, J. C. Lin, J. J. Liu, W. B. Bai, and H. P. Shiao, "Electrical and Optical Characterization of Sputtered Silicon Dioxide, Indium Tin Oxide, and Silicon Dioxide/Indium Tin Oxide Antireflection Coating on Single-Junction GaAs Solar Cells," *Materials (Basel),* vol. 10, no. 7, Jun 26 2017, doi: 10.3390/ma10070700.

[22] Y. Jiang *et al.*, "Optical and interfacial layer properties of SiO2 films deposited on different substrates," *Appl Opt,* vol. 53, no. 4, pp. A83-7, Feb 1 2014, doi: 10.1364/AO.53.000A83.

[23] Y. Yang *et al.*, "Preparation of a novel TiN/TiNxOy/SiO2 composite ceramic films on aluminum substrate as a solar selective absorber by magnetron sputtering," *Journal of Alloys and Compounds,* vol. 815, 2020, doi: 10.1016/j.jallcom.2019.152209.

[24] H. Bartzsch, D. Glöß, B. Böcher, P. Frach, and K. Goedicke, "Properties of SiO2 and Al2O3 films for electrical insulation applications deposited by reactive pulse magnetron sputtering," *Surface and Coatings Technology,* vol. 174-175, pp. 774-778, 2003, doi: 10.1016/s0257-8972(03)00384-0.

[25] B. J. Choi, A. B. Chen, X. Yang, and I. W. Chen, "Purely electronic switching with high uniformity, resistance tunability, and good retention in Pt-dispersed SiO2 thin films for ReRAM," *Adv Mater,* vol. 23, no. 33, pp. 3847-52, Sep 1 2011, doi: 10.1002/adma.201102132.

[26] D. Tahir *et al.*, "Electronic and optical properties of Al2O3/SiO2thin films grown on Si substrate," *Journal of Physics D: Applied Physics,* vol. 43, no. 25, 2010, doi: 10.1088/0022-3727/43/25/255301.

[27] H. Bartzsch *et al.*, "Electrical insulation properties of sputter-deposited SiO2, Si3N4and Al2O3films at room temperature and 400 °C," *physica status solidi (a),* vol. 206, no. 3, pp. 514-519, 2009, doi: 10.1002/pssa.200880481.

[28] B. V. T. Hanby, B. W. Stuart, M. Gimeno-Fabra, J. Moffat, C. Gerada, and D. M. Grant, "Layered Al2O3-SiO2 and Al2O3-Ta2O5 thin-film composites for high dielectric

strength, deposited by pulsed direct current and radio frequency magnetron sputtering," *Applied Surface Science,* vol. 492, pp. 328-336, 2019, doi: 10.1016/j.apsusc.2019.06.202.

[29] S.-H. Jeong, J.-K. Kim, B.-S. Kim, S.-H. Shim, and B.-T. Lee, "Characterization of SiO2 and TiO2 films prepared using rf magnetron sputtering and their application to anti-reflection coating," *Vacuum,* vol. 76, no. 4, pp. 507-515, 2004, doi: 10.1016/j.vacuum.2004.06.003.

[30] H. Kawasaki, T. Ohshima, Y. Yagyu, T. Ihara, M. Shinohara, and Y. Suda, "Preparation of Sn doped SiO2thin films by magnetron sputtering deposition using metal and metal-oxide powder targets," *Japanese Journal of Applied Physics,* vol. 58, no. SA, 2019, doi: 10.7567/1347-4065/aaea67.

[31] R. Biron, C. Pahud, F.-J. Haug, J. Escarré, K. Söderström, and C. Ballif, "Window layer with p doped silicon oxide for high Voc thin-film silicon n-i-p solar cells," *Journal of Applied Physics,* vol. 110, no. 12, 2011, doi: 10.1063/1.3669389.

[32] S. B. Concari, R. H. Buitrago, M. T. Gutiérrez, and J. J. Gandía, "Electric transport mechanism in intrinsic andp-doped microcrystalline silicon thin films," *Journal of Applied Physics,* vol. 94, no. 4, pp. 2417-2422, 2003, doi: 10.1063/1.1593215.

[33] E. Fathi, Y. Vygranenko, M. Vieira, and A. Sazonov, "Boron-doped nanocrystalline silicon thin films for solar cells," *Applied Surface Science,* vol. 257, no. 21, pp. 8901-8905, 2011, doi: 10.1016/j.apsusc.2011.05.052.

[34] T. N. Truong *et al.*, "Deposition pressure dependent structural and optoelectronic properties of ex-situ boron-doped poly-Si/SiOx passivating contacts based on sputtered silicon," *Solar Energy Materials and Solar Cells,* vol. 215, 2020, doi: 10.1016/j.solmat.2020.110602.

[35] C. Zhang *et al.*, "Optical and Electrical Effects of p-typeμc-SiOx:H in Thin-Film Silicon Solar Cells on Various Front Textures," *International Journal of Photoenergy,* vol. 2014, pp. 1-10, 2014, doi: 10.1155/2014/176965.

[36] A. A. Arie and J. K. Lee, "Electrochemical Properties of P-Doped Silicon Thin Film Anodes of Lithium Ion Batteries," *Materials Science Forum,* vol. 737, pp. 80-84, 2013, doi: 10.4028/www.scientific.net/MSF.737.80.

[37] N. H. Pham *et al.*, "High thermoelectric power factor of p-type amorphous silicon thin films dispersed with ultrafine silicon nanocrystals," *Journal of Applied Physics,* vol. 127, no. 24, 2020, doi: 10.1063/5.0004318.

[38] P. Alpuim *et al.*, "Study of the piezoresistivity of doped nanocrystalline silicon thin films," *Journal of Applied Physics,* vol. 109, no. 12, 2011, doi: 10.1063/1.3599881.

[39] K. Ketroussi *et al.*, "Study of boron doped amorphous silicon lightly hydrogenated prepared by DC magnetron sputtering for infrared detectors applications," *Infrared Physics & Technology,* vol. 113, 2021, doi: 10.1016/j.infrared.2020.103556.

[40] P. Pal and S. Chandra, "RF sputtered silicon for MEMS," *Journal of Micromechanics and Microengineering,* vol. 15, no. 8, pp. 1536-1546, 2005, doi: 10.1088/0960-1317/15/8/023.

[41] W. Wang, J. Huang, W. Xu, J. Huang, Y. Zeng, and W. Song, "Electrical properties of boron- and phosphorous-doped microcrystalline silicon thin films prepared by magnetron sputtering of heavily doped silicon targets," *Journal of Materials Science: Materials in Electronics,* vol. 24, no. 6, pp. 2122-2127, 2013, doi: 10.1007/s10854-013-1068-7.

[42] K. Haberle and E. Froschle, "Electrical properties and structure of boron-doped sputter-deposited polycrystalline silicon films," *Thin Solid Films,* vol. 61, no. 1, pp. 105-113, 1979, doi: https://doi.org/10.1016/0040-6090(79)90506-6.

[43] A. Tabata, J. Nakano, K. Mazaki, and K. Fukaya, "Film-thickness dependence of structural and electrical properties of boron-doped hydrogenated microcrystalline silicon prepared by radiofrequency magnetron sputtering," *Journal of Non-Crystalline Solids,* vol. 356, no. 23-24, pp. 1131-1134, 2010, doi: 10.1016/j.jnoncrysol.2010.04.011.

[44] H. Cesiulis, N. Tsyntsaru, A. Ramanavicius, and G. Ragoisha, "The Study of Thin Films by Electrochemical Impedance Spectroscopy," in *Nanostructures and Thin Films for Multifunctional Applications*, (NanoScience and Technology, 2016, ch. Chapter 1, pp. 3-42.

[45] M. Chaik, S. Ben Moumen, R. Bouferra, A. Outzourhit, and L. Essaleh, "Analysis of the electrical impedance spectroscopy measurements of ZnTe:Ni thin film deposited by R–F sputtering," *Superlattices and Microstructures,* vol. 137, 2020, doi: 10.1016/j.spmi.2019.106319.

[46] S. Dabbabi, M. Souli, T. Ben Nasr, A. Garcia-Loureiro, and N. Kamoun, "Effects of Ni and La Dopants on the Properties of ZnO and SnO2 Thin Films: Microstructural, Optical and Impedance Spectroscopy Studies," *Journal of Electronic Materials,* vol. 49, no. 2, pp. 1314-1321, 2019, doi: 10.1007/s11664-019-07784-5.

[47] C. Erinmwingbovo *et al.*, "Dynamic impedance spectroscopy of LiMn2O4 thin films made by multi-layer pulsed laser deposition," *Electrochimica Acta,* vol. 331, 2020, doi: 10.1016/j.electacta.2019.135385.

[48] H.-L. Hsu, C.-B. Yang, C.-H. Huang, and C.-Y. Hsu, "Electrical and optical studies of Ga-doped ZnO thin films," *Journal of Materials Science: Materials in Electronics,* vol. 24, no. 1, pp. 13-19, 2012, doi: 10.1007/s10854-012-0735-4.

[49] P.-c. Huang, C.-h. Huang, M.-y. Lin, C.-y. Chou, C.-y. Hsu, and C.-g. Kuo, "The Effect of Sputtering Parameters on the Film Properties of Molybdenum Back Contact for CIGS Solar Cells," *International Journal of Photoenergy,* vol. 2013, pp. 1-8, 2013, doi: 10.1155/2013/390824.

[50] Minitab® 18 Support. "What is the signal-to-noise ratio in a Taguchi design?" Minitab® 18 Support. https://support.minitab.com/en-us/minitab/18/help-and-how-to/modeling-statistics/doe/supporting-topics/taguchi-designs/what-is-the-signal-to-noise-ratio/ (accessed).

[51] P. S. Kao and H. Hocheng, "Optimization of electrochemical polishing of stainless steel by grey relational analysis," *Journal of Materials Processing Technology,* vol. 140, no. 1-3, pp. 255-259, 2003, doi: 10.1016/s0924-0136(03)00747-7.

[52] W. Yang, H. and Y. Tarng, S., "Design optimization of cutting parameters for turning operations based on the Taguchi metho," *Journal of Materials Processing Technology,* vol. 84, no. 1-3, pp. 122-129, 1998, doi: https://doi.org/10.1016/S0924-0136(98)00079-X.

[53] Minitab® 18 Support. "Model summary table for Fit Regression Model." Minitab® 18 Support. https://support.minitab.com/en-us/minitab/18/help-and-how-to/modeling-statistics/regression/how-to/fit-regression-model/interpret-the-results/all-statistics-and-graphs/model-summary-table/ (accessed).

[54] H.-M. Wu *et al.*, "Structure and electrical properties of Mo back contact for Cu(In, Ga)Se2 solar cells," *Vacuum,* vol. 86, no. 12, pp. 1916-1919, 2012, doi: 10.1016/j.vacuum.2012.04.036.

[55] A. C. Badgujar, S. R. Dhage, and S. V. Joshi, "Process parameter impact on properties of sputtered large-area Mo bilayers for CIGS thin film solar cell applications," *Thin Solid Films,* vol. 589, pp. 79-84, 2015, doi: 10.1016/j.tsf.2015.04.046.

[56] M.-T. Le, Y.-U. Sohn, J.-W. Lim, and G.-S. Choi, "Effect of Sputtering Power on the Nucleation and Growth of Cu Films Deposited by Magnetron Sputtering," *Materials Transactions,* vol. 51, no. 1, pp. 116-120, 2010, doi: 10.2320/matertrans.M2009183.

[57] RRUFF. "Si." https://rruff.info/Silicon (accessed).

[58] P. Zaumseil, "High-resolution characterization of the forbidden Si 200 and Si 222 reflections," *J Appl Crystallogr,* vol. 48, no. Pt 2, pp. 528-532, Apr 1 2015, doi: 10.1107/S1600576715004732.

[59] M. Chrostowski *et al.*, "Low temperature epitaxial growth of boron-doped silicon thin films," 2018.

[60] Z.-H. Li, E.-S. Cho, and S. J. Kwon, "Molybdenum thin film deposited by in-line DC magnetron sputtering as a back contact for Cu(In,Ga)Se2 solar cells," *Applied Surface Science,* vol. 257, no. 22, pp. 9682-9688, 2011, doi: 10.1016/j.apsusc.2011.06.101.

[61] P. Chelvanathan *et al.*, "Effects of RF magnetron sputtering deposition process parameters on the properties of molybdenum thin films," *Thin Solid Films,* vol. 638, pp. 213-219, 2017, doi: 10.1016/j.tsf.2017.07.057.

APPENDIX A

APPENDIX A

NOMENCLATURES

SiO_2/Si	SiO_2 thin film over Si substrate
pSi/Si	pSi thin film over Si substrate
DOE	Design of experiments
sccm	Standard cubic cm per minute
S/N	Signal to Noise Ratio
DF	Degrees of Freedom
Seq SS	Sequential sum of squares
Adj SS	Adjusted sum of squares
Adj MS	Adjusted mean of squares
R^2 (adj)	R^2 adjusted
R^2 pred)	R^2 predicted
R_a	Average surface roughness
$R_{nASiO_2/Si}$	Resistance/Area of nth SiO_2/Si samples
$C_{nASiO_2/Si}$	Capacitance/Area of nth SiO_2/Si samples

R_{Si}	Resistance of the Si Substrate
C_{Si}	Capacitance of the Si Substrate
R_{nSiO_2}	Resistance of the nth SiO_2 film
C_{nSiO_2}	Resistance of the nth SiO_2 film
$R_{nSiO_2/Si}$	Resistance of nth SiO_2/Si samples
$C_{nSiO_2/Si}$	Capacitance of nth SiO_2/Si samples
$R_{nApSi/Si}$	Resistance/Area of nth pSi/Si samples
$C_{nApSi/Si}$	Capacitance/Area of nth pSi/Si samples
$Z_{nSiO_2/Si}$ (real)	Real part of impedance of nth SiO_2/Si samples
$Z_{nSiO_2/Si}$ (img)	Imaginary part of impedance of nth SiO_2/Si samples
d_n	Layer thickness of nth sample
d_{Si}	Layer thickness the Si substrate
A_n	Area of the nth thin film sample
ANOVA	Analysis of Variance
RF	Radio Frequency
AFM	Atomic Force Microscopy
SEM	Scanning Electron Microscopy
XRD	X-ray Diffractometry

APPENDIX B

APPENDIX B

GLOSSARIES

MEMS: Micro Electro-Mechanical System. A system that integrates electronic components with Micro-mechanical parts.

Radio Frequency (RF): Radio frequency (RF) is the rate of oscillation of an altering electric or electromagnetic field (current or voltage) in the frequency with a range from 20kHz to 300GHz.

Plasma: Plasma is called the fourth state of matter after solid, liquid, and gas. It is a state of matter in which an ionized substance becomes highly electrically conductive to the point that long-range electric and magnetic fields dominate its behavior.

Doping: In semiconductor production, doping is the intentional introduction of impurities into an intrinsic semiconductor for the purpose of modulating its electrical, optical and structural properties.

Physical Vapor Deposition (PVD): PVD includes a variety of vacuum deposition techniques to grow thin films over substrates. PVD is a process where the material expected to be deposited goes from condensed phase to vapor phase and then transit back to thin film condensed phase. Two common PVD processes are sputtering and evaporation.

Optoelectronics: Optoelectronics is the study and application of electronic devices that use light.

Statistically Significant: Statistical significance is the determination of the results from data of being not explainable by chance alone. Statistical significance is the opposite of null hypothesis, which tells that changes in the data are some random chances at work.

Design of Experiments: Design of experiments (DOE) is a systematic study to investigate the relationship between factors affecting a process and the output. In simple words, it is used to find cause-and-effect relationships.

Crystallography: The branch of science concerned with the structure and properties of crystals.

Crystallinity: Crystallinity refers to the degree of recursive structural order in a solid.

Cu-Kα: Copper K-α is an x-ray energy frequently used on x-ray instruments.

Impedance Spectroscopy: Impedance spectrometry is a method to evaluate impedance from the response of the current to the varying frequency of the imposed alternating voltage over a wide range and it is separated into real and imaginary components.

BIOGRAPHICAL SKETCH

Sajid Mahfuz Uchayash joined the Electrical Engineering Department at the University of Texas Rio Grande Valley in Fall 2019 semester, August 2019. Prior to that he received a B.Sc. degree in Electrical and Electronic Engineering (EEE) from the Bangladesh University of Engineering and Technology, Dhaka, in 2017. He received the prestigious Presidential Graduate Research Assistantship (2019-2021). He has been working at the Sputtering System Lab under Dr. Hasina F. Huq's supervision. He had also worked as Graduate Teaching Assistant under Dr. Paul Choi, Dr. Samir Iqbal, and Dr. Hasina F. Huq. During his M.Sc. period, he achieved 1st place at the College of Science (COS) poster competition and stood 1st runner up at the college of engineering annual E-Week poster competition 2021. He earned his M.Sc. in Electrical Engineering from the University of Texas Rio Grande Valley in August 2021. His research interest includes thin-film transistors, wide bandgap semiconductors, nanomaterials, nanoengineered Devices, and Bio-MEMS/NEMS. His paper on SiO_2/Si thin film characterization that has been described in chapter 3 in this thesis book has been accepted in IMECE-2021 conference. He has two other conference papers- one of them was in collaboration with MEMS research group in UTRGV. A journal paper he is expecting to publish about the characterization of pSi/Si thin films described in chapter 4 in this book. Additionally, he had been working on CIGS thin film solar cell collaborating with another graduate student- Meah Imtiaz Zulkarnain. He is expected to join the Kansas State University in Fall 2021 for Ph.D. in Electrical and Computer Engineering. He can be reached at usajidmahfuz@gmail.com.